

**ELECTRONIC AND MAGNETIC PROPERTIES OF
SYSTEMS WITHOUT PERIODICITY**

THESIS SUBMITTED FOR THE DEGREE OF
DOCTOR OF PHILOSOPHY(SCIENCE)

IN
PHYSICS (THEORETICAL)

BY

RUDRA BANERJEE



DEPARTMENT OF PHYSICS
UNIVERSITY OF CALCUTTA

April, 2012

To My Parents

Contents

Acknowledgment	xiii
1 Introduction	1
1.1 Brief Comments on Alloys	2
1.2 Brief review on magnetism and frozen phases	5
1.3 Plan of the Thesis	9
2 Methodology	13
2.1 Introduction	13
2.2 Many-body Schrödinger Equation	15
2.2.1 Born Oppenheimer approximation	16
2.3 Density Functional Theory	17
2.3.1 Hohenberg-Kohn Theorem	21
2.3.2 The Kohn-Sham Equation	22
2.3.3 Exchange and Correlation Potential	24
2.3.4 Extension to spin system	24
2.4 Solving Kohn Sham equation	25
2.4.1 LMTO method	25
2.4.2 KKR-ASA	27
2.4.3 Muffin Tin Orbitals	28
2.5 Recursion Technique	31
2.6 Augmented space formalism	32

2.6.1	The Configuration Space	32
2.6.2	Augmented space formalism	34
2.6.3	Augmented Space Theorem	36
2.6.4	Augmented space recursion in TB-LMTO formulation	38
2.6.5	Self Consistency between TB-LMTO and ASR	40
2.6.6	Problem of charge transfer, Madelung potential and energy	41
2.6.7	Termination Scheme	43
2.7	Effective Pair Interaction	45
2.7.1	Generalized Perturbation Method	46
2.7.2	Orbital Peeling	47
2.8	Frozen Spin Phase	50
2.8.1	Freezing of spin	51
2.8.2	Atomistic spin dynamics: Relaxing spins	52
2.8.3	ASD at finite temperature: Langevin Dynamics	53
3	Electronic structure calculation in random alloys	55
3.1	Dealing with disorder: Different levels of approximation	56
3.1.1	The Rigid Band Model and The Virtual Crystal Approximation	56
3.1.2	Average t-matrix approximation (ATA)	57
3.1.3	Coherent Potential Approximation	59
3.1.4	Beyond single site CPA	61
3.2	ScASR: The configuration averaged method	63
3.2.1	The ScASR Algorithm	64
4	Applications of ScASR: Electronic Structure of some binary alloys	71
4.1	CuZn and FeCr alloy	72
4.2	MnCr alloys and their stability	74
4.2.1	Calculation of ordering energy	74
4.2.2	Analysis of Stability	75
4.2.3	Conclusion	79
4.3	Magnetic properties of AuFe alloy	80

4.3.1	Electronic structure of AuFe Alloy	80
4.3.2	Magnetic structure of AuFe Alloy	81
4.3.3	Phase analysis of AuFe	86
5	Magnetic ordering in Ni-rich NiMn alloys around the multi-critical point	93
5.1	Introduction.	93
5.2	Samples	95
5.3	Ordering of magnetic moment carrying atomic spheres	97
5.4	Mean field analysis of the random Ising model	98
5.5	Magnetic relaxation	98
5.6	Conclusions	103
6	Magnetic properties of FeNiMo alloy	105
6.1	Sample	106
6.2	Experimental Motivation	107
6.3	Electronic structure and magnetic moments	109
6.4	Magnetic ordering	112
6.5	Mean-field analysis of transition temperatures	115
6.6	Magnetic relaxation : a theoretical analysis.	116
6.7	Conclusions	119
7	Magnetic properties of FeNiW alloy	121
7.1	Introduction	121
7.2	Samples	122
7.3	Experimental Motivation	122
7.4	Electronic Structure	124
7.5	Application to phase analysis of FeNiW ternary alloys	126
7.6	Conclusion	131
8	Magnetic properties of AuCrFe alloy	133
8.1	Introduction	133

8.2	Low Au regime	133
8.3	High Au Concentration: Around percolation limit	134
8.3.1	Cr above the percolation limit	134
8.3.2	Cr near the percolation limit	136
8.3.3	Cr inside percolation limit	140
8.3.4	Cr lower than the percolation limit	143
8.3.5	Comparison	145
9	Conclusion	147
	References	149

List of Figures

1.1	Binary lattice for $A_{50}B_{50}$ alloy	2
1.2	Publication per year on topic disordered alloy	3
1.3	Filling of 2nd row of periodic table according to Hund's rule.	5
1.4	Magnetic domain structure	7
2.1	Model of ions immersed in electron sea: a cartoon	14
2.2	Flowchart for solving Kohn-Sham Eqn	23
2.3	Atomic sphere approximation	26
2.4	The muffin-tin potential	29
2.5	Graphical representation of chain model.	31
2.6	Scheme of recursion	33
2.7	Interaction between adatoms. (a) when adatoms are far away and (b) when adatoms are close.	48
2.8	Frustration in 2d lattice	51
3.1	Simple flowchart for CPA.	61
3.2	The TB-LMTO-Augmented Space Recursion package flowchart	65
4.1	CrFe and CuZn DOS.	73
4.2	DOS and EPE of $Mn_{50}Cr_{50}$ alloy.	76
4.3	Ordering and Pair energy of $Mn_{50}Cr_{50}$ alloy	77
4.4	$V_{\text{eff}}(\vec{k})$ and contours on the plane bounded by different plane of MnCr alloy. . .	78
4.5	Projected DOS of AuFe alloy	80
4.6	Local magnetic moment of AuFe alloy.	81

4.7	Pair energy of AuFe alloy as function of composition and its variation	83
4.8	Moments of $J(R)$ for AuFe alloys (for $R \geq a$) and their variation with composition	84
4.9	Plaquettes on the face-centered cubic lattice	85
4.10	Decay of scaled moments I_n with n for AuFe	87
4.11	Phase diagrams for AuFe alloys	91
5.1	EPE for $\text{Ni}_x\text{Mn}_{1-x}$ alloy.	96
5.2	Phase diagram of NiMn based on a mean field calculation.	98
5.3	Auto correlation functions for $\text{Ni}_{1-x}\text{Mn}_x$ alloy	99
5.4	Comparison of NiMn alloy with different composition for highest waiting time used (blue curves in Figure 5.3).	100
5.5	Proposed phase diagram from Monte Carlo simulations followed by the aging analysis	101
5.6	Theoretical study of decay of magnetization with time.	102
6.1	Magnetization vs Temperature for two FeNiMo compositions	107
6.2	$M(H)$ vs H taken at 5 K for samples (4), (5) and (6).	108
6.3	M vs T results for sample (6) with both field-cooled and zero-field-cooled situations.	108
6.4	Local magnetic moments per atom on Fe, Ni and Mo sites	110
6.5	Local magnetic moments on Fe, Ni and Mo sites	111
6.6	The dominant pair energies between Fe-Mo, Fe-Ni, Mo-Mo, Fe-Fe, Fe-Mo and Ni-Ni	113
6.7	The first four moments of the probability distribution of the Ni-Ni pair-energies shown as functions of Fe concentration.	114
6.8	Mean-field phase diagram (top) for NiFeMo.	116
6.9	Relaxation of auto-correlation function at $T=5\text{K}$	117
7.1	Magnetization vs Temperature for three compositions of FeNiW	123
7.2	$M(H)$ vs H taken for samples 4,5 and 6 taken at 5 K.	124
7.3	Local magnetic moments on Fe, Ni and W sites as a function of composition .	125
7.4	Total magnetic moments as a function of Fe concentration	126
7.5	The pair interactions for different pairs of FeNiW alloy	127

7.6	Behavior of the n-th nearest neighbor pair energies	127
7.7	$J^{NiNi}(R)$ and $\log(J^{NiNi}(R))$ of FeNiW alloy	128
7.8	Curie Temperature	130
7.9	Mean-field phase diagram	130
8.1	EPE for $Au_xCr_{20}Fe_{100-20-x}$	135
8.2	Spin relaxation of $Au_xCr_{20}Fe_{100-20-x}$ alloy for different waiting time	136
8.3	EPE for $Au_xCr_{25}Fe_{100-25-x}$ alloy	137
8.4	Autocorrelation function for $Au_xCr_{25}Fe_{100-25-x}$ alloy	138
8.5	EPE of $Au_xCr_{18}Fe_{100-18-x}$ alloy	139
8.6	Autocorrelation function for $Au_xCr_{18}Fe_{100-18-x}$	140
8.7	EPE for $Au_xCr_{10}Fe_{100-10-x}$ alloy	141
8.8	Autocorrelation function for $Au_xCr_{10}Fe_{100-10-x}$	142
8.9	EPE for $Au_xCr_{06}Fe_{100-06-x}$ alloy	143
8.10	Autocorrelation function for $Au_xCr_6Fe_{100-6-x}$	144
8.11	Comparison of EPE's and ACID for $Au_{70}Cr_xFe_{30-x}$ alloy	146

List of Tables

1.1	Examples of Ferromagnets and Antiferromagnets	7
3.1	gprof data for ScASR code	68
3.2	Comparison between old code based of augmented space recursion and AMscf .	69
4.1	Weights for different neighboring shells for seven different bcc based equi-atomic superstructures.	77
4.2	Number of different triangular, quadrilateral and pentagonal plaquettes in a cubic unit cell	86
5.1	Atomic concentration of NiMn alloy and lattice parameters.	97
6.1	Atomic % of Ni, Fe and Mo in the six alloy samples and lattice constant. . . .	106
6.2	Summary of experimental results on the six alloy samples.	109
6.3	Fitted time parameters ($\tau_1 < \tau_2$) for the double exponential decay of magnetization at 5K for different damping parameters	118
7.1	Composition of the six samples in atomic %.	122
7.2	Summary of experimental results on the six samples.	125
8.1	Samples in low-Au regime in atomic %	134
8.2	Samples in Cr>percolation limit	136
8.3	Samples in Cr \approx percolation limit	137
8.4	Samples in Cr inside percolation limit	140
8.5	Samples in Cr<percolation limit	143

Acknowledgment

When you have finished what is supposed to be your great achievement, you look back and realize you owe a great deal to other people. A thesis, that spans a good five years, cannot be any different.

First and foremost, I want to express my gratitude to my thesis supervisor. His patience and encouragement through ups-and-downs during these years were the major impetus for me to forge ahead. Also his vast knowledge and understanding of the subject and his enthusiasm to share them with me made the work pleasant. This nature of his is reflected in his students also which makes our research group very vibrant; and ensured very comfortable relations with the group seniors.

Also, I will take this opportunity to express my gratitude to Prof. D. G. Kanhere who introduced me to the field of Condensed Matter Physics and simulation during my Masters programme. Learning the basics of my research work from such a wonderful teacher is indeed a great opportunity.

Dr. Biplab Sanyal, Associate Professor in Physics at Uppsala University helped me a lot to understand the field better. Being a group senior, he was always accessible. His experience and exposure that he shared with me changed my outlook towards the field. Beside having very fruitful collaboration with him, his unfailing support and his new perspectives of looking at a problem was very fresh and encouraging. I wish, in particular, to thank his wife, Prof. Suparna Sanyal. Her enthusiasm in arranging evening get-togethers after tiring days work is worth emulating.

I am thankful to my group-mates. My juniors, Prashant, Ambika, Rajiv and Gopi always kept the group vibrant and made the work enjoyable. Without Shreemoyee's presence in the computer center, the work-time would have been very dull. My seniors like Kartick Tarafder, Aftab Alam and Monodeep Chakroborty are people whom I literally regularly nagged at; but they always helped me, and were never tired of my idiotic mistakes and questions. Among seniors, Atis Chakroborty owes special mention. It was his work that was my first stepping stone to look into world of disordered systems.

I want to appreciate Madhuparna Karmakar and Anuradha Das. The food would not

be as tasty without the pseudo-scientific discussions we shared. My stay here would have been stale without their presence. My mates in hostel like Arghya, Angshuman, Shubhasish, Ashutosh, Sayani only to name a few, are the persons who made my stay pleasant. I always look for late night tea and chat with them to refresh my mind. In general, the first year Ph.D. and Post B.Sc batch in the centre gave me a very refreshing time during the tedious period of writing this thesis. I must not forget Sumanta, Soumyajyoti, Biswarup and Nandini for those unforgettable time spent in Uppsala.

I would like to thank Swedish Institute for their fellowship which helped me visit Department of Physics and Astronomy, Uppsala University yielding a long standing collaboration with Prof. Olle Ericksson's group. Also, I would like to thank AMRU project and its Principle Investigator, Prof. Tanusri Saha-Dasgupta for financial support when I needed it most.

Also, I would like to thank the Administrative staff of the Centre for all their help, specially Mr. Sunish Kumar Deb and Mrs. Sohini Majumder. To the library staffs, who were always ready to sort out the books for me, I owe special thanks. I would like to thank people who took care of the computational facilities in the centre, specially, Arnab, Anjan and Sudeep: they were always ready to help to the best of there ability. Their presence helped me to experiment on the linux installation. I should also mention Elisabeth Bill for her help during my stay in Uppsala.

In this journey, one person is worth special mention. She was always by my side when I was in need. She always helped me to come out of down phases and lit a light during my stay here. On one hand, the huge amount of time we spend together is a memory of joy. On the other hand, her tenacity and approach to problems and life in general is worthy of emulation. A true friend like her is rare and I am really lucky to have her as friend. Thank you Hena!

Last, but not the least, I want to express my gratitude my to mother and father. For their support and patience any words like "thanks" or "gratitude" falls short . I know, no words can match the suffering and sacrifice you two did for me. But, here I just would like to take this opportunity to say a mighty "THANK YOU".

Rudra Banerjee

Chapter 1

Introduction

Most graduate text books on solid state physics or Condensed Matter Physics begin with the definition of a Bravais lattice with some type of symmetry: A (three-dimensional) Bravais lattice consists of all points with position vector \mathbf{R} of the form

$$\mathbf{R}_n = \sum_{i=1}^3 n_i \mathbf{a}_i \quad (1.1)$$

where \mathbf{a}_i 's are any three non-coplaner vectors and n_i 's are integers [Ashcroft and Mermin, 1976]. From a lattice we get a crystal structure when we assign one or more atoms, defined as basis, to each lattice point. This basis can be made of only one type of atom, or more.

The point we miss is that this is a mathematical description of *ideal* lattice [Kittel, 2005]. In real life, in first place, we can never have an infinite lattice. Even if we assume this edge/surface effect is negligible in the bulk [Ashcroft and Mermin, 1976, Chapter 18], it is still very difficult to have a *perfect* lattice. Natural lattices always have many kinds of defects [Ashcroft and Mermin, 1976, Chapter 30].

The assumption of an underlying lattice symmetry hugely simplifies the problem and enables us to consider many complex structures. Bloch's theorem enables us to state symmetries of the wave functions even before solving the Schrödinger equation which leads to them.

But there are many situations like in confined systems (clusters), surfaces and random alloys where we cannot invoke lattice translation symmetries. For first two classes of problems, we basically consider them as a infinite systems with large separation between each unit. On the other hand, for random alloys we need to take different approach. These will be the classes of materials studied in this thesis.

1.1 Brief Comments on Alloys

An alloy is a solid solution composed of two or more constituents. Alloys are prepared taking real life application into account. Some properties are enhanced to suit specific applications. For example, stainless steel, a ternary alloy, made of Fe, Cr and C is stronger than Fe and rust free. It is widely used in everyday life [Armgnac, 1930]. Starting from the “Bronze Age”, one of the first achievements of human civilization is its ability to smelt an ore, with an alloy of Cu and Sn.

In modern world, alloys are ubiquitous. Chemisorption, catalysis, semiconductor device physics, liquid metals, glasses etc. are all based on study of alloys. Their various properties like optical, electrical, magnetic, structural and elastic are under intense investigation [Gonis, 1992].

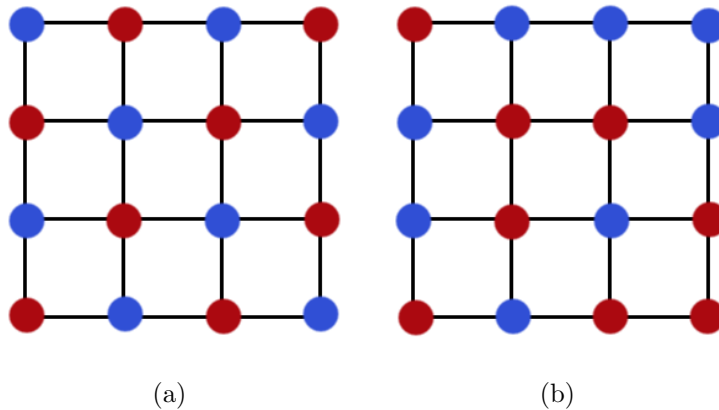


Figure 1.1: Binary lattice for $A_{50}B_{50}$ alloy: (a)ordered configuration: Blue atoms are arranged along one diagonal, Red atoms are arranged in opposite diagonal. (b)disordered configuration: Blue and Red atoms are arranged in a complete disordered manner.

The generic symbol of a binary alloy (alloy with two constituent elements) is A_xB_{100-x} where A and B are the elements and x is the atomic percentage of A . According to the lattice structure and value of x , alloys become ordered or disordered. For example, for a simple cubic structure, the necessary but not sufficient condition for being in an ordered phase is that the concentration of A is nx where n is an integer with $1 < n \leq 7$ and $x = 12.5/n$. For

other concentrations, ordered phase is not possible.

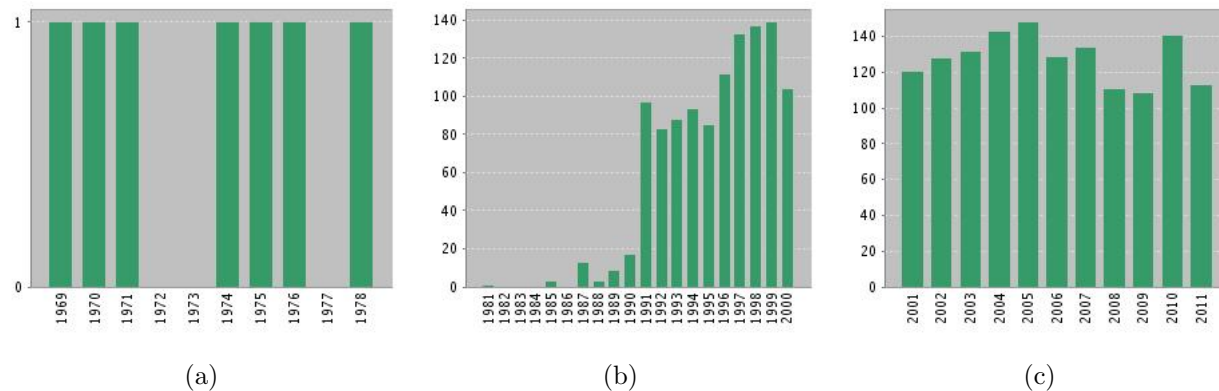


Figure 1.2: Citation per year on topic disordered alloy form <http://apps.isiknowledge.com/portal> [web of knowledge, 2012], using search criteria “Topic=(alloy) AND Topic=(disordered), Search language=English Lemmatization=On ”(a)Year 1950 to 1980;(b)Year 1981 to 2000; (c)Year 2001 to 2011. The data indicates meteoric rise in citations on the work on disordered alloys during 1980-2000 and its eventual saturation.

But the disordered phase is possible even for all those concentrations depending on the ordering energy of the alloy (see § 4.2 on page 74). Figure 1.1 shows an ordered and a disordered arrangement in a square lattice for $A_{50}B_{50}$ alloy.

Figure 1.2 shows papers published with title containing ‘alloy’ and ‘disorder’ from 1950 to 2011 [web of knowledge, 2012]. It clearly shows there has been a huge increase in interest during last twenty years, just when digital computers became sufficiently powerful to handle sophisticated algorithms and data needed to solve this type of problem. This is due to the fact that, as we lose the crystal symmetry, even by a single defect, the consequence is considerable. First of all, Bloch’s theorem is no longer valid. So, the crystal momentum \tilde{k} and k -selection rules are no longer applicable. Hence, to get any microscopic property, we need to study different specific alloy configurations. To have an idea, a material with N sites with C defects, the number of possible configuration is ${}^N P_C$. If we consider $N \sim 10^{20}$, we readily understand the amount of difficulty that we face. How we tackle this difficulty is discussed in detail in § 2.6 on page 32.

The earliest study of disordered systems may be traced back to Lord Rayleigh’s paper

on multiple scattering theory(MST) [Rayleigh, 1892]. By the 1960's the field got much needed impetus through the works of Korringa [Korringa, 1947], Lax [Lax, 1951, 1952] and Beeby [Beeby, 1964a,b]. These studies provided the formal background of MST. Many different approximations were proposed for the electronic structure of disordered alloys. The same time saw emergence of several approaches of dealing with disorder. The advent of *Density functional theory* [Hohenberg and Kohn, 1964; Kohn and Sham, 1965] and the digital computer helped these studies to progress. The accuracy of any model could be easily checked. Among those approximations, the rigid band approximation [Stern, 1967], the virtual crystal approximation [Dargam et al., 1997] and the coherent potential approximation [Soven, 1967] are particularly noteworthy. These techniques are discussed briefly in §3.1. In 1973, Mookerjee introduced the augmented space formalism(ASF) [Mookerjee, 1973], which went beyond the mean field approach to the study of disorder and included environmental effects in its orbit.

Most of the study of alloy systems has been based on a 'local' representation basis e.g. tight binding(TB) and/or linear combination of muffin-tin orbitals(LMTO) description of the Hamiltonian. TB version of LMTO also been used widely(see §2.4.3). Coherent Potential Approximation (CPA) based on the TB-LMTO approximation is very successful [Kudrnovský et al., 1990; Kudrnovský and Drchal, 1990]. But it was a mean field approximation. It could not take into account effect of local environment.

Augmented space method was introduced to bridge this gap. It was one of the successful generalizations of the CPA and could incorporate environmental effects at a site.

Great progress has been made in study of disordered alloys. But effect of disorder in solids is still debated. As quoted from Kittel [Kittel, 2005, 8th edition]

“Experiment and theory agree that the consequences of the destruction of perfect translational symmetry are much less serious (nearly always) than we expect at first sight”

This viewpoint needs discussion. While, as shown by Kittel that properties like resistivity are linear with composition, that does not end the story. As stated at the very beginning, alloys are made keeping their industrial application in mind. Their phase space, magnetic and mechanical properties are strongly dependent upon composition (and ordering). For

example, we will show later in this thesis (see, for example Figure. 5.5 on page 101) that magnetic property changes drastically between 20%-25% Mn concentration in NiMn alloy. An linear interpolation of magnetic data will give severely wrong result; making the alloy unusable to real world.

1.2 Brief review on magnetism and frozen phases

The fundamental building block of magnetism is the magnetic moment: for a current I around a loop $|\mathbf{dS}|$, magnetic moment is defined as

$$d\mathbf{m} = I\mathbf{dS} \quad (1.2)$$

This leads to orbital moment(\mathbf{l}) of electron. The intrinsic magnetic moment or spin(\mathbf{s}) of electron is another source of magnetism. In a real system, these two are often coupled, via the spin-orbit coupling. This coupling produces a total magnetic moment(\mathbf{j}) of the system. In metallic system, itinerant electrons also contribute to the total magnetic moment. For

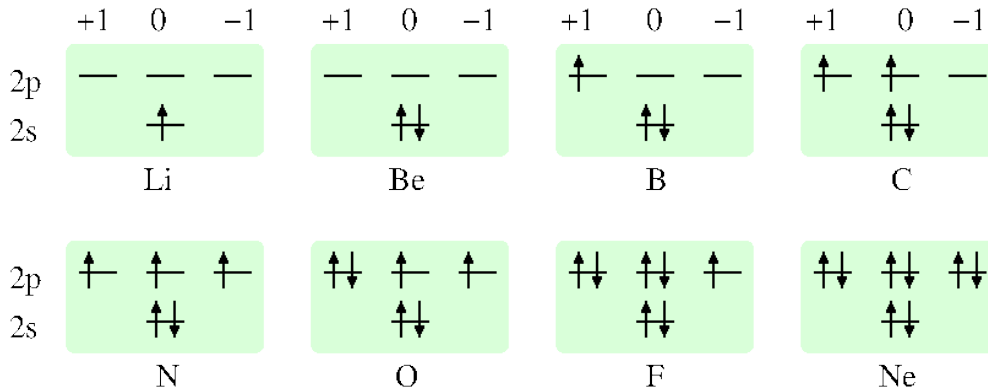


Figure 1.3: Filling of 2nd row of periodic table according to Hund's rule. Total spin and orbital momentum are as follows: Li($S=\frac{1}{2}$, $L=0$); Be($S=0$, $L=0$); B($S=\frac{1}{2}$, $L=1$); C($S=1$, $L=1$); N($S=\frac{3}{2}$, $L=0$); O($S=1$, $L=1$); F($S=\frac{1}{2}$, $L=1$); Ne($S=0$, $L=0$)

insulators, describing magnetism is relatively simpler. Hund's rule describes the filling of electron such that the spin quantum number S and orbital quantum number L are always

maximum given the number of electron. It also requires $J = |L - S|$ for $n \leq 2l + 1$ and $J = |L + S|$ for $n \geq 2l + 1$ where n is the number of electron in the shell and l is the angular momentum. The filling up of isolated atoms of second row elements of periodic table and their moments are shown in Figure 1.3. In this thesis, we shall not discuss magnetism of insulator. Interested readers are referred to [Kaxiras, 2003] for a lucid and detail discussion.

Magnetism in metals is rather interesting. The contribution comes from both local and itinerant electrons as described above. As a first approximation, we consider the itinerant electrons to be free fermion of spin $\frac{1}{2}$ in an external magnetic field. This leads to Pauli paramagnetism with magnetic moment of each particle $m = g_0 \mu_B$ where $g_0 = 2.003$ is electronic g -factor and μ_B is Bohr magneton.

The orbital motion of electron, on the other hand, in presence of external magnetic field, tries to shield the external field, leads to Landau diamagnetism [Peierls, 1955]. Pauli paramagnetism and Landau diamagnetism are seen in metals. They are equivalent in magnitude and opposite to each other in sign. The theory of Pauli and Landau is based on non-interacting microscopic moments, which is not correct for electrons in metal. The model that take the electron-electron interaction is Heisenberg spin model. The model is based on interacting spins $\mathbf{S}(\mathbf{R})$ at the lattice site \mathbf{R} . Spins at site \mathbf{R} and \mathbf{R}' interact with each other via the exchange term $J = J(\mathbf{R} - \mathbf{R}')$. The Heisenberg hamiltonian is

$$\mathcal{H} = -\frac{1}{2} \sum_{\mathbf{R} \neq \mathbf{R}'} J(|\mathbf{R} - \mathbf{R}'|) \mathbf{S}(\mathbf{R}) \cdot \mathbf{S}(\mathbf{R}') \quad (1.3)$$

If the exchange term J is positive, the system is ferromagnetic as $\langle \mathbf{S}(\mathbf{R}) \cdot \mathbf{S}(\mathbf{R}') \rangle \geq 0$, which leads to minimal energy and spins will be oriented in same direction. When $J < 0$, the spins tend to orient in opposite direction to each other, leads to antiferromagnetic ordering.

Temperature destroy magnetic ordering. Table 1.1 shows critical temperatures of few elements and compounds and also the number of Bohr magnetons per atom, n_B , which is difference between up and down electrons. Higher the value of n_B , higher is the magnetic property of the solid. The saturation magnetization, M_0 is the magnetization when all spins are aligned in same direction. Generally, to achieve this state, we need external field. This leads to *domain* structure. As in ferromagnetic interaction, the dominant interaction tries to align neighboring sites aligned parallel to itself, which is not energetically favorable. Other

Elements					
Ferromagnets				Antiferromagnets	
Solid	T_c	n_b	M_0	Solid	T_n
Fe	1043	2.2	1752	Cr	311
Co	1388	1.7	1446	Mn	100
Ni	627	0.6	510	Ce	13

Compounds			
Ferromagnets		Antiferromagnets	
Solid	T_c	Solid	T_n
MnB	152	MnO	122
FeP	215	NiO	600
CrTe	339	CoF ₂	38

Table 1.1: Examples of Ferromagnets and Antiferromagnets. T_c is Curie Temperature, T_N is Néel temperature, n_B is number of Bohr magneton per atom and M_0 is saturation magnetization in Gauss [Car and Parrinello, 1985; Kaxiras, 2003]

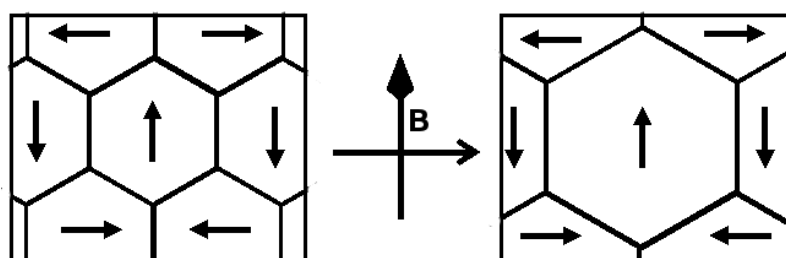


Figure 1.4: Magnetic domain structure. The arrows in the domain shows local magnetic directions. The filled arrow in the middle shows the direction of magnetic field applied to the system in the right.

moments will orient at different angle to each other to minimize the energy of the system. Though this long range dipole interaction is much weaker than short range magnetic order, the huge number of such dipole in macroscopic scale makes the term significant and hence, must be optimized.

The system accommodates this by breaking into parallelly aligned subsystems, called domain. In a domain, all moments are parallel but not correlated with neighboring domain. When a magnetic field is applied in certain direction, the domain with intrinsic moment along that direction grows larger in expense of other domains, as shown in Figure 1.4.

In paramagnetic interaction, no such short range ordering is observed to create domain; rather microscopic magnetic moments are oriented in random order. Now if ferromagnetic and antiferromagnetic interactions coexist in a spin system, then their origins a frustrating interaction and the system becomes disordered. Usually, this property is seen in dilute magnetic materials, where magnetic atoms randomly substitute nonmagnetic matrix. Classic examples of this type of system are AuFe and CuMn.

Cannella and Mydosh [Cannella and Mydosh, 1972] showed unusual phase transition in AuFe alloy. The ac magnetic susceptibility showed a maximum at a frequency-dependent temperature T_f . This type of cusp in ac magnetic susceptibility is then seen in many other spin glass and became a signature of this type of system.

Edward and Anderson [Edwards and Anderson, 1975](EA hereafter) tried to describe this system using

$$H = -\frac{1}{2} \sum_{\substack{x,y \in \Lambda \\ x \sim y}} J_{R_i, R_j} S_{R_i} S_{R_j} \quad (1.4)$$

where Λ is the complete system and $x \sim y$ is x and y are nearest neighbor. Few months later, Sherrington and Kirkpatrick [Sherrington and Kirkpatrick, 1975](SK hereafter) put forward a mean field solution of Edward and Anderson’s model, named “*replica symmetry*”. This model turned out to be incorrect and self contradictory. The local free energy extrema turned out to be unstable and led to a negative entropy as $T \rightarrow 0$. Parisi [Parisi, 1980] overcome the problem by introducing “*continuous replica symmetry breaking scheme*”. Mézard *et al* [Mézard et al., 1987] collected the results published still 1987 using replica breaking scheme and other. Various models keep coming. Among them, “*Generalized random energy model*”

by Derrida [Derrida, 1985] is particularly famous for it is exactly solvable and its prediction is similar to SK model. Binder and Young [Binder and Young, 1986] summarized the evolution and problems raised in this field in 1986. The progress in next one decade was summarized by Bovier and Picco [Bovier and Picco, 1998] in 1998. Newman and Stein [Newman, 1997] show fundamental difference between EA and SK's model. So, not much optimism left until Guerra [Guerra and Toninelli, 2002] and Toninelli [Guerra, 2003] solved some mathematical problems like the existence of Thermodynamic limit of SK model. A brief and up-to-date review of mathematical development of spin glass is given by [den Hollander and Toninelli, 2004]. Overall, a dependable model for Spin Glass is still alluring physicists. The reason is two fold

- (a) EA model is far yet to be solved.
- (b) Mean field approximation (SK model) can not explain the broken symmetry of short ranged systems.

The underlying reason is discussed in detail in [Newman and Stein, 2003b,a]. A very readable account of this history is available in [Stein, 2004; Stein and Newman, 2011].

Condensed matter Physicists took a rather different approach. The starting point is the Landau and Lifshitz's (LL) theory [Landau and Lifshitz, 1935] on precision of local magnetization in the presence of local magnetic field. LL equation is applicable to solids, as well as thin films and nano-strips [Hillebrands and Ounadjela, 2002, 2003, 2006]. Brown [Brown, 1963] and Kubo *etal* [Kubo and Hashitsume, 1970] extend LL equation for finite temperature using Langevin dynamics for magnetic nanoparticles [Brown, 1963] and classical single spin [Kubo and Hashitsume, 1970] system.

Antropov [Antropov et al., 1995, 1996] developed a method to calculate magnetization dynamics with time within the framework of density functional theory. Stocks [Stocks et al., 1998; Ujfalussy et al., 2004] later extend the method to self consistent field.

1.3 Plan of the Thesis

This thesis is organized as follows:

In chapter 2 I have discussed various methods used to calculate electronic and magnetic properties of systems without periodicity. First, given a brief description to the complete Hamiltonian, I move to the density functional theory and its extension to magnetic systems. DFT gives the chemical signature of the constituent elements. Then I gave a detailed introduction to multiple scattering theory. I then discussed the TB-LMTO-ASA formalism in details that is general for electronic structure theory. Augmented space formalism comes next which is our preferred tool for studying disorder alloy. This completes our toolbox for studying electronic structure of systems without periodicity.

I next discussed the *orbital peeling* technique as a method for obtaining effective pair interactions. Since this technique is not widely used, I have discussed the methodology in detail and the reasons behind choosing this over other formalism. As spin glass system is one of our focus system I studied, I discussed atomistic spin dynamics based on Landau-Lifshitz-Gilbert equation. These two methods enable us to calculate spin-spin auto-correlation function that surely gives a very dependable way to study the possibility of existence of any spin frozen phase.

In chapter 3 I have discussed the Augmented Space Recursion(ASR) based code ScASR that have developed and used through out my research. Its theoretical background is given in §2.6. In this chapter I have detailed the algorithm and working principle. I have also shown its superiority compared to previously available ASR based code as far as efficiency and runtime is concerned. In the beginning of this chapter I have also reviewed other methods suitable for disordered systems and showed there pros and cons that make me choose ASR based algorithm.

In chapter 4 I have discussed implementation of ScASR , a self consistent ASR based code and Orbital peeling technique in three binary alloys. As for any new code, the work in this chapter is a testing ground for the code. I show its applicability and accuracy in various previously studied alloy systems.

In §4.1 I have discussed Electronic structure of two very different type of alloys: CuZn shows ‘split band’ Density of states(DOS), and FeCr has ‘overlapping band’ DOS.

In §4.2 I have discussed Electronic structure and stability of the MnCr alloy system.

In §4.3 I have discussed the Electronic structure and Effective Pair interaction of AuFe Alloy.

In chapter 5 I have carried out ab initio density functional calculations along with finite temperature studies using mean field analysis and Inverse Monte Carlo simulations. Our theoretical analysis was in two steps. A DFT based calculation of the formation of moments in atomic spheres and a statistical analysis of the free-energetically the most favorable arrangement of these moment carrying spheres. Since I believe that the spin-glass transition is a dynamic freezing of spin degrees of freedom, I studied magnetization relaxation using a LLG formalism. I showed that in the composition range where experiment observes spin-glassy behavior, I also see aging behavior and anomalously slow relaxation of magnetization. The DFT part was done for uniaxial spins, I were unable to describe the ferro-spin-glass or the anti-ferro-spin-glass mixed phases. Since the moments are randomly canted in these phases it would have required a generalization of the DFT part to allow description of non-collinear magnetic moments before carrying out the statistical analysis of their favorable arrangements.

I have carried out Reverse Monte Carlo simulation with effective pair energy result from first principle calculation. I have shown this method is capable of reproducing experimental results dependably, as shown in [Pal et al., 2012].

In chapter 6 I have discussed electronic and magnetic properties of FeNiMo alloy for various concentration. In the first half, I investigated the behavior of magnetization with temperature and magnetic field of six samples at different compositions of this disordered ternary alloy NiFeMo. I analyze the data using a first-principles density functional based electronic structure method and a mean-field phase diagram study. For five of the compositions there is a clear indication of transition from a paramagnetic to a random ferromagnetic phases. Fe boosts and Mo depletes the fragile moment on Ni. The sixth sample with large Mo concentration showed the possibility of a glassy phase. In the second part of this chapter I carried out more intense study to see if there is and frozen phase exists in high Mo sample. Comparing our theoretical investigation along

with experimental study shows a possible ferro-spin-glass mixed phase in this regime.

In chapter 7 I have discussed electronic and magnetic properties of FeNiW alloy for various concentration. This is actually a continuation of work done in §6 in the sense that in this two chapter I have studied effect of $4d$ and $5d$ element in permalloy respectively. Using first-principles LSDA based TB-LMTO-ASR method I have obtained the magnetic moment across the composition range. I compared our results with the experimental saturation magnetization. Based on the generalized perturbation expansion, I mapped the energetics of the problem onto an equivalent random Ising model. The pair energies of the Ising model were derived from the TB-LMTO-ASR using Lichtenstein's formula. Our mean-field analysis of the model shows that at low Fe concentrations not only frustration decreases, but Ni also loses its moment. The resulting phase diagram confirms the possibility that spin-glass transition may not take place in this system even at low Fe concentrations, as found experimentally.

In chapter 8 I have discussed the effect of Cr in AuFe alloy. For reference, I have taken the spin glass limit of Cr (10 to 15 atomic %) as in binary AuCr alloy as the reference for Cr and varied the Cr concentration of Cr around the concentration. I have shown the breaking of breaking of spin-glass phase around binary Cr concentration. I have also shown that spin glass phase is only possible when Au concentration is high and among Fe and Cu, one is high and other is very less.

Chapter 2

Methodology

2.1 Introduction

A solid is made up of atoms bonded together by a sea of *valence electrons*. For example, let us consider solid Na. If we examine the Na atom we see that at its nucleus contains eleven protons and twelve neutrons bound together by nuclear forces. In the energy range of our interest, i.e. up to a few hundred eV, we are unable to probe the structure of this nucleus. We shall model the nucleus by a point object of charge $+11e$. The eleven electrons which neutralize this nucleus have the structure $1s^2 2s^2 2p^6 3s^1$, arranged with decreasing binding energy in the attractive Coulomb potential of the nucleus. Of these, the first ten electrons are so tightly bound to the nucleus that when these Na atoms bind together to form a solid, these electrons hardly change their quantum state. These are called *core electrons*. If we probe the solid with energies lower than that required to excite these core electrons out of their bound quantum states, then we can consider the nucleus and these core electrons together as a single, featureless ion-core with a single positive charge on it. These Na^+ *ion cores* are arranged on a lattice. The outermost $3s^1$ electron is given up by the Na atom to form the *valence electron* cloud in which the ion-core lattice is immersed. The Figure 2.1 illustrates this model.

Why does the valence cloud bind the solid together? If the valence cloud were not there the ion-cores would repel one another by Coulomb repulsion and could not form a bonded solid. If they are immersed in the valence cloud, then if we consider a small negative charge packet as shown in the Figure 2.1, it will attract two of the neighbouring ion-cores towards it. These ion-cores will then see an effective, indirect attraction via the valence cloud. If this attraction can just balance the Coulomb repulsion for a given configuration of the ion-cores, then this will be the stable configuration of the ion-cores in the solid. The ion-cores are then the building blocks we have been talking about, the valence charge cloud the glue

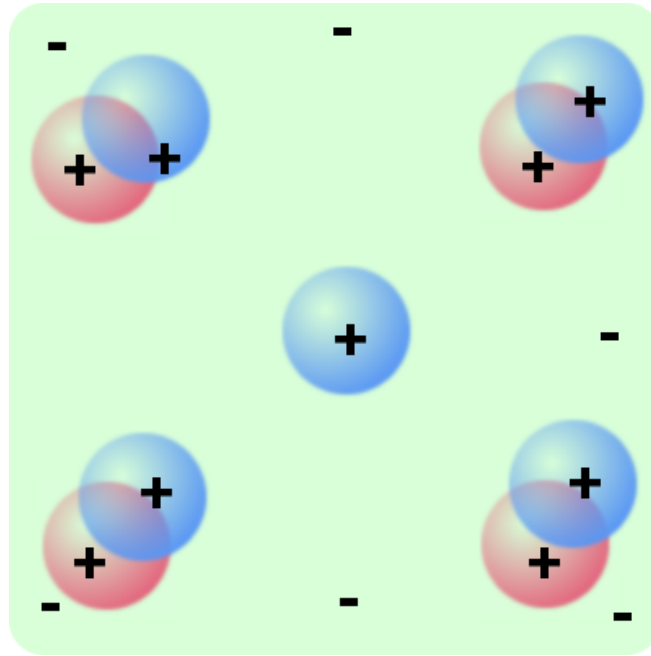


Figure 2.1: Model of ions immersed in electron sea: a cartoon

that holds them together, and the stable configuration the underlying lattice. Of course the ion-cores are not static in the equilibrium configuration. At temperatures much below the melting temperature, the ion-cores can at most vibrate with amplitudes much less than the inter-ionic distances. When the amplitude is comparable to the inter-ionic spacing, the solid becomes unstable and a transition to a liquid state takes place. We shall be sufficiently far from this instability temperatures. Even at 0°K , quantum mechanical uncertainty principle dictates that there will be zero-point vibrations of the ion-cores.

This is the model that will be our starting point. We shall first describe the quantum mechanics of the system of ion-cores and valence electrons. The great advantage in this problem is that the interaction potentials are all Coulombic and hence exactly known. The disadvantage, as we shall see, is the immense number of interacting objects.

2.2 Many-body Schrödinger Equation

Based on above model, we write Hamiltonian of the system. For M atoms sitting at position $\{\mathbf{R}_I\}$ and $N = ZM$ electrons, where Z is the number of valence electron per atom, sitting at $\{\mathbf{r}_i\}$, the Schrödinger Hamiltonian is given by:

$$\begin{aligned} \hat{\mathcal{H}} = & -\frac{\hbar^2}{2m_e} \sum_{\mathbf{r}_i} \nabla_{\mathbf{r}_i}^2 - \frac{\hbar^2}{2M_I} \sum_{\mathbf{R}_I} \nabla_{\mathbf{R}_I}^2 - \sum_{\mathbf{r}_i, \mathbf{R}_I} \frac{Z_I e^2}{|\mathbf{r}_i - \mathbf{R}_I|} + \frac{1}{2} \sum_{\mathbf{r}_i, \mathbf{r}_j} \frac{e^2}{|\mathbf{r}_i - \mathbf{r}_j|} \\ & + \frac{e^2}{2} \sum_{\mathbf{R}_I, \mathbf{R}_J} \frac{Z_I Z_J}{|\mathbf{R}_I - \mathbf{R}_J|} \end{aligned} \quad (2.1)$$

in short,

$$\hat{\mathcal{H}} = \hat{\mathcal{T}}_e + \hat{\mathcal{T}}_N + \hat{\mathcal{V}}_{int} + \hat{\mathcal{V}}_{ext} + \hat{\mathcal{V}}_{NN} \quad (2.2)$$

where, using Hartree units,

$$\begin{aligned} \hat{\mathcal{T}}_e &= - \sum_{\mathbf{r}_i} \frac{1}{2} \nabla_{\mathbf{r}_i}^2 && \text{(Kinetic Energy of Electrons)} \\ \hat{\mathcal{T}}_N &= - \sum_{\mathbf{R}_I} \frac{1}{2} \nabla_{\mathbf{R}_I}^2 && \text{(Kinetic Energy of Nucleus)} \\ \hat{\mathcal{V}}_{ext} &= - \sum_{\mathbf{r}_i, \mathbf{R}_I} \frac{Z_I e^2}{|\mathbf{r}_i - \mathbf{R}_I|} && \text{(Ion-Electron interaction)} \\ \hat{\mathcal{V}}_{int} &= \frac{1}{2} \sum_{\mathbf{r}_i, \mathbf{r}_j} \frac{1}{|\mathbf{r}_i - \mathbf{r}_j|} && \text{(Electron-Electron interaction)} \\ \hat{\mathcal{V}}_{NN} &= \frac{1}{2} \sum_{\mathbf{R}_I, \mathbf{R}_J} \frac{Z_I e^2}{|\mathbf{R}_I - \mathbf{R}_J|} && \text{(Ion-Ion interaction)} \end{aligned}$$

This is a multi-component many-body system and the two-body nature of $\hat{\mathcal{V}}_{ext}$ makes the equation inseparable. As a consequence, beyond some simple systems like hydrogenoid atoms and H_2^+ molecule, its not possible to solve it analytically. Even numerically, a complete solution of eqn. (2.1) are available only for few cases like single atoms and very small molecules.

The most of this chapter is review on the development of some reasonable and well-controlled approximations that will enable us to calculate a wide variety of systems, that are of interests.

2.2.1 Born Oppenheimer approximation

The first step in this approximation is that the nuclei is much heavier than the electrons (rest mass is 1:1836) [Born and Oppenheimer, 1927] and so is the time scale associated with the motion of them. For the bounded systems, the smallest excitation energy (E_e) for electron is of “*particle in a box*” nature and varies from 0eV (for metal) to few eV (1.1eV in Si, 4eV in Diamond). On the other hand, nuclear vibration energy, in harmonic approximation, is $E_v = \hbar\omega \approx M\omega^2 a^2 = (m/M)^{1/2} E_e$; rotational energy of the nuclei is $E_r = L^2/I$ where L is the angular momentum and I is the moment of inertia of the molecule. L is quantized in levels separated by energy $\approx \hbar$, hence, $E_r \approx \hbar^2/Ma^2 = (m/M)E_e$. So, even for lighter molecules like N₂, where we have $(m/M)=3.89 \times 10^{-5}$, and energy of the nucleus is negligibly small.

In metallic systems with $E_e = 0eV$, strictly, this approximation is *not* valid. But, since in typical experiments the temperature range used is much lower than the Fermi temperature, excitation is generally confined in a narrow region around the Fermi surface and the electronic properties are little affected by this approximation.

Mathematically, this is a separation of variable

$$\Psi(\{\mathbf{r}_i\}, \{\mathbf{R}_I\}) = \phi(\{\mathbf{R}_I\}) \psi(\{\mathbf{r}_i\}, \{\mathbf{R}_I\})$$

Using this approximation in eqn. (2.1), we get

$$\begin{aligned} \mathcal{H} &= -\frac{\hbar^2}{2M_I} \sum_{\mathbf{R}_I} \nabla_{\mathbf{R}_I}^2 \{ \phi(\{\mathbf{R}_I\}) \psi(\{\mathbf{r}_i\}, \{\mathbf{R}_I\}) \} \\ &+ \psi(\{\mathbf{r}_i\}, \{\mathbf{R}_I\}) \left[\sum_{\mathbf{R}_I} \sum_{\mathbf{R}_J} \frac{Z^2 e^2}{|\mathbf{R}_I - \mathbf{R}_J|} \right] \phi(\{\mathbf{R}_I\}) \\ &+ \phi(\{\mathbf{R}_I\}) \left[-\frac{\hbar^2}{2m_e} \sum_{\mathbf{r}_i} \nabla_{\mathbf{r}_i}^2 + \sum_{\mathbf{r}_i} \sum_{\mathbf{r}_j} \frac{e^2}{|\mathbf{r}_i - \mathbf{r}_j|} - \sum_{\mathbf{R}_I} \sum_{\mathbf{r}_i} \frac{Ze^2}{|\mathbf{r}_i - \mathbf{R}_I|} \right] \psi(\{\mathbf{r}_i\}, \{\mathbf{R}_I\}) \\ &= E \phi(\{\mathbf{R}_I\}) \psi(\{\mathbf{r}_i\}, \{\mathbf{R}_I\}) \end{aligned} \tag{2.3}$$

Neglecting the smaller terms, we get a separable Schrödinger’s equation with two equation:

one for electrons

$$\left[-\frac{1}{2} \sum_{\mathbf{r}_i} \nabla_{\mathbf{r}_i}^2 + \sum_{\mathbf{r}_i} \sum_{\mathbf{r}_j} \frac{1}{|\mathbf{r}_i - \mathbf{r}_j|} - \sum_{\mathbf{R}_I} \sum_{\mathbf{r}_i} \frac{Z}{|\mathbf{r}_i - \mathbf{R}_I|} \right] \psi(\{\mathbf{r}_i\}) = E(\{\mathbf{R}_n\}) \psi(\{\mathbf{r}_i\}) \quad (2.4)$$

and one for ion-cores:

$$\left[-\frac{1}{2M_I} \sum_{\mathbf{R}_I} \nabla_{\mathbf{R}_I}^2 + \sum_{\mathbf{R}_I} \sum_{\mathbf{R}_J} \frac{Z^2}{|\mathbf{R}_I - \mathbf{R}_J|} + E(\{\mathbf{R}_I\}) \right] \phi(\{\mathbf{R}_J\}) = E\phi(\{\mathbf{R}_I\}) \quad (2.5)$$

in Hartree unit.

2.3 Density Functional Theory

Though the mathematical description of many electron system is given by eqn. (2.4), it has its own difficulties. Since the exact analytical solution has been possible for very few potentials even for a single particle and hence we have to depend upon approximate methods, such as variational principle or the perturbation theory. Alternatively, although we can adopt direct numerical solution in principle, difficulty arises due to the large number of variables ($3N$) involved in the wave-function $\psi(\mathbf{r}_1, \mathbf{r}_2, \dots, \mathbf{r}_N)$ and also in its interpretation.

Attempt to solve the problems due to (a) large number of variables (b) lack of easy interpretation and (c) the so called electron correlation has led to the development of newer approaches. An important class of methods has been based on the variational principle where we minimize the quantity $\tilde{E} = \langle \tilde{\psi} | H | \tilde{\psi} \rangle$. Using suitable forms for the trial function $\tilde{\psi}$ mainly guided by the one-particle orbital picture leading to single particle self-consistent field schemes like Hartree, Hartree-Fock and multi-configuration methods.

An alternative approach has been based on reduction to lower dimensions. Although the wave-function $\psi(\mathbf{r}_1, \mathbf{r}_2, \dots, \mathbf{r}_N)$ is a function of $3N$ variables, the expectation value $\bar{A} = \langle \psi | \hat{A} | \psi \rangle$ can be calculated through other derived quantities that depend on less number of variables, if \hat{A} is a sum of one- or two-particle operators, as is the case for the Hamiltonian.

Thus, for the ion-core-electron potential energy consisting of one-particle terms, we have

$$\begin{aligned} & \int \psi^*(\mathbf{r}_1, \mathbf{r}_2, \dots, \mathbf{r}_N) \sum_i v(\mathbf{r}_i) \psi(\mathbf{r}_1, \mathbf{r}_2, \dots, \mathbf{r}_N) d\mathbf{r}_1 d\mathbf{r}_2 \dots d\mathbf{r}_N \\ &= N \int d\mathbf{r}_1 v(\mathbf{r}_1) \int \psi^*(\mathbf{r}_1, \mathbf{r}_2, \dots, \mathbf{r}_N) \psi(\mathbf{r}_1, \mathbf{r}_2, \dots, \mathbf{r}_N) d\mathbf{r}_2 d\mathbf{r}_3 \dots d\mathbf{r}_N \end{aligned}$$

Here,

$$v(\mathbf{r}_i) = \sum_{\mathbf{R}_n} \frac{Z}{|\mathbf{r}_i - \mathbf{R}_n|} \quad \text{and} \quad V_{ie} = \left\langle \psi \left| \sum_{\mathbf{r}_i} v(\mathbf{r}_i) \right| \psi \right\rangle = \int d\mathbf{r} v(\mathbf{r}) \rho(\mathbf{r}) \quad (2.6)$$

valid for any single-particle multiplicative operator, where the single-particle density is defined as

$$\rho(\mathbf{r}_1) = N \int \psi^*(\mathbf{r}_1, \mathbf{r}_2, \dots, \mathbf{r}_N) \psi(\mathbf{r}_1, \mathbf{r}_2, \dots, \mathbf{r}_N) d\mathbf{r}_2 d\mathbf{r}_3 \dots d\mathbf{r}_N \quad (2.7)$$

Similarly, for two-particle multiplicative operators such as the electron-electron repulsion, we can write

$$V_{ee} = \left\langle \psi \left| \frac{1}{2} \sum_{i,j} \frac{1}{|\mathbf{r}_i - \mathbf{r}_j|} \right| \psi \right\rangle = \frac{1}{2} \int d\mathbf{r}_1 d\mathbf{r}_2 \frac{\Gamma_2(\mathbf{r}_1, \mathbf{r}_2)}{|\mathbf{r}_1 - \mathbf{r}_2|} \quad (2.8)$$

where the two-particle density is defined as

$$\Gamma_2(\mathbf{r}_1, \mathbf{r}_2) = N(N-1) \int \psi^*(\mathbf{r}_1, \mathbf{r}_2, \dots, \mathbf{r}_N) \psi(\mathbf{r}_1, \mathbf{r}_2, \dots, \mathbf{r}_N) d\mathbf{r}_3 \dots d\mathbf{r}_N \quad (2.9)$$

The reduced density functions can also be expressed as the expectation values of the corresponding density operators, viz.

$$\begin{aligned} \rho(\mathbf{r}) &= \left\langle \psi \left| \sum_i \delta(\mathbf{r} - \mathbf{r}_i) \right| \psi \right\rangle \\ \Gamma_2(\mathbf{r}_1, \mathbf{r}_2) &= \left\langle \psi \left| \sum_{i \neq j} \delta(\mathbf{r}_1 - \mathbf{r}_i) \delta(\mathbf{r}_2 - \mathbf{r}_j) \right| \psi \right\rangle \end{aligned}$$

For the kinetic energy term which involves differential operators, we can write

$$\begin{aligned}
T &= - \left\langle \psi \left| \frac{1}{2} \sum_i \nabla_i^2 \right| \psi \right\rangle \\
&= - \frac{N}{2} \int \psi^*(\mathbf{r}_1, \mathbf{r}_2, \dots, \mathbf{r}_N) \nabla_1^2 \psi(\mathbf{r}_1, \mathbf{r}_2, \dots, \mathbf{r}_N) d\mathbf{r}_1 d\mathbf{r}_2 d\mathbf{r}_3 \dots d\mathbf{r}_N \\
&= - \frac{N}{2} \int [\nabla_1^2 \psi^*(\mathbf{r}'_1, \mathbf{r}_2, \dots, \mathbf{r}_N) \psi(\mathbf{r}_1, \mathbf{r}_2, \dots, \mathbf{r}_N)]_{\mathbf{r}_1=\mathbf{r}'_1} d\mathbf{r}_1 d\mathbf{r}_2 d\mathbf{r}_3 \dots d\mathbf{r}_N \\
&= - \frac{1}{2} \int d\mathbf{r}_1 [\nabla_1^2 \gamma(\mathbf{r}_1; \mathbf{r}'_1)]_{\mathbf{r}_1=\mathbf{r}'_1}
\end{aligned} \tag{2.10}$$

with the first-order reduced density matrix (RDM) defined as

$$\gamma(\mathbf{r}_1; \mathbf{r}'_1) = N \int \psi^*(\mathbf{r}'_1, \mathbf{r}_2, \dots, \mathbf{r}_N) \psi(\mathbf{r}_1, \mathbf{r}_2, \dots, \mathbf{r}_N) d\mathbf{r}_2 d\mathbf{r}_3 \dots d\mathbf{r}_N \tag{2.11}$$

Clearly, the following relationships among the reduced density functions and matrices hold good.

$$\begin{aligned}
\rho(\mathbf{r}_1) = \gamma(\mathbf{r}_1; \mathbf{r}_1) \quad ; \quad \Gamma_2(\mathbf{r}_1, \mathbf{r}_2) = \Gamma_2(\mathbf{r}_1, \mathbf{r}_2; \mathbf{r}_1, \mathbf{r}_2) \quad ; \quad \gamma(\mathbf{r}_1; \mathbf{r}'_1) = \gamma^*(\mathbf{r}'_1; \mathbf{r}_1) \\
\int \rho(\mathbf{r}_1) d\mathbf{r}_1 = N \quad ; \quad \int \Gamma_2(\mathbf{r}_1, \mathbf{r}_2) d\mathbf{r}_1 d\mathbf{r}_2 = N(N-1) \\
\rho(\mathbf{r}_1) = \frac{1}{N-1} \int \Gamma_2(\mathbf{r}_1, \mathbf{r}_2) d\mathbf{r}_2
\end{aligned}$$

For spin-polarized situation, we have to include the spin dependence, viz.

$$\begin{aligned}
\rho(\mathbf{r}) \longrightarrow \rho(x) = \rho_\sigma(\mathbf{r}) \quad ; \quad \int d\mathbf{r} \longrightarrow \int dx = \sum_\sigma \int d\mathbf{r} \\
\rho(\mathbf{r}) = \rho_\uparrow(\mathbf{r}) + \rho_\downarrow(\mathbf{r}) \quad ; \quad m(\mathbf{r}) = \rho_\uparrow(\mathbf{r}) - \rho_\downarrow(\mathbf{r})
\end{aligned}$$

The total energy can thus be expressed in terms of the reduced density matrices (RDM) as

$$E[\rho, \gamma, \Gamma_2] = T[\gamma(\mathbf{r}_1; \mathbf{r}'_1)] + V_{ie}[\rho(\mathbf{r})] + V_{ee}[\Gamma_2(\mathbf{r}_1, \mathbf{r}_2)] + V_{nn} \tag{2.12}$$

which leads to the possibility of developing a quantum mechanics of many-electron systems in reduced space in terms of the RDM's bypassing the wave-function. One of the important requirements is the possibility of direct determination of RDM by minimizing the energy with respect to the RDM's for which the effect of Pauli exclusion principle has to be built-in into the RDM's. The existence of an antisymmetric ψ from which the RDM's can be obtained has to be guaranteed.

This is the so called N -representability problem which has to be solved by imposing necessary and sufficient conditions on $\gamma_1(\mathbf{r}_1; \mathbf{r}'_1)$ and $\Gamma_2(\mathbf{r}_1, \mathbf{r}_2)$, which are unfortunately not yet known. The N -representability conditions on $\rho(\mathbf{r})$ are however known and are very simple, viz.

$$\int \rho(\mathbf{r})d\mathbf{r} = N; \quad \rho(\mathbf{r}) \geq 0. \quad (2.13)$$

This makes the single-particle density (simplest reduced quantity) a promising candidate for the formulation of quantum mechanics in reduced space. Some of the many advantages for the electron density $\rho(\mathbf{r})$ to be the basic variable are: (a) it is a function in 3D space in which we live and perceive (b) it is simpler to tabulate and plot (c) it provides a better visualization (d) it is an experimental observable, thus enabling one to compare the results of theoretical calculations directly with experiments.

Thus, the question now is whether it is possible to develop a quantum theory in terms of density alone bypassing the wave-function, for which one has to ensure if (a) the density contains sufficient information (b) calculation of the properties and the energy is possible from the density alone (c) it is possible to develop a method for the direct calculation of density.

The possibility of a density description of many-electron systems has been explored by many people leading to the so called density functional theory (DFT). Although the first DFT, namely, the Thomas-Fermi [Thomas, 1927; Fermi, 1927] method has existed since 1927, the birth of modern DFT has been through the formal proof of Hohenberg and Kohn [Hohenberg and Kohn, 1964] theorem.

Density Functional Theory (DFT) is the basis of most modern electronic structure calculations. It shows that a correlated many-body system can be solved by means of a scalar function of coordinate. Originating from crude approximation of Thomas and Fermi in 1927,

it came into usability when Hohenberg and Kohn proposed its modern form.

2.3.1 Hohenberg-Kohn Theorem

DFT is based on two theorems proposed by Hohenberg and Kohn [Hohenberg and Kohn, 1964],

Theorem 1. *For any system of interacting particles in an external potential V_{ext} , the potential V_{ext} is determined uniquely, except for a constant, by the ground state particle density $\rho_0(\mathbf{r})$.*

Theorem 2. *A universal functional for the energy $E[n]$ in terms of $\rho(\mathbf{r})$ can be defined, valid for any V_{ext} . For any particular V_{ext} , the exact ground state energy of the system is the global minima of the functional, and the $\rho(\mathbf{r})$ that minimizes the functional is the exact ground state density $\rho_0(\mathbf{r})$.*

i.e. for any trial density $\tilde{\rho}$ satisfying $\tilde{\rho} \geq 0$ and $\int \tilde{\rho} d\mathbf{r} = N$,

$$E[\rho_0] \leq E[\tilde{\rho}]$$

Thus, the Hohenberg-Kohn total energy functional

$$\begin{aligned} E_{HK} &= \mathcal{T}[\rho] + \mathcal{E}_{int}[\rho] + \int \mathcal{V}_{ext}\rho(\mathbf{r})d^3r + E_{II} \\ &\equiv \mathcal{F}_{HK}[\rho] + \int \mathcal{V}_{ext}\rho(\mathbf{r})d^3r + E_{II} \end{aligned} \quad (2.14)$$

where, $\mathcal{F}_{HK}[\rho] = \mathcal{T}[\rho] + \mathcal{E}_{int}[\rho]$ is a universal functional and E_{II} is ion-ion repulsion. The ground state electron density is one that minimizes $E[\rho]$ via variational principle,

$$\begin{aligned} \delta \left\{ E_{HK}[\rho] - \mu \left[\int \rho(\mathbf{r})d\mathbf{r} - N \right] \right\} &= 0 \\ \Rightarrow \mu &= \mathcal{V}_{ext} + \frac{\partial \mathcal{F}_{HK}[\rho]}{\partial \rho(\mathbf{r})} \end{aligned} \quad (2.15)$$

Though these two theorems give a one-to-one correspondence between $\rho(\mathbf{r})$ and Ψ_0 , the ground state wave function, it had few limitations, like:

- No prescription to determine Ψ_0 for a given ρ_0 .
- Not applicable to degenerate state.

Another problem with this formulation was that the density ρ was *V-representable*; though almost all problems in condensed matter physics can be formulated via this type of density, it is not the general one. In a series of papers, Levy [Levy, 1979] and Lieb [Lieb, 1982] introduced an alternative definition of the Hohenberg-Kohn theorems. This is a two step minimization, where instead of searching the full N-particle Hilbert space for the trial density, we *constrain* ourselves only to the space of trial wave functions that give the density $\rho_0(\mathbf{r})$.

2.3.2 The Kohn-Sham Equation

From eqn. (2.15), we are left with two problems: how to calculate $\mathcal{T}[\rho]$ and the non-classical part of \mathcal{V}_{int} . Thomas-Fermi model did this calculation using drastic approximation, too crude to have any physical value. In their celebrated paper, Kohn and Sham [Kohn and Sham, 1965] took rather indirect approach to calculate $\mathcal{T}[\rho]$,

$$\begin{aligned}\mathcal{T}_s[\rho] &= \sum_i^N \left\langle \psi_i \left| -\frac{1}{2} \nabla^2 \right| \psi_i \right\rangle \\ \rho(\mathbf{r}) &= \sum_i^N \sum_s |\psi_i(\mathbf{r}, s)|^2\end{aligned}\tag{2.16}$$

where, $\mathcal{T}_s[\rho]$, the single particle kinetic energy, *exactly* describes the *non-interacting* kinetic energy. So, the Hohenberg-Kohn Energy in eqn. (2.14) turns out to be,

$$E_{KS} = \mathcal{T}_s[\rho] + \int \mathcal{V}_{ext}(\mathbf{r})\rho(\mathbf{r})d\mathbf{r} + E_{Hartree} + E_{II} + E_{xc}[\rho]\tag{2.17}$$

where

$$\begin{aligned}E_{xc}[\rho] &= \mathcal{F}_{HK}[\rho] - \mathcal{T}_s[\rho] - E_{Hartree}[\rho] \\ &= \langle \mathcal{T} \rangle - \mathcal{T}_s[\rho] + \langle \mathcal{V}_{int} \rangle - E_{Hartree}[\rho]\end{aligned}\tag{2.18}$$

is the exchange-correlation energy, that includes *all* many-body effect the system has. So now we see that E_{KS} is a functional of orbital \mathcal{T}_s and density. Implementing eqn. (2.15) gives:

$$\frac{\delta E_{KS}}{\delta \psi_i} = \frac{\delta \mathcal{T}_s}{\delta \psi_i} + \left[\frac{\delta E_{ext}}{\delta \rho} + \frac{\delta E_{Hartree}}{\delta \rho} + \frac{\delta E_{xc}}{\delta \rho} \right] \frac{\delta \rho}{\delta \psi} = 0 \quad (2.19)$$

which results in a Schrödinger like Kohn-Sham equation:

$$H_{KS}\psi_i = \varepsilon\psi_i \quad (2.20)$$

where

$$H_{KS} = -\frac{1}{2}\nabla^2 + V_{KS} \quad (2.21)$$

with

$$V_{KS} = \mathcal{V}_{ext} + \mathcal{V}_{Hartree} + \mathcal{V}_{xc} \quad (2.22)$$

eqn. (2.20)-(2.22) are the famous Kohn-Sham Equation.

We solve the Kohn-Sham equation using a self-consistent iterative scheme as shown in the Figure 2.2

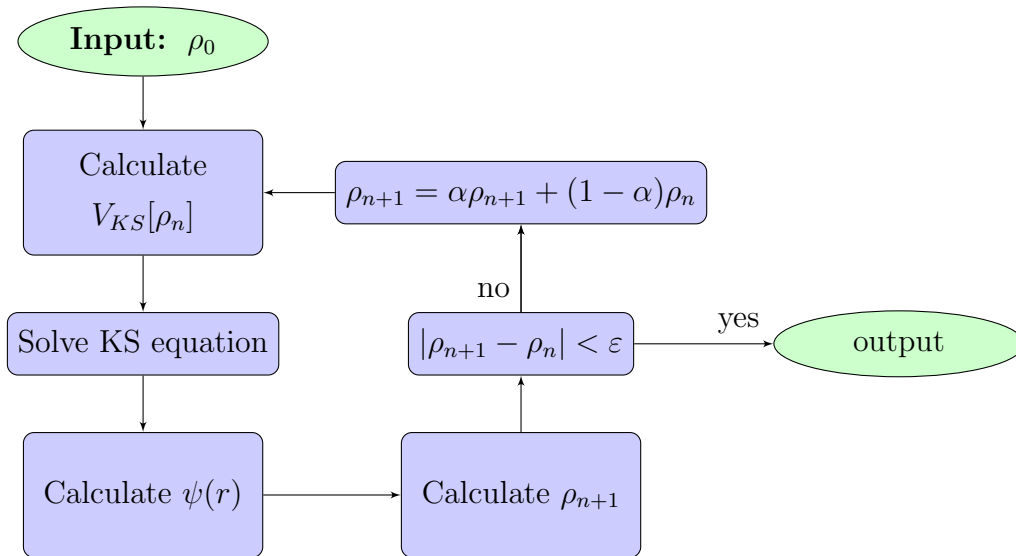


Figure 2.2: Simple flowchart for solving Kohn-Sham eqn. (2.20)-(2.22).

2.3.3 Exchange and Correlation Potential

The many body effect of Kohn-Sham equation is included solely in \mathcal{V}_{xc} and can be approximated as local or nearly local functional of density as

$$E_{xc} = \int \rho[\mathbf{r}] \epsilon_{xc}[\mathbf{r}, \rho] d\mathbf{r}.$$

But the term $\epsilon_{xc}[\mathbf{r}, \rho]$, the exchange-correlation density, is not uniquely defined. We have to approximate its value and obtain from other methods. For solids, there are calculations using quantum Monte Carlo simulation with a variational wavefunction, which shows that the exchange term dominates over correlation. In their paper, Kohn-Sham [Hohenberg and Kohn, 1964] chooses the term to that of homogeneous electron gas. It is easy but very successful approximation as in this limit the exchange-correlation term is a local functional of ρ . This is called **local density approximation**(LDA). Here E_{xc} becomes,

$$E_{xc}[\rho] = \int \rho[\mathbf{r}] \epsilon_{xc}^{hom}[\mathbf{r}, \rho] d\mathbf{r} \tag{2.23}$$

Since, for homogeneous gas, this term is universal, dependent of ρ only, we can have very accurate calculation of this using Monte Carlo method [Ceperley and Alder, 1980].

LDA has been used very extensively! Though it is known from its theoretical foundation and multiple studies that LDA fails for atomic systems or that of strongly correlated systems, it is also known to give remarkably correct results for metallic systems, specially for extended systems. Since all of our calculations are on metallic alloys, we have taken this level of approximation in $E_{xc}[\rho]$.

2.3.4 Extension to spin system

DFT as outlined above, is based on the charge density ρ only, it is easy to extend it for spin polarized systems, which is absolutely essential to study magnetic properties. We just decompose the density ρ into two independent spin density $\rho = \rho_{\uparrow} + \rho_{\downarrow}$ and eqn. (2.20) becomes,

$$H_{KS}^{\sigma} \psi_i^{\sigma} = \epsilon^{\sigma} \psi_i^{\sigma} \tag{2.24}$$

where σ indicates the spin components (\uparrow or \downarrow). Here we also get the magnetization density as

$$\zeta(\mathbf{r}) = \rho_{\uparrow}(\mathbf{r}) - \rho_{\downarrow}(\mathbf{r}) \quad (2.25)$$

This very simple and logical extension of K-S eqn. (2.20)-(2.22) enables us to study magnetic systems.

2.4 Solving Kohn Sham equation

There are three different methods of calculating independent particle electronic states in condensed matter theory.

Plane wave methods: General approach to solve Poisson's equation. Very efficient method.

Localized atomic orbital or LCAO: Atomic features and localized descriptions are very well explained within this method.

Atomic Sphere Methods: The most general approach. The basic approach is to divide the space between atomic region and inter-atomic region.

The top two method provides fixed energy based basis set, where the third one is partial wave-like basis. We have chosen this type of solution to solve the Kohn-Sham equation.

2.4.1 LMTO method

The first approximation in using *atomic sphere method*, is that the potential in the crystal has a local spherical symmetry and extremely flat potential in interstitial space. This approximation is called atomic sphere approximation(ASA) as shown schematically in Figure 2.3.

The wave function at energy E can be written as

$$\psi_j(\mathbf{k}, \mathbf{r}) = \sum_{lm} b_{Rlm}^{jk} \psi_{Rl}(E, |\mathbf{r} - \mathbf{R}|) i^l Y_l^m(\widehat{\mathbf{r} - \mathbf{R}}) \quad (2.26)$$

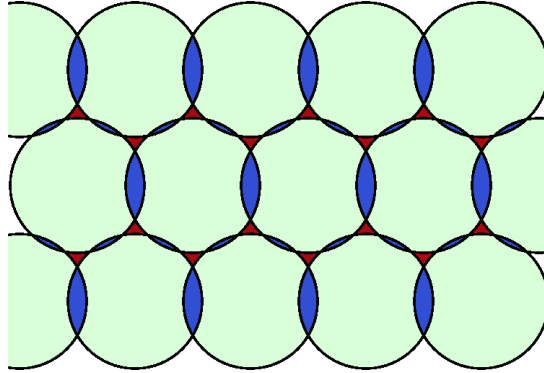


Figure 2.3: Atomic sphere approximation: The scatterer is of the same volume as Wigner-Seitz cell; Blue regions are interatomic space; Brown region is overlap.

where b_{Rlm}^{jk} is the expansion coefficient of the partial wave, Y_l^m is a spherical harmonics, i^l is a phase factor and ψ_{Rl} a solution of radial Schrödinger equation

$$\left[-\frac{d^2}{dr^2} + \frac{l(l+1)}{r^2} + v(r) - E \right] r\psi_l(E, r) = 0 \quad (2.27)$$

Phase conventions of [Condon and Shortley, 1935] is used for spherical harmonics. Wigner and Seitz [Wigner and Seitz, 1933, 1934] suggested the spherically symmetric potential to extend until the boundary of atomic polyhedron. The wave functions in solid is then expressed as Bloch sum of eqn. (2.26)

$$\psi_j(\mathbf{k}, \mathbf{r}) = \sum_{\mathbf{R}} e^{i\mathbf{k}\cdot\mathbf{R}} \sum_{lm} b_{lm}^{jk} \theta(\mathbf{r} - \mathbf{R}) \psi_l(E, |\mathbf{r} - \mathbf{R}|) i^l Y_l^m(\widehat{\mathbf{r} - \mathbf{R}}) \quad (2.28)$$

where θ is unity inside atomic sphere and zero outside. Though this “cellular” method turned out to be too tough for applying boundary conditions, it gave rise to KKR (named after Korringa, Kohn and Rostoker) (and LMTO) method and Wigner-Seitz rule of energy band. Slater [Slater, 1937] in his Augmented Plane-wave(APW), inscribed a *muffin-tin*(MT) sphere in each atomic sphere. Inside the sphere, the potential is spherically symmetric and wave functions are expanded as Wigner-Seitz partial wave.

Korringa [Korringa, 1947], Kohn and Rostoker [Kohn and Rostoker, 1954] expand the MT spheres similar to cellular and APW. The interstitial potential is flat and wave functions are

expanded as phase shifted spherical wave. Boundary conditions are expressed as condition for self-consistent multiple scattering between the MT spheres. Andersen[Andersen, 75] linearizes this method which is one of the most used method of solving the KS equation. I have used LMTO method in my work, and the method has been discussed in detail in next section. §2.4.2¹.

2.4.2 KKR-ASA

We will start from an energy dependent orbital

$$\chi_{lm}(E, \mathbf{r}) = i^l Y_l^m \begin{cases} \psi_l(E, r) + p_l(E) \left(\frac{r}{S}\right)^l & r < S \\ \left(\frac{S}{r}\right)^{l+1} & r > S \end{cases} \quad (2.29)$$

where $\psi_l(E, r)$ is the solution of eqn. (2.27) and S is the radius of atomic sphere. This *muffin-tin orbital*(MTO) is regular, continuous and differentiable in all the space. The potential function $p_l(E, r)$ and normalization of $\psi_l(E, r)$ requires continuity and differentiability at the sphere i.e.

$$p_l(E) = \frac{D_l(E) + l + 1}{D_l(E) - l} \quad (2.30)$$

where

$$D_l(E) = \frac{S}{\psi_l(E, S)} \left. \frac{\partial \psi_l(E, r)}{\partial r} \right|_{r=S} \quad (2.31)$$

is the logarithmic derivative function.

The tail of the orbital, $\left(\frac{S}{r}\right)^{l+1}$ is the solution of Poisson's equation $\nabla^2 X = 0$, i.e. has zero kinetic energy. So, the tail centered at \mathbf{R} may be expanded around the origin in terms of phase shifted spherical harmonics, yielding,

$$\sum_{\mathbf{R} \neq 0} e^{i\mathbf{k} \cdot \mathbf{R}} \left(\frac{S}{|\mathbf{r} - \mathbf{R}|} \right)^{l+1} i^l Y_l^m(\widehat{\mathbf{r} - \mathbf{R}}) = \sum_{l'm'} \frac{-1}{2(2l' + 1)} \left(\frac{r}{S} \right)^{l'} i^{l'} Y_{l'}^{m'}(\hat{r}) S_{l'm', lm}^{\mathbf{k}} \quad (2.32)$$

¹This and later discussion on LMTO is based on [Skriver, 1984]

where $S_{l'm',lm}^{\mathbf{k}}$ is the canonical structure constant, converges inside the sphere of nearest neighbor.

The first term of MTO $i^l Y_l^m(\hat{r})\psi_l(E, r)$ is already a solution of eqn. (2.27) and is the correct one-center expansion at the origin. For any other sphere, therefore, the term is

$$\sum_{lm} a_{lm}^{j\mathbf{k}} i^l Y_l^m(\hat{r})\psi_l(E, r) \quad (2.33)$$

provided tails from all other sphere cancel the term

$$\sum_{lm} a_{lm}^{j\mathbf{k}} i^l Y_l^m(\hat{r})p_l(E) \left(\frac{r}{S}\right)^l \quad (2.34)$$

where $a_{lm}^{j\mathbf{k}}$ is the expansion coefficient of MTO. From eqn. (2.32), the condition for this *tail cancellation* is

$$\sum_{lm} [P_l(E)\delta_{ll'}\delta_{mm'} - S_{l'm',lm}^{\mathbf{k}}] a_{lm}^{j\mathbf{k}} = 0 \quad (2.35)$$

where P_l is defined as

$$P_l(E) = 2(2l + 1) \frac{D_l(E) + l + 1}{D_l(E) - 1} \quad (2.36)$$

Eqn. (2.35) is the KKR-ASA equation which gives solution for eigenvectors $a_{lm}^{j\mathbf{k}}$ when

$$\det [P_l(E)\delta_{ll'}\delta_{mm'} - S_{l'm',lm}^{\mathbf{k}}] = 0 \quad (2.37)$$

This is the secular determinant of KKR-ASA.

2.4.3 Muffin Tin Orbitals

The basic assumption of Muffin-Tin(MT) orbital is that in the neighborhood of an ion-core the potential seen by the electron in a solid is not very different from that of the atomic ion-core. This neighborhood is spherically symmetric with radius S centered at \mathbf{R} . In the interstitial region the potential is flat, called *muffin-tin potential* (V_{MTZ}).

For one atom per unit cell, the effective potential is

$$V_{MT}(\mathbf{r} - \mathbf{R}) = \begin{cases} v(|\mathbf{r} - \mathbf{R}|) - V_{MTZ} & r \leq S \\ 0 & r \geq S \end{cases} \quad (2.38)$$

is the Muffin-Tin Potential where \mathbf{R} and \mathbf{r} are the positions of the ion-cores and an electron respectively. The Hamiltonian is therefore given by

$$H = -\nabla^2 + \sum_{\mathbf{R}} V_{MT}(|\mathbf{r} - \mathbf{R}|) - \kappa^2 + E \quad (2.39)$$

where κ is the kinetic energy in the extended region, $\kappa^2 = E - V_{MTZ}$. we solve the eqn. (2.27) numerically to obtain the radial part $\psi_l(E, r)$

$$\psi_L(\varepsilon, \kappa, \mathbf{r}) = i^l Y_L(\hat{r}) \begin{cases} \psi_l(\varepsilon, r) + \kappa \cot(\eta_l(\varepsilon)) j_l(\kappa r) & r \geq S \\ \kappa n_l(\kappa r) & r \leq S \end{cases} \quad (2.40)$$

and in defining the basis set:

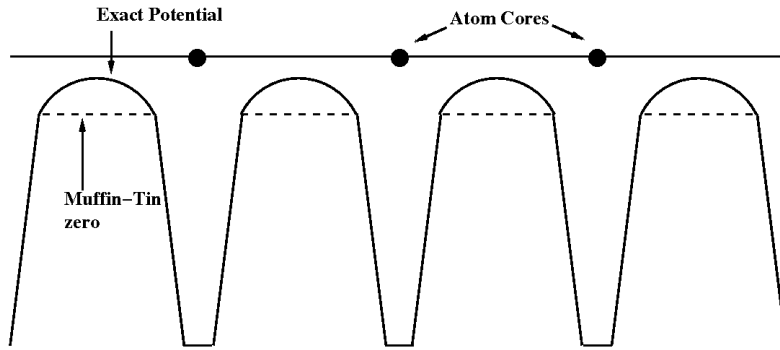


Figure 2.4: The muffin-tin potential

$$\chi_L^{MTO}(\varepsilon, \kappa, \mathbf{r}) = i^l Y_L(\hat{r}) \begin{cases} \psi_l(\varepsilon, r) + \kappa \cot(\eta_l(\varepsilon)) j_l(\kappa r) & r \leq S \\ \kappa n_l(\kappa r) & r \geq S \end{cases} \quad (2.41)$$

where S is the muffin-tin sphere radius. j_l and n_l are the spherical Bessel and Neumann function, defined as

$$j_l(\kappa r) \rightarrow \begin{cases} \frac{(\kappa r)^l}{(2l+1)!!} & \kappa r \rightarrow 0 \\ \frac{\sin(\kappa r + l\pi/2)}{\kappa r} & r \rightarrow \infty \end{cases} \quad (2.42)$$

$$n_l(\kappa r) \rightarrow \begin{cases} -\frac{(2l-1)!!}{(\kappa r)^{l+1}} & \kappa r \rightarrow 0 \\ -\frac{\cos(\kappa r + l\pi/2)}{\kappa r} & r \rightarrow \infty \end{cases} \quad (2.43)$$

which means j_l is regular both at origin and at ∞ , where n_l is regular at ∞ only and diverges at origin.

This yields a bound state *envelop function* which is real, and regular both inside (since $j_l(\kappa r)$ is regular at origin) and outside (since $n_l(\kappa r)$ is regular at infinity) the sphere. The inclusion of $j_l(\kappa r)$ in the single particle basis set includes the effect of neighbours so that the minimal basis set is capable of describing the full system. Anderson's method of linearization [Andersen, 75; Andersen et al., 1987] shows that the basis can be written as

$$\chi_{RL}^\alpha = \phi_{RL}(r_R) + \sum \dot{\phi}_{R'L'}^\alpha(r'_R) h_{R'L',RL}^\alpha \quad (2.44)$$

where $\dot{\phi}_{R'L'}^\alpha(r'_R)$ are linear combination of ϕ and $\dot{\phi}$, given as

$$\dot{\phi}_{R'L'}^\alpha = \dot{\phi}_{R'L'} + \phi_{R'L'} o^\alpha \quad (2.45)$$

where o^α is overlap matrix and Hamiltonian matrix h^α is defined as

$$h^\alpha = C^\alpha - \varepsilon_\nu + (\Delta^\alpha)^{1/2} S^\alpha (\Delta^\alpha)^{1/2}. \quad (2.46)$$

C^α and Δ^α are the potential parameters defined as

$$C^\alpha = \varepsilon_\nu - \frac{P^\alpha(\varepsilon_\nu)}{\dot{P}^\alpha(\varepsilon_\nu)}, \quad (\Delta^\alpha)^{1/2} = \frac{1}{\dot{P}^\alpha(\varepsilon_\nu)} \quad (2.47)$$

These are called band center and band width respectively.

Each set of α is also characterized by screening parameters, found numerically by Andersen and Jepsen [Andersen and Jepsen, 1984]. The site independent constants are

$$\alpha = \left\{ \begin{array}{lll} 0.3458 & l = 0 & (s) \\ 0.0530 & l = 1 & (p) \\ 0.0107 & l = 2 & (d) \end{array} \right\} \quad (2.48)$$

LMTO, together with this screening parameters are called tight-binding (TB)-LMTO sets. Also, for the self consistency to achieve, a correction term, named combined correction is attached. The corresponding (corrected) Hamiltonian is given by

$$H = C^\alpha + (\Delta^\alpha)^{1/2} S^\alpha (\Delta^\alpha)^{1/2} - (\kappa^2 + v_0) \partial_{\kappa^2} h^\alpha \quad (2.49)$$

2.5 Recursion Technique

von Laue's theorem on black body [Von Laue, 1914] shows that, when heated, black bodies take on the color characteristic of their temperature and independent of composition. It also shows (as not by more popular Weyl's theorem) that surface of the cavity helps damping the electromagnetic wave exponentially with number of wavelength from the surface.

This is consistent with the concept of *locality* that it is independent of its surrounding. Friedel [Friedel, 1954] first showed the applicability of von Laue theorem in electronic structure of surfaces. With Cyrot-Lackmann [Cyrot-Lackmann, 1967] he also calculated the orbital projected density of states (PDOS) for various transition metals. Based on this *method of moments*, Haydock *et al* [Haydock et al., 1972] developed the *recursion method*. The locality effect in electronic states and their accuracy via recursion method was shown

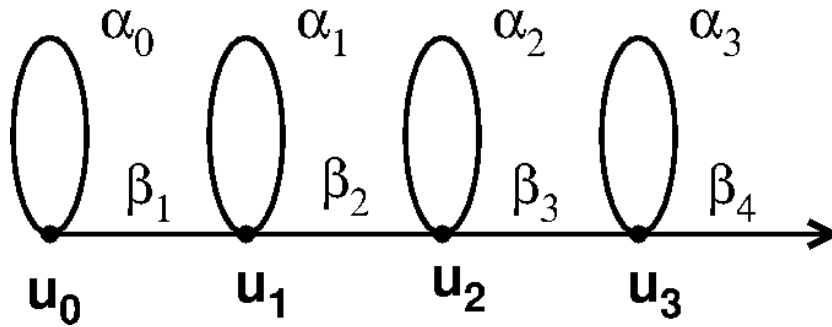


Figure 2.5: Graphical representation of chain model.

by Haydock and Kelly [Haydock and Kelly, 1973]

Recursion technique is based on the fact that any quantum-mechanical model can be transformed in one or more solvable chain model. The chain model is specified by a sequence of orthonormal orbitals of $\{u_n\}$ and two sets of real parameters $\{a_n\}$ and $\{b_n\}$ as shown in Figure 2.5 which describes the action of the Hamiltonian on the orbitals is given by three term recurrence relation:

$$Hu_n = \alpha_n u_n + \beta_{n+1} u_{n+1} + \beta_n u_{n-1} \quad (2.50)$$

where $u_1, u_2 \cdots u_n, \cdots$ are successively delocalized and u_{-1} is zero.

It can be realized that α_n is the self-interaction term and $\beta_{n\pm 1}$'s are nearest neighbour hopping term. We can directly solve this taking $\{\alpha, \beta\}$ as parameters using continued fraction as given in eqn. (2.53).

Lanczos [Lanczos, 1950] proposed an asymmetric version of eqn. (2.50) to solve the eigenvalue problem numerically. He tridiagonalized the matrix and iteratively obtained the sequence $\{\alpha, \beta\}$. A schematic diagram of recursion using Lanczos's method is shown in Figure 2.6

Formally the recursion starts with the initial condition : $u_1 = |0\rangle$ and the subsequent members of the basis are recursively generated :

$$u_n = H u_{n-1} - \alpha_n u_{n-1} - \beta_n^2 u_{n-2}$$

with $\alpha_n = (u_n, H u_n)/(u_n, u_n)$ and $\beta_n^2 = (u_n, u_n)/(u_{n-1}, u_{n-1})$

The recursion procedure tridiagonalizes the Hamiltonian. This allows us to obtain a representation of the resolvent of the Hamiltonian $G(z) = (zI - H)^{-1}$ as a continued fraction :

$$\langle 0|G(z)|0 \rangle = \frac{1}{z - \alpha_1 - \frac{\beta_1^2}{z - \alpha_2 - \frac{\beta_2}{z - \alpha_3 - \dots}}} \quad (2.51)$$

2.6 Augmented space formalism

2.6.1 The Configuration Space

Let us first start with clarifying the mathematical concept of the configuration space of a set of random variables. Depending on the nature of random variables, it assumes different values for different circumstances. The set containing all possible values that the random variables assume is called the configuration space of those random variables. If there are N independent binary random variables, then each random variable assumes two values. The set of all possible arrangements of these N variables contains 2^N sequences and hence the dimension of the space in this case is 2^N . The idea will be more clear if we take a particular

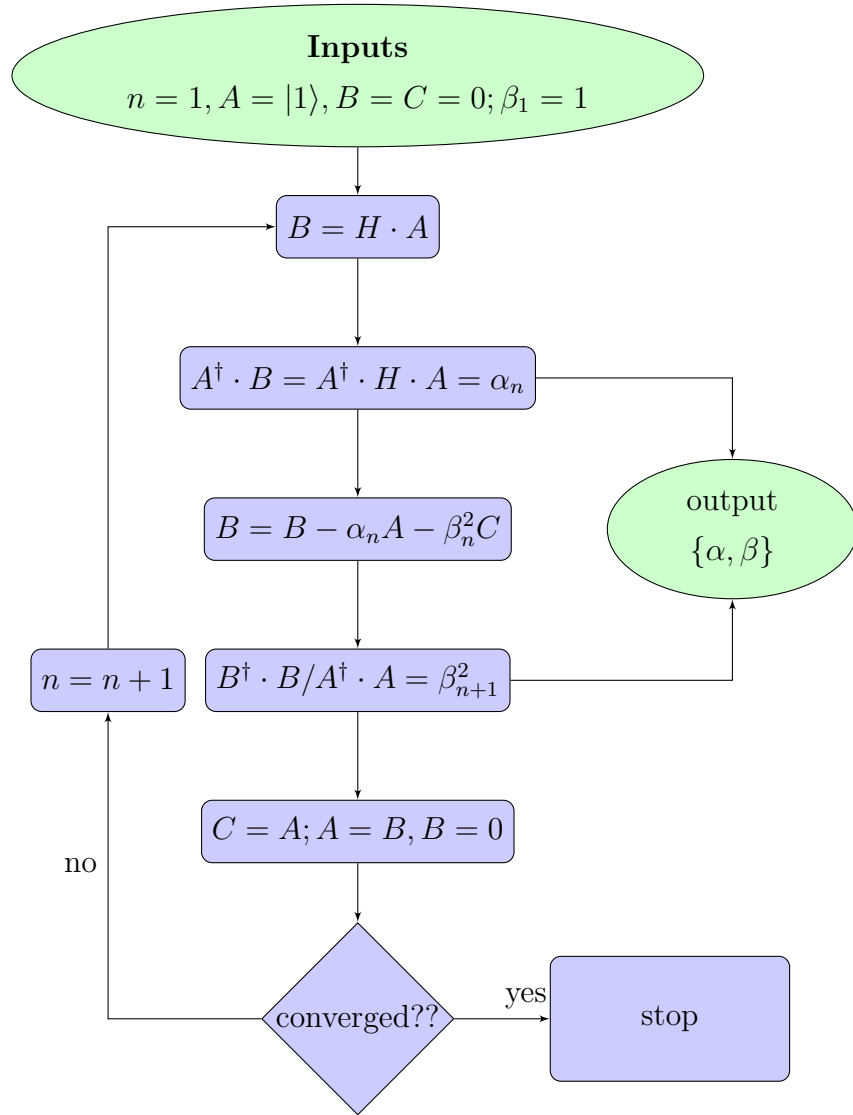


Figure 2.6: Scheme of recursion

example of the Ising model. This model consists of a set of *spins* $\{\sigma_R\}$ arranged on a discrete lattice labeled by $\{R\}$. Each spins can have two possible states or *configurations* : $|\uparrow_R\rangle$ and $|\downarrow_R\rangle$. For a single lattice site it only occupied by either $|\uparrow_R\rangle$ or $|\downarrow_R\rangle$, i.e the configuration space in this case is $[(|\uparrow_R\rangle), (|\downarrow_R\rangle)]$. Let us call this space ϕ_R . Now if we consider there are only two lattice sites, then possible distribution of spins in this two sites are $[(|\downarrow_1\rangle, |\downarrow_2\rangle),$

$(|\downarrow_1\rangle, |\uparrow_2\rangle), (|\uparrow_1\rangle, |\downarrow_2\rangle), (|\uparrow_1\rangle, |\uparrow_2\rangle)$, which is the configuration space for the sites with two random spins. The set of N-spins then have 2^N possible configurations, each of which can be written as a sequence of p-up states and (N-p) down-states. The number (N-p) is defined as the *cardinality* of the configuration and the sequence $\{C\}$ of sites $\{R_{i_1}, R_{i_2}, R_{i_3}, \dots, R_{i_{N_p}}\}$ where the down states sit is called the *cardinality sequence* of configuration. For example take a particular configuration of 6-spins $\{\uparrow_1 \downarrow_2 \uparrow_3 \downarrow_4 \downarrow_5 \downarrow_6\}$. It has a cardinality 4 and a cardinality sequence $\{2 \ 4 \ 5 \ 6\}$. Another configuration $\{\downarrow_1 \uparrow_2 \uparrow_3 \downarrow_4 \downarrow_5 \downarrow_6\}$ also has cardinality 4 but its cardinality sequence is $\{1 \ 4 \ 5 \ 6\}$ which is distinct from the previous one. For a set of N-spins, the configuration space Φ is of rank 2^N and can be written as the direct product of the configuration spaces of individual spins

$$\Phi = \prod_R^{\otimes} \phi_R$$

It is quite straight forward to generalize these ideas when random variables assumes more than two values. The configuration of an individual random variables can be labeled as $|\kappa_R\rangle$ where $\kappa_R = 1, 2, \dots, n$. The rank of ϕ_R is now n. Also the set of N-variables will have n^N possible configurations.

2.6.2 Augmented space formalism

The augmented space method was first introduced by Mookerjee is a feasible technique for carrying out configuration averaging in disordered systems. Here we shall discuss briefly about this formalism. Let us consider a set of independently distributed binary random variables $\{n_R\}$ with probability densities $p_R\{n_R\}$ and assume that the $p_R\{n_R\}$ has finite moment of all order. Clearly it is a reasonable assumption for almost all physical distributions. Since probability densities are positive definite functions therefore it can always be possible to express them as spectral densities of positive definite operator N_R as:

$$p_R(n_R) = -\frac{1}{\pi} \Im m \left[\langle \uparrow_R | (z\mathbf{I} - \mathbf{N}^R)^{-1} | \uparrow_R \rangle \right] \quad (2.52)$$

where $z \rightarrow n_R + i \delta ; \delta \rightarrow 0$, and $|\uparrow_R\rangle$ is the *average* state defined in such a way that for any related quantity containing n_R , $\langle \uparrow_R | \eta | \uparrow_R \rangle$ gives average value of η

Since the resolvent of \mathbf{N}^R $(z\mathbf{I} - \mathbf{N}^R)^{-1}$ is Herglotz, and $p_R\{n_R\}$ is assumed to be such that it has finite moment of all order exists, so one can expand it as a continued fractional form,

$$p_i(n_i) = -\frac{1}{\pi} \Im m \frac{1}{z - \alpha_0 - \frac{\beta_1^2}{z - \alpha_1 - \frac{\beta_2^2}{\ddots}}} \quad (2.53)$$

For a binary distribution, if n_R takes the value 0 and 1 with probabilities $x, y = (1 - x)$ then $p_R(n_R) = x\delta(n_R - 1) + y\delta(n_R)$ we have : $\alpha_0 = x, \alpha_1 = y$ and $\beta_1 = \sqrt{xy}$, and a representation of \mathbf{N}^R is

$$\begin{pmatrix} x & \sqrt{xy} \\ \sqrt{xy} & y \end{pmatrix}$$

In general if n_R takes k different values with probability x_k , then the configuration space is spanned by k states : $|k\rangle$ which are the eigenstates of N_R with eigenvalue k . In that case the *average state* $|\emptyset_R\rangle$, which is the equivalent of $|\uparrow_R\rangle$ is $\sum_k \sqrt{x_k}|k\rangle$ where x_k is the probability of the variable N_R to take the value k . The other members of the countable basis $|n\rangle$ may be obtained recursively from the average state through :

$$\begin{aligned} |0\rangle &= |\emptyset_R\rangle \\ \beta_1|1\rangle &= \mathbf{N}^R |0\rangle - \alpha_0|0\rangle \\ \dots & \quad \dots \quad \dots \quad \dots \\ \beta_n|n\rangle &= \mathbf{N}^R |n-1\rangle - \alpha_{n-1}|n-1\rangle - \beta_{n-1}|n-2\rangle \end{aligned}$$

In this basis, the operator \mathbf{N}^R thus has the tridiagonal form,

$$\begin{pmatrix} \alpha_0 & \beta_1 & 0 & 0 & 0 & \dots \\ \beta_1 & \alpha_1 & \beta_2 & 0 & 0 & \dots \\ 0 & \beta_2 & \alpha_2 & \beta_3 & 0 & \dots \\ 0 & 0 & \beta_3 & \alpha_3 & \beta_4 & \dots \\ \dots & \dots & \dots & \dots & \dots & \dots \end{pmatrix}$$

We can see that there is a close relationship between the above procedure and the recursion method described in the previous chapter. This is not surprising, since the projected density of states and the probability density are both positive definite and integrable functions. and in both the cases finite moments to all orders exists.

2.6.3 Augmented Space Theorem

The problem addressed involves the configuration averaging of a function of many independent random variables. e.g. $\ll f(\{n_R\}) \gg$ where R labels a set of lattice points. The first step is to associate with each random variable n_R an operator N^R such that the spectral density of this operator is the probability density of the random variable :

$$p(n_R) = -(1/\pi) \langle \uparrow_R | (n_R I - N^R)^{-1} | \uparrow_R \rangle$$

Also to each variable n_R there is associated a *configuration* space ϕ_R spanned by the *states* $\{| \uparrow_R \rangle\}$ then the augmented space theorem states that the average of any physical quantity $f(n_R)$, which is a function of the set of random variables $\{n_R\}$ is given by

$$\ll f(\{n_R\}) \gg = \langle \emptyset | \tilde{\mathbf{f}}(\{\mathbf{N}^R\}) | \emptyset \rangle \quad (2.54)$$

where $\tilde{\mathbf{f}}(\{\mathbf{N}^R\})$ is an operator which is a functional of $\{\mathbf{N}^R\}$ and has the same form as function $f(\{n_R\})$ of n_R has. Further, $|\emptyset\rangle = \prod_R^\otimes | \uparrow_R \rangle$ is the *average configuration state* in the product space $\Phi = \prod_R^\otimes \phi_R$. Therefore information about all possible configurations of the disordered system with random variables n_R are kept in the product space Φ . The statement of the theorem will be clear if we see the following mathematical steps.

Let us start with a function $f(n_R)$ of a single random variable n_R . The generalization for a function of the set of many random variables is quite straight forward. The average value of $f(n_R)$ can be expressed as:

$$\begin{aligned} \ll f(n_R) \gg &= \int_{-\infty}^{\infty} f(n_R) p_R(n_R) dn_R \\ &= -\frac{1}{\pi} \Im \int_{-\infty}^{\infty} f(n_R) \langle \uparrow_R | (n_R I - N^R)^{-1} | \uparrow_R \rangle dn_R \end{aligned}$$

Since the eigen vectors of the operator N^R on the configuration space is a complete set, we can write

$$\ll f(n_R) \gg = -\frac{1}{\pi} \Im m \sum_k \sum_{k'} \int_{-\infty}^{\infty} f(n_R) \langle \uparrow_R | k \rangle \langle k | (n_R I - \mathbf{N}^R)^{-1} | k' \rangle \langle k' | \uparrow_R \rangle dn_R$$

But $(n_R I - \mathbf{N}^R)^{-1}$ is diagonal in the eigen basis of N^R and is equal to $\frac{\delta_{kk'}}{n_R - k}$, so

$$\begin{aligned} \ll f(n_R) \gg &= \sum_k \int_{-\infty}^{\infty} f(n_R) \langle \uparrow_R | k \rangle \left[-\frac{1}{\pi} \Im m (n_R - k)^{-1} \right] \langle k | \uparrow_R \rangle dn_R \\ &= \langle \uparrow_R | \sum_k | k \rangle \int_{-\infty}^{\infty} [f(n_R) \delta(n_R - k) dn_R] \langle k | \uparrow_R \rangle \\ &= \langle \uparrow_R | \{ \sum_k | k \rangle f(k) \langle k | \} | \uparrow_R \rangle \end{aligned} \tag{2.55}$$

Now $\sum_k | k \rangle f(k) \langle k |$ is nothing but the spectral representation of the functional $\tilde{\mathbf{f}}(\mathbf{N}^R)$ of the operator N^R constructing by simply replacing the variable n_R with the associated operator \mathbf{N}^R in $f(n_R)$. Hence

$$\ll f(n_R) \gg = \langle \emptyset_R | \tilde{\mathbf{f}}(\mathbf{N}^R) | \emptyset_R \rangle \tag{2.56}$$

In general if there are independent random variables $\{n_R\}$ involved then the joint probability distribution is given by :

$$P(n_{R_1}, n_{R_2}, \dots, n_{R_i}, \dots) = \prod_i p_i(n_{R_i})$$

Proceeding in the same way we shall get average of functions of the set of random variables as.

$$\ll f(\{n_R\}) \gg = \langle \emptyset | \tilde{\mathbf{f}}(\{\tilde{\mathbf{N}}^R\}) | \emptyset \rangle$$

The operator $\tilde{\mathbf{N}}^R$ are built up from the operators \mathbf{N}^R as :

$$\tilde{\mathbf{N}}^R = \mathbf{I} \otimes \mathbf{I} \otimes \dots \otimes \mathbf{N}^R \otimes \mathbf{I} \otimes \dots$$

and $|\emptyset\rangle$ is the average state in the full configuration space Φ .

Clearly this is a very powerful theorem as it reduces the problem of configuration averaging to just a calculation of a spatial matrix element of an operator in the configuration space constructed according to the given prescription above by using probability distribution of the random variables. One can visualize in a way that the space where disordered function or operators are defined is extended to a bigger space by including the configuration space and in this enlarged space functions or operators are ordered one. In this formalism any approximation has not yet been done so far for averaging, therefore the expressions are exact. Also the formalism preserves all intrinsic properties of the function for example in case of Green's function Herglotz properties are preserved which ensures positive density of states. One of the main advantages of this formalism is that we can generalize it also for a system with correlated random variables. In practice there are lots of alloys where this kind of randomness exists which comes mainly due to the different chemical affinities of the constituent atoms. Formulation and use of generalized version of this formalism will be discussed in our subsequent chapter. In the following section we shall discuss how to perform configuration averaged electronic structure calculations for a real system using augmented space formalism.

2.6.4 Augmented space recursion in TB-LMTO formulation

We have already showed in our previous section that the augmented space theorem maps a disordered operator described in a space on to an ordered function in the augmented space. For a real physical system the disordered Hamiltonian defined in a real Hilbert space maps onto the configuration space Ψ which is nothing but the direct product of the real Hilbert space and the configuration space of the random variables. i.e. $\Psi = \mathcal{H} \otimes \oplus$ If the binary disordered system consisting of N number of sites then the dimension of Ψ is $N \times 2^N$. For the calculation of real binary disordered alloy using TB-LMTO method, we first need to express the TB-LMTO Hamiltonian in the augmented space Ψ .

In terms of potential parameter and screened structure matrix, up to the second-order

TB-LMTO Hamiltonian in the most localized β representation is expressed as:

$$\begin{aligned} \mathcal{H} &= E_\nu + h - hoh & (2.57) \\ \text{with } h &= \sum_{\nu} (C_\nu - E_\nu) \mathcal{P}_\nu + \sum_{\nu\nu'} \Delta_\nu^{1/2} S_{\nu\nu'} \Delta_{\nu'}^{1/2} \mathcal{T}_{\nu\nu'} \end{aligned}$$

where ν, ν' are the composite indices of the position(R) and orbital(L) quantum numbers and $\mathcal{P}_\nu = |\nu\rangle\langle\nu|$, $\mathcal{T}_{\nu\nu'} = |\nu\rangle\langle\nu'|$ are projection and translation operators respectively in the Hilbert space spanned by the tight binding basis $\{|\nu\rangle\}$. Now if we only consider diagonal disordered then C , Δ , and o are random at each site and one can express them in terms of the binary random variables n_R as :

$$\begin{aligned} \tilde{C}_\nu &= C_\nu^A n_R + C_\nu^B (1 - n_R) &= C_\nu^B + \delta C_\nu n_R \\ \Delta_\nu^{1/2} &= (\Delta^A)_\nu^{1/2} n_R + (\Delta^B)_\nu^{1/2} (1 - n_R) &= (\Delta^B)_\nu^{1/2} + \delta \Delta_\nu^{1/2} n_R \\ \tilde{o}_\nu &= o_\nu^A n_R + o_\nu^B (1 - n_R) &= o_\nu^B + \delta o_\nu n_R \end{aligned}$$

where $\delta C_\nu = C_\nu^A - C_\nu^B$ and so on

The representation of the Hamiltonian in the augmented space can be obtain simply by replacing the local site occupation variable $\{n_R\}$ by corresponding operator $\{N^R\}$. Hence the form of the first order Hamiltonian in the augmented space is

$$\begin{aligned} \tilde{\mathcal{H}} &= \sum_{\nu} (C_\nu^B \tilde{\mathcal{I}} + \delta C_\nu N^R) \otimes \mathcal{P}_\nu \\ &+ \sum_{\nu\nu'} [(\Delta^B)_\nu^{1/2} \tilde{\mathcal{I}} + \delta \Delta_\nu^{1/2} N^R] S_{\nu\nu'} [(\Delta^B)_{\nu'}^{1/2} \tilde{\mathcal{I}} + \delta \Delta_{\nu'}^{1/2} N^R] \otimes \mathcal{T}_{\nu\nu'} \end{aligned} \quad (2.58)$$

We have already shown that in $\{|\uparrow_R\rangle\}$ basis N^R has the representation of

$$N^R = x \mathcal{P}_\uparrow^R + y \mathcal{P}_\downarrow^R + \sqrt{xy} (\mathcal{T}_{\uparrow\downarrow}^R + \mathcal{T}_{\downarrow\uparrow}^R) \quad (2.59)$$

where $\mathcal{P}_\uparrow^R = |\uparrow_R\rangle\langle\uparrow_R|$ and $\mathcal{T}_{\uparrow\downarrow}^R = |\uparrow_R\rangle\langle\downarrow_R|$ are the projection and transfer operator respectively in the configuration space Φ .

Now replacing the form of N^R in eqn. (2.59) in the Hamiltonian in eqn. (2.58) we get the Hamiltonian operator in the enlarge space (augmented space) spanned by the basis $\{|\nu\rangle \otimes |\uparrow_R\rangle\}$

$\rangle \}$. Using this Hamiltonian we perform the recursion process in the augmented space and calculate the configuration averaged Green's function as single element of the Green's function in this enlarge space.

2.6.5 Self Consistency between TB-LMTO and ASR

In this section we shall describe a fully self consistent scheme to perform first principle electronic structure calculation for the disordered alloy by using TB-LMTO and ASR. The whole scheme is divided into two parts. First we determine the structure constant matrices \bar{S} for a given system. The canonical structure matrices are calculated in the same way as the LMTO-ASA does, that is expanding the tail of the envelop function at site R around the other site R' , which are nothing but the expansion coefficient of that expansion. From this canonical structure matrices S^0 we obtain the structure matrices for the tight-binding representation using the same mixing parameter α by which LMTO-ASA reduces to its most localized representation via the transformation $\bar{S} = S^0(I - \bar{\alpha}S^0)^{-1}$. The values of $\bar{\alpha}$ were found to be independent of structure and are given for s , p , and d electrons by $\bar{\alpha}_s = 0.3485$, $\bar{\alpha}_p = 0.05303$ and $\bar{\alpha}_d = 0.00107$. Since structure matrices depends only on the position of the atom and not the type of the atom, it does not change in the total self consistency process. Now to construct the Hamiltonian we need potential parameters \bar{C}_l , $\bar{\Delta}_l$ in the most localized basis of the LMTO. These are obtained from the orthogonal potential parameters C_l , Δ_l , α_l via the relation

$$\frac{\bar{C}_l - E_l}{C_l - E_l} = \frac{\bar{\Delta}_l}{\Delta_l} = 1 - (\alpha_l - \bar{\alpha}_l) \frac{C_l - E_l}{\Delta_l} \quad (2.60)$$

C_l , Δ_l , α_l are obtain by solving Schrödinger equation inside the Wigner-Sitz sphere for each type of atom. This part is called the atomic part and we treat this part of the problem in the same way as k -space LMTO-ASA formalism does. That is we use the same exchange and correlation term as one uses in LMTO-ASA formalism. The potential and the corresponding potential parameters inside the Wigner-Sitz sphere can be uniquely determined from the given occupation numbers of each local band, first and second order moment of the density of states relative to E_ν and the logarithmic derivative of the orbital wave function at the sphere boundary. The spherical averaged charge density inside a WS sphere can be expressed

in terms of the radial part of the Schrödinger equation inside the sphere and the moments of the local density of states. We choose the potential to be zero at the sphere boundary and corrected the total energy and potential by adding Madelung term while constructing the Hamiltonian. Starting from a guess charge density we made the local density potential and $\phi_\nu(r)$, $\cdot\phi_\nu(r)$ are calculated to the given logarithmic derivative. Then we construct a new charge density by occupying the wave functions according to the moments and iterate this process until the self consistency is achieved in the atomic sphere. E_ν is chosen to be such that the first moment of the density of state for the occupied part of the band is always zero. To start the self-consistency process, we give reasonable guess for the occupation, second moment and logarithmic derivatives and find nearly orthogonal potential parameters for each type of atom from the atomic part. then using eqn. (2.60) we calculate \bar{C}_l , $\bar{\Delta}_l$. Using \bar{C}_l , $\bar{\Delta}_l$ and the structure matrix \bar{S} we construct the augmented space Hamiltonian in the same procedure discussed in the previous section. Now we solve the eigen value problem of the disordered Hamiltonian by using recursion technique in the augmented space and obtain the local density of state(LDOS) for each type of atom and for each orbital. From LDOS we calculate new E_ν , moments for each band of each type of atom. The logarithmic derivatives are calculated from the E_ν and old potential parameters. Finally we supply all these moment an logarithmic derivative in the atomic part for the calculation of new potential parameter which will be used in the next iteration. We iterate this process until desire self-consistent values of moment and the logarithmic derivative achieved.

2.6.6 Problem of charge transfer, Madelung potential and energy

Since the constituent atoms in an alloy are different, there should be charge transfer between them in the alloying process and the neutral atomic spheres are become charged. As a result there Madelung energy become a significant part of the total energy. But in this case Madelung potential is very difficult to define as it depends upon the far environment in a given configuration.

In a single site CPA Johnson et all [Johnson et al., 1986] assumed that all atom of the same kind have the same net charge Q_A or Q_B which does not affected by the environment.

As a result

$$Q_i = n_R Q_A + (1 - n_R) Q_B$$

which follows on account for overall charge neutrality that

$$\langle Q_R Q_{R'} \rangle = \langle Q_R \rangle \langle Q_{R'} \rangle = 0$$

and hence $E_{mad} = 0$. This assumption works in many cases but for systems like *CuZn* alloy where the charge-transfer plays a significant role, it produces qualitatively incorrect results. For a mean-field coherent potential approach, Kudrnovský and Drchal [Kudrnovský and Drchal, 1990] have suggested using different atomic radii for the constituents in such a way that average total volume is conserved and the overlap is below the threshold value (15%), one can make these spheres approximately neutral and therefore ignore the Madelung contributions. In this procedure varying the ratio of the atomic spheres $r = R_A/R_B$ is very cumbersome, also Ruban and Skriver [Ruban and Skriver, 2002] have shown that local environmental effects (beyond the CPA) destroys the strict charge-potential alignment, and hence the possibility of choosing electroneutral atomic spheres by a single ratio r . In our self consistency process we have chosen the procedure namely screened impurity model proposed by Ruban and Skriver [Ruban and Skriver, 2002]. According to their suggestion the net charge of the alloy component embedded in the effective CPA medium is completely screened by the first shell of its surrounding effective atoms and the screening charge is uniformly distributed among all the Z_1 nearest neighbor atoms. The Madelung potential of the impurity atom is

$$V_M^i = -e^2 \frac{Q_i}{R_1}$$

where, $i = A$ or B (labels the constituents of the alloy), Q_i is the net charge of the alloy component i in its own atomic sphere of radius R_a and R_1 is the radius of the first coordination shell. Consequently the Madelung energy is given by :

$$E_{Madelung}^i = -\beta^* e^2 \frac{Q_i^2}{R_1} \tag{2.61}$$

where

$$\beta^* = 1 - \sum_{m=1}^4 \frac{n_m}{2Q_m}$$

with ϱ_m is the ratio of the radius of the m-th and 1-st coordination shell. In case of BCC and FCC structure the values of β^* are 0.69155 and 0.65735 respectively.

2.6.7 Termination Scheme

The continued fraction eqn. (2.53) is terminated via several schemes once $\{\alpha_n, \beta_n\}$ is converged. Convergence is necessary to represent the densities of state and Van Hove singularities of the exact Hamiltonian.

For single band of states, it was found that the $\{\alpha_n, \beta_n\}$ rapidly convergent to some (α, β) . So for $n \geq N$ we can set $\alpha_n = \alpha$ and $\beta_n = \beta$. We can sum up the remainder of the continued fraction analytically as:

$$\begin{aligned} T(E) &= \frac{\beta_n^2}{E - \alpha_n - \frac{\beta_{n+1}^2}{E - \alpha_{n+1} - \dots}} \simeq \frac{\beta^2}{E - \alpha - \frac{\beta^2}{E - \alpha - \dots}} \\ &= \frac{\beta^2}{E - \alpha - T(E)} \end{aligned} \tag{2.62}$$

$$\Rightarrow T(E) = \frac{1}{2} \left(E - \alpha - \sqrt{(E - \alpha)^2 - 4\beta^2} \right) \tag{2.63}$$

$T(E)$ is called the quadratic terminator and was proposed by Haydock [Haydock et al., 1972]. In more complex systems involving a number of isolated bands (For example, semiconductors and transition metal compounds), the quadratic terminator was found to be unsuitable and the quadrature method proposed by Nex [Nex, 1978] was found to be more useful. It has been found that given the band-edges and the truncated continued fraction, the analytic terminator proposed by Haydock and Nex [Haydock and Nex, 1984] and later improved by Luchini and Nex [Luchini and Nex, 1987] as compared to the quadrature method. Here is the outline of the analytic terminator schemes for a solid with a single band. A set of coefficients $\{\alpha_n, \beta_n\}$ is first generated recursively from the three term recurrence relation. We generate such coefficients up to $n = n_2$ steps. We now generate orthogonal polynomials of the first and second kinds: $P_n(z)$ and $Q_n(z)$ for the above recurrence relation. These are the solutions of:

$$\left. \begin{aligned} P_{n+1}(z) &= (z - \alpha_n) P_n(z) - \beta_n^2 P_{n-1}(z) \\ Q_n(z) &= (z - \alpha_n) Q_{n-1}(z) - \beta_n^2 Q_{n-2}(z) \end{aligned} \right\} \tag{2.64}$$

with $P_{-1}=Q_{-1}=0$, $P_0=Q_0=1$

We then locate, from the generated continued fraction coefficients ($n < n_2$), the lower (left) band edge a , the bandwidth r and the weight w . From this we construct a model Herglotz function with square-root band edge singularities:

$$F(z) = 8w \left[z - (a + r/2) - \sqrt{(z - a)(z - a - r)} \right] / r^2 \quad (2.65)$$

We now run the recursion again with the Hamiltonian replaced by z , the state vectors by polynomials described by equation (2-21), the inner product by a union of Gauss-Chebyshev quadrature:

$$f(z) \odot g(z) = \sum_{i=1}^n \Omega_i f(\alpha'_i) g(\alpha'_i) \quad (2.66)$$

where,

$$\begin{aligned} \Omega_i &= \frac{\pi w}{(n+1) \sin^2 \theta_i} \\ \alpha'_i &= a + (1 - \cos \theta_i) r/2 \\ \theta_i &= \frac{i\pi}{n+1} \end{aligned}$$

This generates a set of recursion coefficients $\{c_n, d_n\}$ and a set of mutually orthogonal polynomials $\{R_n(z)\}$ and $\{S_n(z)\}$. The terminator is then given by,

$$T(z) = \frac{S_{n-2}(z) - F(z) R_{n-1}(z)}{d_{n-1}^2 (S_{n-3}(z) - F(z) R_{n-2}(z))} \quad (2.67)$$

Again, from the fact that R_n and S_n are polynomials of order n and $F(z)$ is a Herglotz function, it follows immediately that the terminator is itself Herglotz. The Green function is given by,

$$G(z) = \frac{Q_{n-2}(z) - \beta_{n-1}^2 T(z) Q_{n-3}}{P_{n-1}(z) - \beta_{n-1}^2 T(z) P_{n-2}} \quad (2.68)$$

Using very similar arguments as before, the Green function is Herglotz if $T(z)$ is Herglotz.

It is easy to understand that in a chain with constant parameters if one appends a constant terminator with infinite band-width then the spectrum will consist of delta functions. When the band edge mismatch is reduced, these delta-functions broaden into Lorentzians and finally

only show up as oscillations superimposed on the semi-elliptic local density of states resulting from such constant coefficients. The parameters α_n and β_n represent the potentials on the one-dimensional chain and one can regard the eigenstates of the computed chain as being initially unable to tunnel out through the potential barrier of the terminator. As the height of the barrier is reduced, they become resonances superposed on the local density of states. The situation is analogous to the coherent reflection of the eigenstates by the step function in the potential represented by the discontinuous join to the terminator. The method of Luchini and Nex suggests linear interpolation between the computed and the analytic terminator coefficients to reduce the spurious oscillations arising out of this coherent reflection. The method is analogous to splicing as opposed to butt-joining pieces of wood.

We start with computed continued fraction coefficients α_n, β_n up to n_2 levels and with terminator coefficients α_n^t and β_n^t . The method of Luchini and Nex now suggests to linearly interpolate between the computed coefficients and that of the analytic terminator in the following manner:

$$\alpha_n = \begin{cases} \alpha_n & n \leq n_1 \\ [\alpha_n (n_2 - n) + \alpha_n^t (n - n_1)] / (n_2 - n_1) & n_1 \leq n \leq n_2 \\ \alpha_n^t & n_2 < n \end{cases}$$

where n_1 is the start and n_2 is the end of the interpolation. Similarly β_n can be obtained by replacing α_n with β_n in the above expression. Again, such a termination procedure retains the Herglotz properties of the Green function.

2.7 Effective Pair Interaction

In order to understand the onset of ordering in random alloys, one needs a derivation of the lowest configurational energy for a specified alloy system. Models have been set up describing configurational energies in terms of effective multi-site interactions, in particular EPE [Gonis et al., 1987]. Within this approach, the analysis of alloy ordering tendencies and phase stability reduces to accurate and reliable determinations of these EPE. Traditionally there have been two different approaches for obtaining the EPE. The first approach is to start

with the electronic structure and total energy determinations of ordered super-structures of the alloy and to use these to invert the relationship between total energies and EPE to obtain the latter. This is the Connolly-Williams method [Connolly, 1983]. The alternative approach is to start with the disordered phase, setup a perturbation in the form of concentration fluctuations associated with an ordered phase and study whether the alloy can sustain such a perturbation. This approach includes the Generalized Perturbation Method (GPM) [Ducastelle, 1976], the embedded cluster method (ECM) [Gonis et al., 1987] and the concentration wave approach [14]. We shall follow this alternative viewpoint. In this discussion, we will consider two different approach of this alternative method

- i. GPM method
- ii. orbital peeling introduced by Burke [Burke, 1976]

2.7.1 Generalized Perturbation Method

In a homogeneously disordered alloy A_xB_{1-x} with each site occupied by either A or B proportional to there concentration. We define occupation variable $n_{\mathbf{R}}$ which randomly takes value 0 or 1 if the site \mathbf{R} is occupied by A or by B with $\ll n_{\mathbf{R}} \gg = x$ The total internal energy of a particular configuration is

$$E = V^{(0)} + \sum_{\mathbf{R}} V_{\mathbf{R}}^{(1)} \delta n_{\mathbf{R}} + \sum_{\mathbf{R}} \sum_{\mathbf{R}' \neq \mathbf{R}} V_{\mathbf{R}\mathbf{R}'}^{(2)} \delta n_{\mathbf{R}} \delta n_{\mathbf{R}'} \quad (2.69)$$

with $\delta n_{\mathbf{R}} = n_{\mathbf{R}} - x$ and $\ll \delta n_{\mathbf{R}} \gg = 0$. If the configuration is homogeneously disordered then it immediately follows that $\ll E \gg = E_{dis} = V^{(0)}$. From the above definition we can interpret the other two expansion terms as follows: if E^I is the configuration averaged total energy of a configuration in which any arbitrary site labeled \mathbf{R} is occupied by an atom of the type I and the other sites are randomly occupied, and E^{IJ} is the averaged total energy of another configuration in which the sites \mathbf{R} and \mathbf{R}' are occupied by atoms of the types I and J , respectively, and all other sites are randomly occupied, then from 2.69 we see:

$$V_{\mathbf{R}}^{(1)} = E^A - E^B, V_{\mathbf{R}\mathbf{R}'}^{(2)} = E^{AA} + E^{BB} - E^{AB} - E^{BA} \quad (2.70)$$

The single site energy $V_{\mathbf{R}}^{(1)}$ corresponds to inhomogeneous disorder and $V_{\mathbf{R}\mathbf{R}'}^{(2)}$, the pair interaction energy gives the ordering energy.

While this method is very fast and computationally less demanding, it has a major drawback in the mode of calculating $V^{(2)}$: the terms E^{ij} 's are very large and comparable in magnitude. Hence, their difference is very small; leading to a numerical instability due to the fact that the difference goes smaller than the error involved in the measurement of E^{ij} . This problem is overcome using the Orbital Peeling method discussed below (§2.7.2).

2.7.2 Orbital Peeling

Orbital peeling technique, first introduced by Einstein and Schrieffer [Einstein and Schrieffer, 1973] was generalized by N. R. Burke [Burke, 1976] to take very small energy difference into account. We want to calculate the energy difference between two systems: 1) when the adatoms are far apart (Figure 2.7(a)) and 2) when the adatoms are close enough (Figure 2.7(b)). The interaction energy is calculated through density of states, which we define as

$$f(E_k) = \frac{1}{2\pi i} \oint_{\mathcal{C}} f(E) \text{Tr}[E - H]^{-1} dE \quad (2.71)$$

where \mathcal{C} is the contour of integration enclosing all poles below E_F

So, we calculate the one-electron eigenvalue (E_i) and the total energy will be given as

$$U_{TOT} = \sum E_i - U_{es}$$

for states below fermi level, E_F and U_{es} is the electrostatic interaction (inter-electronic and inter-ions). The required energy difference is given by

$$\Delta U_{TOT} = \Delta \left(\sum E_i \right) - \Delta U_{es} \quad (2.72)$$

If we rewrite in terms of “resolvent operator” using $\int_{-\infty}^{E_f} = \frac{1}{\pi i} \oint$ then, we have a complex N defined as

$$N = \text{Tr}[EI - H]^{-1} \quad (2.73)$$

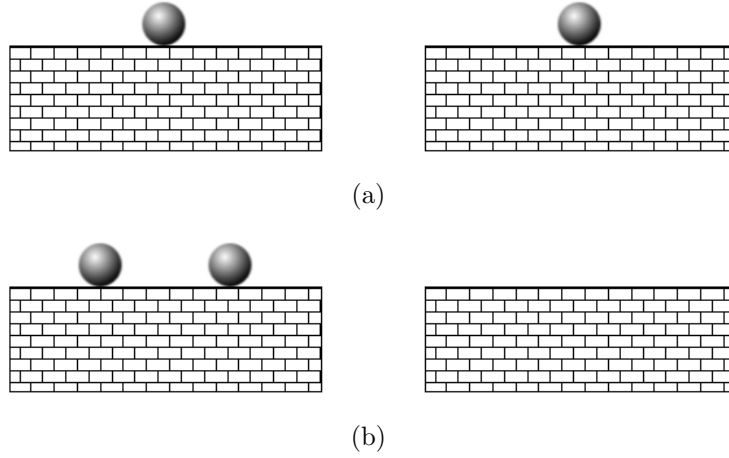


Figure 2.7: Interaction between adatoms. (a) when adatoms are far away and (b) when adatoms are close.

We get the electronic contribution to the structural energy as when the electrons are far apart is

$$U_1 = \int_{-\infty}^{E_F^{(1)}} EN_1(E)dE \quad (2.74)$$

and when the electrons come together, we have a new DOS, (N_2) and the new energy is given by

$$U_2 = \int_{-\infty}^{E_F^{(2)}} EN_2(E)dE \quad (2.75)$$

given $\int_{-\infty}^{E_F^{(2)}} N_2(E)dE = \int_{-\infty}^{E_F^{(1)}} N_1(E)dE$ the interaction energy is given by:

$$\begin{aligned} W &= U_2 - U_1 \\ &= \int_{-\infty}^{E_F} (E - E_F)\Delta N dE \end{aligned} \quad (2.76)$$

where $\Delta N = N_2 - N_1$. Now, we notice that when the systems are far apart as in Figure 2.7(a), each block has 1 atom, when they are close, as in Figure 2.7(b) one block has 2 atom when the other has none. Hence we can define

$$\begin{aligned} N_1 &= 2\text{Tr}[EI - H_1]^{-1} \\ N_2 &= \text{Tr}[EI - H_2]^{-1} + \text{Tr}[EI - H_0]^{-1} \end{aligned} \quad (2.77)$$

Following the identity from [Einstein and Schrieffer, 1973]

$$\text{Tr}[EI - H]^{-1} = \frac{\partial}{\partial E} \log \det[EI - H] \quad (2.78)$$

which yields

$$\Delta N = \frac{\partial}{\partial E} \log \frac{\det[EI - H_2] \det[EI - H_0]}{\det[EI - H_1] \det[EI - H_1]} \quad (2.79)$$

The structure of the Hamiltonian is given by

$$H_2 = \begin{pmatrix} E_A & V_{12} & \cdots & \tilde{V}_2 \\ V_{21} & E_A & \cdots & \tilde{V}_1 \\ \vdots & \vdots & \ddots & \vdots \\ V_2 & V_1 & \cdots & H_0 \end{pmatrix} \quad H_1 = \begin{pmatrix} E_A & \cdots & \tilde{V}_1 \\ \vdots & \vdots & \vdots \\ V_1 & \cdots & H_0 \end{pmatrix} \quad (2.80)$$

The dimension of the matrix depends on the orbital. As for d orbital, H_2 is an matrix of $(5N + 10)$ as first 5 rows are for 1st adatom, next 5 rows are for 2nd ad atom and $5N$ rows for H_0 , the substrate. Similarly, rank of H_1 is $5N + 5$. Evidently, $V_{12} = V_{21}$ as they are the interaction between each other ; V_1 and V_2 are interaction with substrate.

From eqn. (2.80), we see that $[EI - H_1]$ is a submatrix of $[EI - H_2]$ and $[EI - H_0]$ is a submatrix of $[EI - H_1]$, we have

$$\begin{aligned} \det[EI - H_2] &= \det \mathcal{G}_2^{-1} \det[EI - H_1] \\ \det[EI - H_1] &= \det \mathcal{G}_1^{-1} \det[EI - H_0] \end{aligned} \quad (2.81)$$

where

$$(\mathcal{G})_{\alpha\beta} = \langle a_i, \alpha | [EI - H_i]^{-1} | a_i, \beta \rangle \quad (2.82)$$

Substituting above results in eqn.(2.79), we get

$$\Delta N = \frac{\partial}{\partial E} \log \frac{\det \mathcal{G}_1}{\det \mathcal{G}_2} \quad (2.83)$$

which is the *working* equation of *orbital peeling technique*.

The physical meaning of this equation is quite clear: “ $\log \det \mathcal{G}_2$ ” is the energy to pull one of the two isolated adatom of system (Figure 2.7(a)) and “ $\log \det \mathcal{G}_1$ ” gives the energy to put it in a isolated place as in (Figure 2.7(b)).

2.8 Frozen Spin Phase

A good percentage of my work is based on frozen spin phase, popularly known as spin glass phase. The theory of Spin glass was first systematically documented in seminal paper of Edward and Anderson [Edwards and Anderson, 1975] showing that this phase is essentially due to the competitive interaction between ferro and antiferromagnetic ordering given by the Hamiltonian

$$\mathcal{H}_g = - \sum_{\langle i,j \rangle} J_{ij} \sigma_i \sigma_j - h \sum_i \sigma_i \quad (2.84)$$

Two distinctive features of this phase are

frustration The Hamiltonian (2.84) exhibits frustration: no spin configuration can simultaneously satisfy all couplings. If a closed circuit \mathcal{C} in the edge lattice satisfies the property

$$\prod_{\langle i,j \rangle \in \mathcal{C}} J_{ij} < 0 \quad (2.85)$$

then the spins along it cannot all be simultaneously satisfied [Toulouse, 1977] as shown in Figure 2.8. Anderson suggested a different formulation, namely that frustration manifests itself as free energy fluctuations scaling as the square root of the surface area of a typical sample. Either way, the spin glass is characterized by both quenched disorder and frustration. Their joint presence indicates the possibility that spin glasses might possess multiple pure thermodynamic states unrelated by any simple symmetry transformation.

ageing Below the glass temperature T_g , the dynamic response to a small magnetic excitation is slow, and in addition it depends on the time spent below T_g , and this phenomena is called aging. Numerically this is measured via the zero filled time dependent susceptibility (χ), where a characteristic inflection point in χ vs. $\ln t$ plot shows the existence of glassy phase.

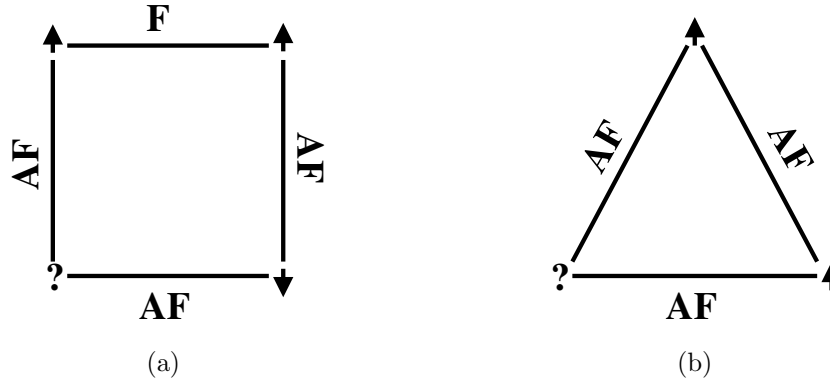


Figure 2.8: A simple frustrated contour in a 2D lattice. Bonds marked “F” correspond to ferromagnetic couplings ($J_{ij} > 0$) and “AF” corresponds to an antiferromagnetic coupling ($J_{ij} < 0$). Two possible arrangement of spins at the corner sites is shown.

2.8.1 Freezing of spin

Wohlfarth [Wohlfarth, 1977] showed the freezing of spin is closely related to blocking of superparamagnetic(SP) single domain magnetic particle in rock materials(RM). In RM, there are 10^5 or more particle coupled ferromagnetically in each domain. At high temperature, the interaction in paramagnetic and each particle posses giant magnetic moment. There are extra energy due to anisotropy: either due to shape, crystalline or external stress. Since no domain movement is possible, as in 1.4 on page 7. In 1949, Néel [Néel, 1949] show the Brownian motion in magnetization direction in these SP.

For uniaxial systems, magnetization relaxes as

$$M_r = M_0 e^{-t/\tau} \quad (2.86)$$

where M_0 is the full magnetization when the field is switched off and relaxation time τ is given by

$$\frac{1}{\tau} = \frac{1}{\tau_0} e^{-KV/K_B T}. \quad (2.87)$$

Here, τ_0 ($\approx 10^{-9}$ sec) arises due to random thermal fluctuation, K is anisotropy constant and V is the volume of the particle. V effects the typical relaxation time τ_m heavily. Like for

spherical Fe with radius 115 Å have relaxation time $\frac{1}{10}$ sec; where under same conditions, a particle of 150 Å will have relaxation time 10^9 sec [Chowdhury, 1983]. Usually a relaxation time 10^2 sec is considered as criterion of stability and the corresponding barrier height is $\approx 25k_B T$. The corresponding temperature is “blocking temperature”.

Wohlfarth [1977] draw analogy between blocking of superparamagnetic clusters and spin glass “freezing”. The single domain particles of SP clusters are, according to this analogy, is equivalent to non-interacting clusters of spin glasses. The formation of these non-interacting clusters at $T \gg T_g$ is evident from the experimental deviation of $\chi(T)$ from Currie-Weiss behavior [Cannella and Mydosh, 1972].

2.8.2 Atomistic spin dynamics: Relaxing spins ²

Autocorrelation function is a measure of relaxation of individual spins. Above T_g , though total magnetic moment of the system preserves, each spin changes its direction with time. The autocorrelation function, defined as

$$\mathcal{C}(t, t_w) = \langle \mathbf{m}_i(t_w) \cdot \mathbf{m}_i(t + t_w) \rangle \quad (2.88)$$

where t_w is the waiting time, i.e. time offset between initial and final measurement; shows how fast it “relaxes”. Since above T_g , individual spins are in dynamic motion, the average tends to 0 in normal magnetic phases; whereas in spin glass phase, it shows a continuous slow down in \mathcal{C} with t and equilibrates near 1, the initial value.

Phenomenological solution of spin relaxation, given by Landau and Lifshitz [Landau and Lifshitz, 1935] is

$$\frac{\partial \mathbf{m}}{\partial t} = -\gamma \mathbf{m} \times \mathbf{B} - \frac{\lambda}{m} \mathbf{m} \times (\mathbf{m} \times \mathbf{B}) \quad (2.89)$$

where γ is gyromagnetic ratio and λ the damping constant. Gilbert extend this equation introducing damping analogous to frictional force [Gilbert, 2004]

$$\frac{\partial \mathbf{m}}{\partial t} = -\gamma \mathbf{m} \times \mathbf{B} + \frac{\alpha}{m} \mathbf{m} \times \frac{\partial \mathbf{m}}{\partial t} \quad (2.90)$$

²This section is based on [Hellsvik, 2010]

2.8.3 ASD at finite temperature: Langevin Dynamics

To study the glassy phase we must include finite temperature effect as well into LLG equation (2.90). In this situation, beside \mathbf{B}_i and damping force, a stochastic torque will also act on atom's magnetic moment, which can be seen as fluctuating field \mathbf{b}_i . The fluctuation-dissipation theorem [Kubo, 1966] shows fluctuation and damping are initially connected.

In this direction, first work is done by Brown [Brown, 1963]. He calculated Fokker-Plank equation for stochastic LLG equation and couples α and \mathbf{b}_i to temperature T . In this derivation, both precessional and damping motion was affected by the stochastic torque. Kubo and Hashitsume [Kubo and Hashitsume, 1970] left damping unaffected by \mathbf{b}_i . Brown and Kubo *et al* derived their model for single domain magnetic particles and for single spins. Antropov *et al* [Antropov, 2005] showed both formalism can be applicable to atomic magnetic moment as well.

Kubo's formalism yields LL equation in the presence of stochastic field(SLL)

$$\frac{d\mathbf{m}_i}{dt} = -\gamma\mathbf{m}_i \times [\mathbf{B}_i + \mathbf{b}_i(t)] - \gamma\frac{\alpha}{m}\mathbf{m}_i \times \{\mathbf{m}_i \times [\mathbf{B}_i + \mathbf{b}_i(t)]\} \quad (2.91)$$

which is basically Langevin equation [van Kampen, 2007] with \mathbf{b}_i , a multiplicative noise term, introduced as Langevin force.

To solve eqn. (2.91) we assume components of $\mathbf{b}_{i,\mu}$ where $\mu = x, y, z$ are uncorrelated and also independent of \mathbf{m}_i . We extend ordinary differential equation(ODE) solvers to solve this stochastic differential equation(SDE). Two solver, based on Runge-Kutta scheme, is used. One in Euler and other is Heun's. In both cases, time is discretized $t_0 < t_1 < t_2 < \dots < t_n$ and also the solutions $x_0 < x_1 < x_2 < \dots < x_n$. The stochastic extension of Euler's scheme is

$$x_i(t + \tau) = x_i(t) + A_i(\{x\}, t)\tau + \sum_k B_{ik}(\{y\}, t)dW_k \quad (2.92)$$

where τ is the finite increment and dW_k is the increment that replaces stochastic variable Γ_j defined as $dW_j = \int_0^\tau \Gamma_j dt$.

Chapter 3

Electronic structure calculation in random alloys

This chapter is based on

Rudra Banerjee and Abhijit Mookerjee. Augmented Space Recursion Code and Application in Simple Binary Metallic Alloy. *International Journal of Modern Physics C*, 21(02):205, 2010.

The predictions of properties of classical and new materials such as substitutional disordered alloys, their surfaces and metallic or semiconducting multilayers have great importance. A detailed understanding based on the microscopic, parameter free approach is necessary for future development in material science. In a solid the outer most electrons of the atoms play an important role, as they bind each atom to its neighbor and determines the properties of the resulting materials. So one of the important aim of the condensed matter theory is the calculation of the electronic structure of solids. This is not only helpful in understanding and interpreting experiment, but also a predictive tool of the condensed matter and materials science. In case of disordered systems the calculation of such properties are much more difficult compared to that of the ordered system. Difficulties arises due to the involvement of the random variables and we have to carry out averages for physical observables over different configurations. In §2 we have discussed various methods used in this thesis

and particularly the TB-LMTO-ASR method for calculation of the electronic structure of disordered alloys. In this chapter we shall first overview some of the conventional mean field theories for the configuration averaging. We shall also discuss their limitations and probable extensions. Finally we shall discuss a fully self-consistent scheme of TB-LMTO-ASR calculation for realistic systems.

3.1 Dealing with disorder: Different levels of approximation

3.1.1 The Rigid Band Model and The Virtual Crystal Approximation

The first attempt at the calculation of the electronic structure of disordered alloys was made by Jones in 1934 with his rigid band model (RBM). In this crude approximation we neglect the potential differences between alloy constituents: the electronic state of pure A metal is identical to that of pure B and even A_xB_{1-x} alloy. The only composition-dependence comes from number of electrons per atom of A and B [Stern, 1967]. The average number of electron per atom $n = N_A C_A + N_B C_B$, where $N_{A/B}$ is number of electron and $C_{A/B}$ is the concentration of A/B determines Fermi energy and other properties [Grimvall, 1972].

Clearly, this method is only applicable when the difference in potential of A and B is very small, and that too in limited cases. This is an oversimplified model which neglects the difference between alloy constituents and only accounts for the number of electrons per atom which is different for different alloys. In its time this model was a success for a very few cases like $CuNi$ system where potentials of constituents are nearly identical. Almost all types of alloy the eigen value distribution is qualitatively very different from that of the constituents materials and the model does not work.

Korringa in 1958 modified RBM to the Virtual Crystal Approximation (VCA). He assumed that the potential associated with every lattice site in the alloy is same and which is

equal to the concentration average potential $\langle V \rangle$ of the constituents.

$$V_{alloy} = \langle V \rangle = xV_A + (1 - x)V_B$$

where x is the concentration of one constituent. For systems with weak scattering potential and consisting of nearly equal concentration of the constituents, this model is fairly successful. In this model the self energy consisting of only the lowest order term $\langle V \rangle$, which is independent of wave-vector k . Therefore the life-time of the states are infinite as in the pure materials. Only due to the scattering of the impurities, alloys states are decay with finite lifetime. Assuming V is very small, we get

$$\langle V_i V_j \cdots V_n \rangle \cong \langle V_i \rangle \langle V_j \rangle \cdots \langle V_n \rangle$$

and the Green's function becomes

$$\langle \mathcal{G}(E) \rangle = P(E) [1 - \langle V \rangle P(E)]^{-1} = [E - H_0 - \langle V \rangle]^{-1}$$

i.e. the pure crystal's Green's function with a $\langle V \rangle$ shift.

Despite some success, this approximation is mathematically wrong. Firstly, the self-energy, $\Sigma_{VCA} = \langle V \rangle$ is real, independent of energy and wavevector \mathbf{k} . So, the lifetime of the \mathbf{k} -state is infinite, as in pure metal, and not in alloys. Also Rayleigh-Schrödinger perturbation theory shows, VCA can not give correct density of states. This is because of the fact that, eigenvalue distribution of alloys are fundamentally different from pure elements and one can not go to another by any finite number of perturbation steps [Gonis, 1992; Dargam et al., 1997].

3.1.2 Average t-matrix approximation (ATA)

VCA can not accurately describe systems with large difference between the potential of the constituents atoms. It also fails if there are large concentration fluctuations. In case of small concentration one deals with averaging the scattering matrix (t-matrix) associated with individual scatterers (potential) instead of using average potential. We can express the

Green's function in terms of the scattering matrix as:

$$G_1(r - r', t - t') = G_0(r - r', t - t') + \int_0^t dt_1 \int_0^{t_1} dt_2 \int dr_1 \int dr_2 G_0(r - r_1, t - t_1) T(r_1, r_2; t_1, t_2) G_0(r_2 - r', t_2 - t') \quad (3.1)$$

where G_0 is the unperturbed Green's function and

$$T = \sum_{i,j} T_{ij} \quad (3.2)$$

is the total system t-matrix with

$$\begin{aligned} T_{ij} &= V_i \delta_{ij} + V_i G_0 V_j (1 - \delta_{ij}) + \sum_k V_i G_0 V_k G_0 V_j + \dots \\ &= V_i \delta_{ij} + V_i \sum_k G_0 T_{kj} \end{aligned} \quad (3.3)$$

Separating $k = i$ term we can write

$$T_{ij} = t_i \delta_{ij} + t_i \sum_k G_0 T_{kj} \quad (3.4)$$

t_i are the single site scattering matrix and these are replaced by the average value $\langle t \rangle$. If we considering VCA medium as the host material, then perturbation is $V_i - \langle V \rangle$ and correspondingly $\langle t \rangle$ becomes

$$\langle t \rangle^{ATA} = \frac{x(\epsilon_A - \langle \epsilon \rangle)}{1 - (\epsilon_A - \langle \epsilon \rangle) G_0^{VCA}} + \frac{(1-x)(\epsilon_B - \langle \epsilon \rangle)}{1 - (\epsilon_B - \langle \epsilon \rangle) G_0^{VCA}} \quad (3.5)$$

with $\langle \epsilon \rangle = x\epsilon_A + (1-x)\epsilon_B$. The configuration averaged Green's function is given by

$$\langle G \rangle = G_0 + G_0 [\langle t \rangle^{ATA} (1 - G_0 \langle t \rangle^{ATA})^{-1}] G_0$$

Compare to VCA, ATA shows the impurity bands and k -states with finite life times [Soven, 1967].

3.1.3 Coherent Potential Approximation

As we have mentioned before that for the disordered system the main thrust goes to obtain the configuration averaged quantity. Also the Green's function contains all informations about the system. Therefor the main aim goes to the calculation of configuration averaged Green's function for a disordered system. In this context Soven [Soven, 1967] and Taylor [Soven, 1967] in 1967 introduce independently the widely used approximation namely Coherent potential approximation (CPA). In case of totally random alloy their basic idea was to obtain a translationally symmetric effective Hamiltonian (H^{eff}) and the representation of it's Green's function G^{eff} which are good approximation of the average Green's function of the random Hamiltonian. If we write the total Hamiltonian as $H = H_0 + V$ where $V = \sum_i V_i$ is the superposition of the real individual site potential $V_i(z)$ then in terms of self energy operator $\Sigma(z)$ one can write the average Green's function as:

$$\langle G(z) \rangle = \langle (z - H)^{-1} \rangle = [z - H_0 - \Sigma(z)]^{-1} \quad (3.6)$$

Now in a translationally invariant medium $\Sigma(z)$ the total Hamiltonian can be written as

$$H(z) = H^{eff}(z) + V(z) - W(z) \quad \text{with} \quad H^{eff}(z) = H_0(z) + W(z)$$

where $W(z) = \sum_i W_i(z)$ is the translationally invariant site-dependent quantities $W_i(z)$. Defining $\mathcal{V}(z) = \sum_i (V_i - W_i)$ and $G^{eff}(z) = (z - H^{eff})^{-1}$ we can express the resolvent $G(z)$ and corresponding T operator $T(z)$ as :

$$\begin{aligned} G(z) &= G^{eff}[1 - \mathcal{V}(z)G^{eff}] \\ T(z) &= \mathcal{V}(z) + \mathcal{V}(z)G^{eff}\mathcal{V}(z) \\ G(z) &= G^{eff} + G^{eff}T(z)G^{eff} \end{aligned}$$

Clearly G^{eff} is translationally symmetric and therefore the average $G(z)$ becomes

$$\begin{aligned} \langle G(z) \rangle &= G^{eff}(z) + G^{eff}(z)\langle T(z) \rangle G^{eff}(z) \\ &= [1 + G^{eff}(z)\langle T(z) \rangle]G^{eff}(z) \end{aligned} \quad (3.7)$$

and hence to get the average Green's $\langle G(z) \rangle$ function as the effective Green's function $G^{eff}(z)$ i.e.

$$\langle G(z) \rangle = G^{eff}(z) \quad (3.8)$$

We need to satisfy

$$\langle T(z) \rangle = 0 \quad (3.9)$$

The self energy becomes

$$\begin{aligned} \Sigma(z) &= z - H_0(z) - [\langle G(z) \rangle]^{-1} \\ &= z - H_0(z) - G^{eff}(z)^{-1} \{1 - G^{eff}(z) \langle T(z) \rangle [1 + G^{eff}(z) \langle T(z) \rangle]^{-1}\} \\ &= z - H_0(z) - G^{eff}(z)^{-1} + \langle T(z) \rangle [1 + G^{eff}(z) \langle T(z) \rangle]^{-1} \\ &= W(z) + \langle T(z) \rangle [1 + G^{eff}(z) \langle T(z) \rangle]^{-1} = W(z) + \Sigma_1(z) \end{aligned}$$

With the help of eqn. (3.4) in the previous section we can write

$$\langle T(z) \rangle = \sum_i \langle Q_i(z) \rangle \quad (3.10)$$

where $\langle Q_i \rangle$ can be represents as

$$\begin{aligned} \langle Q_i \rangle &= \langle t_i(z) \rangle \left[1 + G^{eff}(z) \sum_{i \neq j} \langle Q_j(z) \rangle \right] \\ &+ \langle [t_i(z) - \langle t_i(z) \rangle] G^{eff}(z) \sum_{i \neq j} [Q_j(z) - \langle Q_j(z) \rangle] \rangle \end{aligned}$$

The first term of the above expression contains only the single site quantities but the second one is kind of correlation term. In CPA The second term is neglected and therefore it is single site approximation. But neglecting second term means that, excluding the local environmental effect like short-ranged ordering. So in CPA $\langle Q_i(z) \rangle$ becomes

$$\langle Q_i(z) \rangle = \langle t_i \rangle \left[1 + G^{eff}(z) \sum_{j \neq i} \langle Q_j(z) \rangle \right] \quad (3.11)$$

So in the single site coherent potential approximation condition in eqn. (3.9) namely $\langle T(z) \rangle = 0$ reduces to

$$\langle Q_i(z) \rangle = 0 \implies \langle t_i(z) \rangle = 0 \quad \forall i \quad (3.12)$$

This condition implies that the average scattering produces on a site is zero. It is possible to prove that this approximation preserves the analytic properties of the Green's function

and gives first eight moment of the density of state exactly. It is also reproduces several limiting cases like dilute limit where concentration of one of the constituent is goes to zero and it is exact up to first order. In the atomic limit it can be shown that the approximation is exact up to the second order term by using the locator formalism. Using the CPA concept Gyorffy [Gyorffy et al., 1985] apply it subsequently within the KKR method. Stocks and Winter [Stocks and Winter, 1982] performed first charge-self-consistency calculation of KKR-CPA. Kudrnovský [Kudrnovský et al., 1990] applied the CPA concept withing the TB-LMTO method.

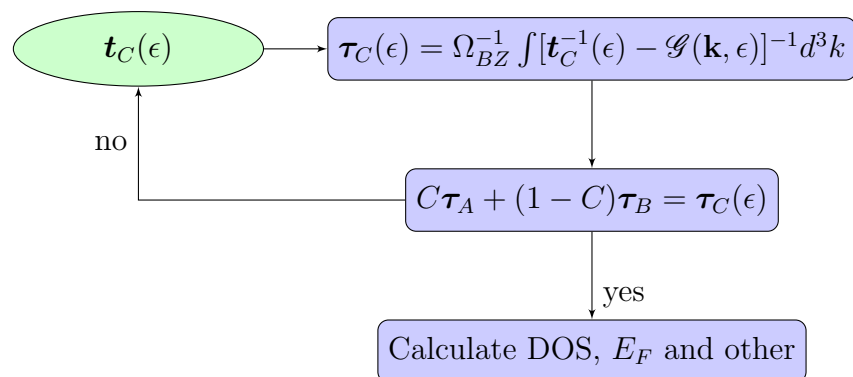


Figure 3.1: Simple flowchart for CPA.

CPA is very robust both from mathematical and physical point of view. It is able to explain several one-electron properties of the system for considerable range. It is the *best* single-site approximation available, without any doubt. But, it still posses some very serious drawbacks. This originate from the requirements assigned to the Hamiltonian, types of randomness and in the approximation in Green's function itself [Yonezawa and Morigaki, 1973]. This theory fails when there exist cluster effect, or short-range ordering or off-diagonal randomness.

3.1.4 Beyond single site CPA

Although CPA produces excellent results in many cases and no doubt it is a very good approximation and is widely used but it has several limitations. As we have discussed before

that being single site approximation, CPA cannot take into account the local environmental effects and off-diagonal randomness. It also fails to describe local lattice distortions. In case of low dimensionality for example surfaces it cannot be able to produce fine structures in the density of states. There have been several attempts by many authors to generalize this approximation to overcome those limitations. These are basically the cluster generalization of the CPA. Generalizing scattering t -matrix approach Nickel and Krummhanl (1971) and Leath [Leath, 1970, 1972] tried to include all cross scattering diagrams involving two sites. This diagram summation is extremely cumbersome and intractable for a bigger cluster. After partitioning the system into subunits, Tsukada [Tsukada, 1972] suggested to carry out CPA by replacing single site by such subunits. This is the easiest way to include some of the effects of scattering from cluster of atoms. This procedure is called the molecular coherent potential approximation (MCPA). However in case of homogeneous disorder this violates the lattice translational symmetry of the configuration averaged Green's function. Butler [Butler, 1972, 1973] suggested a further approximation to overcome this difficulty. He assumed that every cluster has a central site and the CPA equations are applied only to the central site. In the weak scattering limit the 'central site approximation' produces good results. However in the strong scattering limit the density of state becomes many-valued and negative in some energy range and the sum rule for the integrated density of state is violated. After that he applied the CPA equations in the boundary sites instead of central site which also gave unphysical results in the strong scattering limits. The traveling cluster approximation (TCA) proposed by Kaplan and Gray [Kaplan and Gray, 1976] using augmented space formalism discussed in §2.6, is a major breakthrough in this direction. This method based on the fact that instead of summing all possible diagrams necessary for consistent treatment of scattering event one should sum up certain type of diagrams so that the corresponding self energy satisfies the condition : $Im(\Sigma(z)) \leq 0$ for $Im(z) \geq 0$, which is necessary (but not sufficient) for analyticity. The TCA formalism provides a consistent rule for summing such class of diagrams so that the self energy and Green's function with proper analytic properties can be obtained. Also the diagrammatic consistency generates all higher order graphs associated with a given type of scattering and includes such scattering throughout the material. In the two site version, this method not only retains the analytic properties of the Green's function but also

the lattice translational symmetry of the configuration averaged Green's function, however this method is also suffers some limitations. The method is computationally extremely difficult for a bigger cluster size and is nearly impossible to implement for a realistic system.

3.2 ScASR: The configuration averaged method

The DFT Self-consistent ASR package was developed to handle first-principles studies of electronic structure of systems without long-ranged lattice translational symmetry. Bulk disordered alloys and surfaces and interfaces which are either flat, corrugated or rough fall under this category which our formalism should be able to take care of. Lack of lattice translational symmetry means that the standard reciprocal space techniques based on the powerful Bloch theorem can no longer be of any use and we have to depend on alternative techniques based purely on real space approaches. Our formalism will be a marriage of three distinct methods which have been individually applied extensively : namely, the recursion method (RM) of Haydock [Haydock et al., 1972, 1975], the augmented space method proposed by Mookerjee [Mookerjee, 2003; Chakrabarti and Mookerjee, 2005] and the tight-binding, linear muffin-tin orbitals method (TB-LMTO) [Andersen and Kasowski, 1971]. The last mentioned provides us with a DFT self-consistent sparse representation of the Hamiltonian in a real-space minimal basis $\{|\mathbf{R}_n L\rangle\} \in \mathcal{H}$. Here \mathbf{R}_n labels the sites where the ion-cores sit and $L = (\ell m \sigma)$ are the angular momentum indices. For a disordered system the matrix elements of the Hamiltonian representation in this basis are random. This representation is then taken over by the ASR to generate a modified Hamiltonian representation in the outer product space of \mathcal{H} and the space \mathcal{C} of configuration fluctuations of the random parameters. This modified Hamiltonian represents a collection of all possible Hamiltonians for all possible configurations of Hamiltonian representations. Once this is done the RM allows us to obtain the matrix elements of the Green functions related to the Kohn-Sham equation for the electronic states. The augmented space theorem (AST) [Mookerjee, 1973] relates a specific matrix element of the Green function in the augmented space $\mathcal{H} \otimes \mathcal{C}$ to the configuration averaged Green functions. The RM is a purely real-space based technique, and therefore as applicable to a bulk system as one with surfaces, interfaces or extended defects. In the

following we shall describe each of the points raised above in some detail.

As this is the main tool of my work, the algorithm is detailed in the following section.

3.2.1 The ScASR Algorithm

The full ScASR package is divided into several sub-packages. The first sub-package is the Preparation Module. The routines are those of the LMTO47 Stuttgart code [Andersen, 75] mostly edited in its file structure and variable names to accommodate them themselves as variables. The Module has two branches, one each for each constituent of the alloy. Each branch is parallelly run on two different slave processors, with the results collected in a master processor. The structure matrix is calculated in the master processor. These routines in this

lminit This prepares the control files for the different alloy constituents,

lmhart This carries out a simple Hartree calculation and prepares the atomic sphere radii of the constituents,

Module are : *lmovl* Checks the overlap between the atomic spheres,

lmes Sets up the “empty spheres” carrying charge but no ion-cores to fill up the excess interstitial space in open lattices,

lmstr Calculates the structure matrix in the screened representation.

The Preparation Module is followed by the main ASR-module. This module is called by the routine *lmasr*. This main module is divided into five smaller modules :

Module A This module reads the data generated by the Preparation Module. It checks the inputs for consistency. The routines in this module are again those in the Stuttgart LMTO47, but modified to read the inputs for *both* the two constituents of the alloy.

Module B At the start of the DFT self-consistency loop, this module takes the overlap of a simple Hartree atomic density calculation in the Preparation module and generates the Hartree and exchange-correlation potentials, spheridizes them and inputs them to the Atomic Module that follows. In later steps of the self-consistency loop, this Module first mixes the charge densities of the earlier steps and prepares the Hartree and exchange-correlation potentials, spheridizes them for input into the Atomic Module.

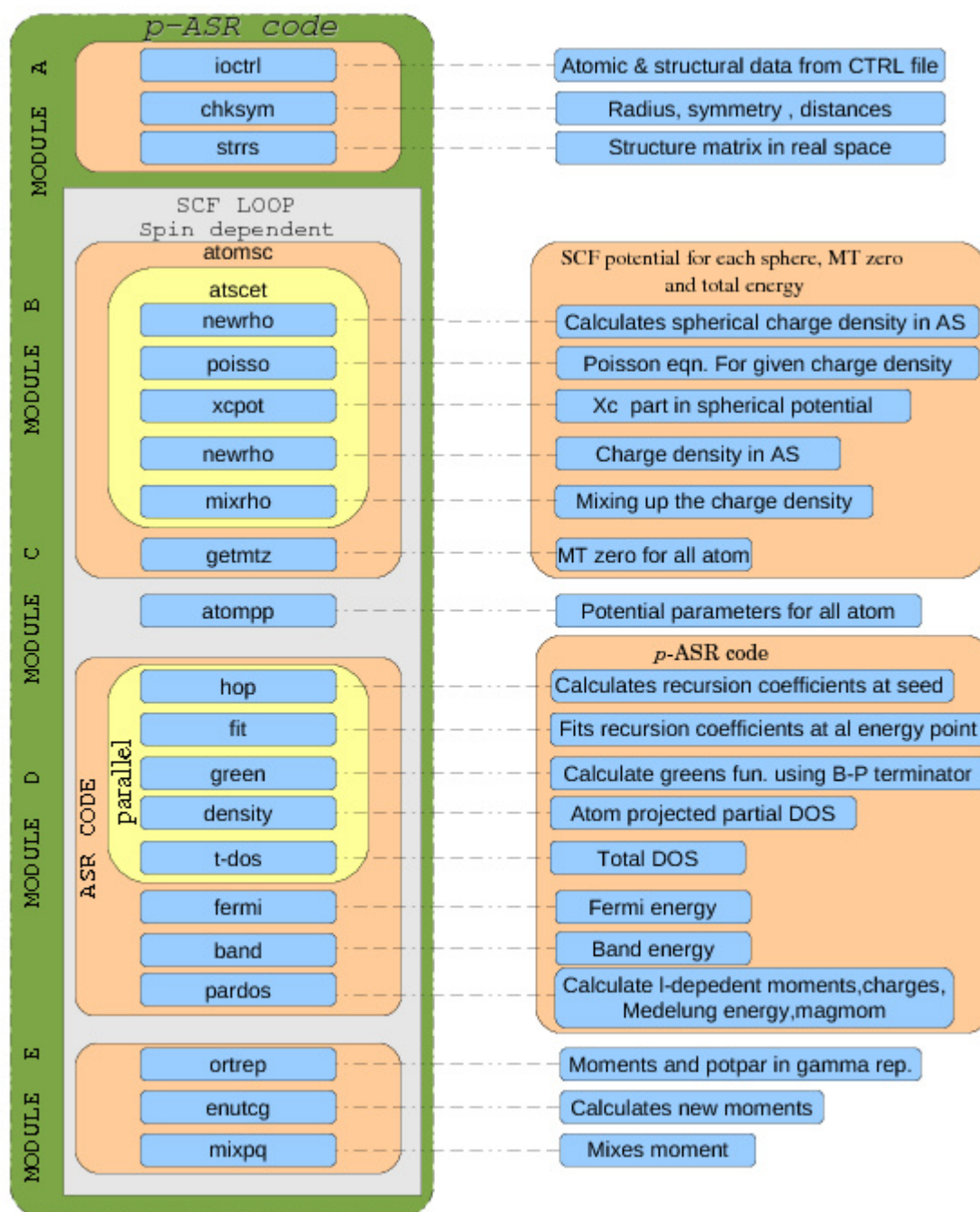


Figure 3.2: The TB-LMTO-Augmented Space Recursion package flowchart

- At this point there is a choice of using either the standard DFT exchange-correlation potentials or, alternatively, there is a branch module *Harbola-Sahni* which sets up the Harbola-Sahni potential for the study of excited states [Rahaman et al., 2009].

Module C This is the Atomic Module. It takes the spheridized Kohn-Sham potential generated in Module B and solves the radial Kohn-Sham equation numerically. The Kohn-Sham orbitals and energies then lead to the potential parameters for each constituent. Those for the two constituents are calculated on different processors. The parameters are first calculated in the orthogonal representation. A new routine *gtoa*, not present in the Stuttgart LMTO47 package, then transforms them to the most screened tight-binding representation.

Module D This is the main ASR Module. The routines herein have been fully developed by us and form the main backbone of the package. The input are the tight-binding Hamiltonian parameters from the Atomic Module. First they are combined with the alloy composition to prepare the augmented space Hamiltonian. The nearest neighbour map in augmented space is then generated. Next, the recursion is carried out for each L value, terminators generated and the L projected density of states are calculated. Each different recursion for each L value is carried out on a different processor, thus vastly accelerating the calculations.

We then proceed to calculate the total density of states and the Fermi energy. Again, branching out into different processors, we calculate the L -dependent moments and magnetic moments. Of all the Modules, this is the one amenable to maximum parallelization.

- (a) At this point we have the possibility of introducing short ranged order. The ASR for short-ranged order has been described in some detail earlier [Mookerjee and Prasad, 1993]. The branching for this choice occurs just before we set up the augmented space Hamiltonian. The extra input is the Warren-Cowley short ranged order parameter.

(b) Also at this point we have the option to introducing disorder in the structure matrix because of size mismatch between the two constituents of the alloy. The branching now takes place earlier in the Preparation Module where we generate not one, but three different structure matrices : $\underline{\underline{S}}_{ij}^{AA}$, $\underline{\underline{S}}_{ij}^{BB}$ and $\underline{\underline{S}}_{ij}^{AB}$. In the ‘end point’ approximation [Saha and Mookerjee, 1996] structure matrix is defined by:

$$\tilde{\mathbf{S}} = \sum_{ij} \left\{ \ll \underline{\underline{S}}_{ij} \gg \mathcal{I} + \underline{\underline{S}}_{ij}^{(1)} (\mathcal{N}_i + \mathcal{N}_j) + \underline{\underline{S}}_{ij}^{(2)} \mathcal{N}_i \otimes \mathcal{N}_j \right\} \otimes \mathcal{T}_{ij} \quad (3.13)$$

where $\mathcal{N}_i = (y - x)\mathcal{P}_{\downarrow i} + \sqrt{xy}\mathcal{T}_{\uparrow i \downarrow i}$, $\underline{\underline{S}}_{ij}^{(1)} = \underline{\underline{S}}_{ij}^{AB} - \underline{\underline{S}}_{ij}^{BB}$ and $\underline{\underline{S}}_{ij}^{(2)} = \underline{\underline{S}}_{ij}^{AA} + \underline{\underline{S}}_{ij}^{BB} - 2\underline{\underline{S}}_{ij}^{AB}$. This modification will be available in this module.

It is in these last two options that the ASR really scores over the CPA, which cannot really deal with either short-ranged order or off-diagonal disorder as both involve more than one site. The competing methodology is the special quasi-random structures (SQS) [Zunger et al., 1990]. However, if we are dealing with materials with many atoms per unit cell and non-stoichiometric compositions, the SQS required will be rather large and will involve use of *huge* unit cells. Here the TB-LMTO-ASR with the use of much smaller unit cells will score. We have shown earlier [Tarafder et al., 2008a] that both these two methods give virtually the same results for the density of states.

Module E In this module the L -dependent moments are used to obtain the charge density. We also calculate the total energy, including the Madelung term. For the disordered alloy, the Madelung term is obtained from the procedure suggested by Skriver and Ruban [Ruban and Skriver, 2002]. Finally the old and new moments are mixed, the mixed charge density thus obtained is input back in Module B. This is iterated till convergence in both energy and charge density is achieved.

For the DFT part, our code depends heavily on Stuttgart-LMTO routines developed by Anderson and co-workers [Andersen and Jepsen, 1984]. Two independent DFT codes run parallelly to produce the potential parameters of the two constituent atoms of the binary

% time	cumulative seconds	self seconds	calls	self s/call	total s/call	name
49.91	100.73	100.73	81	1.24	2.26	hop
40.78	183.04	82.31	1.6×10^9	0.00	0.00	matp
0.76	196.82	1.53	7	0.22	0.22	spectral
0.00	201.84	0.00	1.8×10^5	0.00	0.00	splint
0.00	201.84	0.00	206	0.00	0.00	spline
0.00	201.84	0.00	56	0.00	0.00	matmult
0.00	201.84	0.00	36	0.00	0.00	mom
0.00	201.84	0.00	28	0.00	6.59	doparallel
0.00	201.84	0.00	7	0.00	0.00	fit
0.00	201.84	0.00	4	0.00	0.00	tdos
0.00	201.84	0.00	1	0.00	0.00	band
0.00	201.84	0.00	1	0.00	0.00	fermi
0.00	201.84	0.00	1	0.00	0.00	pardos

Table 3.1: gprof data for the optimized and parallelized ASR code. The discontinuity between the cumulative time of `spectral` and `splint` is due to the machine routine which are not included here.

alloy. These potential parameters are used at the input point of our ASR routines in Module D.

Our present DFT modules deal only with collinear magnetism. For spin dependent calculations the Hamiltonian is separable in spin space. Thus the spin is merged with the label L which is now $\{\ell, m, \sigma\}$ and we have just to carry out twice the number of recursions : for $\sigma = \uparrow$ and \downarrow . In case we wish to introduce spin-orbit coupling and possibility of non-collinear magnetism, we have to replace the DFT module with one dealing with density matrices, rather than densities [Lizárraga et al., 2004] and the ASR module with one applying generalized or vector recursion [Godin and Haydock, 1988, 1991] which was designed to deal with Hamiltonians whose representation in spin-space or ‘spinor’ bases is not diagonal.

	Old TB-LMTO-ASR	AMscf
Wall time	699 sec	225 sec
Efficiency $\left(\frac{\text{cputime}}{\text{walltime}}\right)$	0.714	0.97

Table 3.2: Comparison between old code based of augmented space recursion and AMscf

To benchmark these characteristics we take a specific calculation on $\text{Fe}_x\text{Cr}_{1-x}$ and $\text{Cu}_x\text{Zn}_{1-x}$. Each calculation is done on a 73109 site augmented space map, with N recursion steps with $L = s, p_x, e_g$ and t_{2g} , and $\sigma = 1, 2$, followed by a Beer-Pettifor termination scheme. Gnu profiler output [Fenlason and Stallman, 2011] for the new TB-LMTO-ASR are given in the Table (3.1). Table 3.2 shows the compairison between an pre-existing augmented space recursion based code [Chakrabarti and Mookerjee, 2005] and AMscf. Here Wall time is the total run time and Efficiency is the ratio between the Wall time and CPU time.

Chapter 4

Applications of ScASR: Electronic Structure of some binary alloys

This chapter is based on

P.Singh, **R. Banerjee**, M. Rahaman, A.V. Ruban, B. Sanyal, and A. Mookerjee. Magnetic behaviour of AuFe and NiMo alloys. *Pramana*, 76:639, 2011.

Rudra Banerjee and Abhijit Mookerjee. Study of phase stability of MnCr using the augmented space recursion based orbital peeling technique. *Physica B: Condensed Matter*, 404(14-15):1979–1983, July 2009.

Rudra Banerjee and Abhijit Mookerjee. Augmented Space Recursion Code and Application in Simple Binary Metallic Alloy. *International Journal of Modern Physics C*, 21(02):205, 2010.

The code, as detailed in §2 and §3 is implemented in different binary and ternary alloys. But, before applications, we have tested the formalism on a few simple binary alloys. This chapter proceeds as follows:

In §4.1 we will discuss Electronic structure of two very different type of alloys where one shows split Density of states (DOS) and the other has overlapped DOS. The systems studied here are CuZn and FeCr.

In §4.2 we will discuss Electronic structure and ordering energy, effective pair interactions etc. of MnCr alloy.

In §4.3 we will discuss the Electronic structure and Effective Pair interaction (§2.7.2) of AuFe Alloy.

4.1 CuZn and FeCr alloy

The suitability of our method is based on how good it can reproduce various alloys giving rise to different type of DOS. In this section of, we have chosen two different types of alloy, among them one gives split DOS and other overlapped.

The Figure 4.1 shows DOS of CuZn and FeCr alloy for 3 concentrations each. The CuZn alloy shows split DOS where FeCr shows overlapped DOS. The alloys have been studied earlier by us using the old version of the TB-LMTO-ASR [Chakrabarti and Mookerjee, 2005; Saha et al., 1994, 1996] and TB-LMTO-CCPA¹ [Rahaman and Mookerjee, 2009] and the KKR-ICPA² [Ghosh et al., 2002] which is also based on the augmented space formalism, as well as through the KKR-CPA³ [Turchi et al., 1994], PAW-SQS⁴ [Zunger et al., 1990] and KKR-NL-CPA⁵ [Jarrell and Krishnamurthy, 2001; Rowlands et al., 2005]. They are therefore ideal system for bench marking the new TB-LMTO-ASR package. Comparison of the densities of states shown in Fig. 4.1 with the results shown in the above references will convince us that for $\text{Fe}_x\text{Cr}_{1-x}$ there is hardly anything to choose between the various techniques and the packages based on them. However, for the split band alloy $\text{Cu}_x\text{Zn}_{1-x}$

¹Tight-binding linear muffin-tin orbitals cluster coherent potential approximation

²Korringa-Kohn-Rostocker itinerant coherent potential approximation

³Korringa-Kohn-Rostocker coherent potential approximation

⁴Projector augmented wave special quasi-random structures

⁵Korringa-Kohn-Rostocker non-local coherent potential approximation

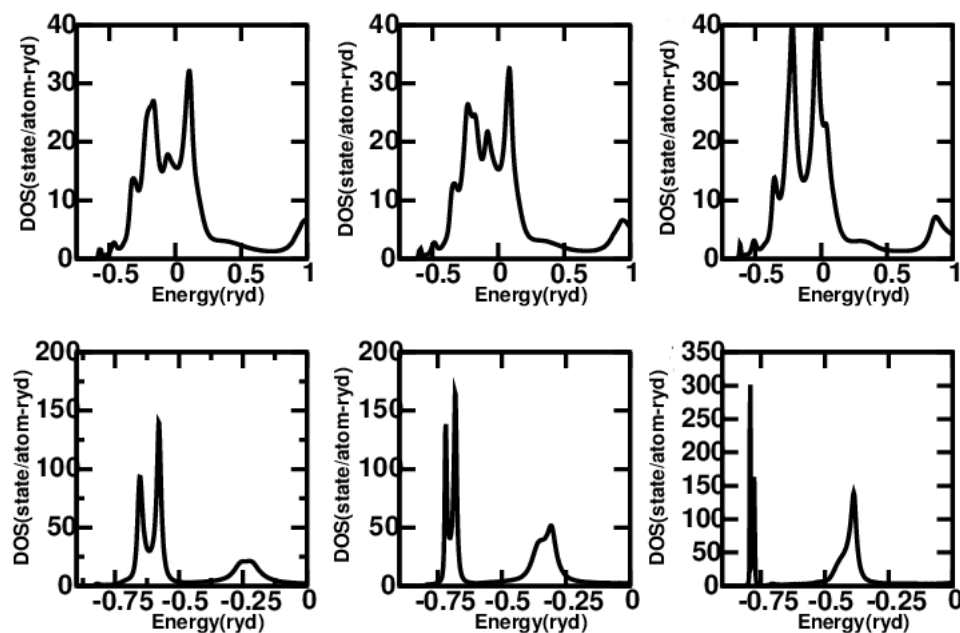


Figure 4.1: (Top) DOS for $\text{Cr}_x\text{Fe}_{1-x}$ for different compositions: (left) Cr_7Fe_3 ; (middle) Cr_5Fe_5 ; (right) Cr_3Fe_7 ; (Bottom) DOS for $\text{Cu}_x\text{Zn}_{1-x}$ for different compositions: (left) $\text{Cu}_{24}\text{Zn}_{76}$; (middle) $\text{Cu}_{50}\text{Zn}_{50}$; (right) $\text{Cu}_{75}\text{Zn}_{25}$. Energy(Ryd) is plotted along x -axis; y -axis is DOS (states/Ryd)

the TB-LMTO-ASR, TB-LMTO-CCPA and KKR-NL-CPA scores over the CPA versions, as expected from earlier analysis.

One of our our main point of interest is the relative runtime and efficiency of this new version of the TB-LMTO-ASR, as compared to the several earlier versions proposed by us (see Table 3.1 on page 68). To benchmark these characteristics we take a specific calculation on $\text{Fe}_x\text{Cr}_{1-x}$. Each calculation is done on a 73109 site augmented space map, with N recursion steps with $L = s, p_x, e_g$ and t_{2g} , and $\sigma = 1, 2$, followed by a Beer-Pettifor termination scheme.

4.2 MnCr alloys and their stability

We studied MnCr alloy to the study of phase stability and transition of binary alloys. We had combined the recursion method introduced by Haydock, Heine and Kelly [Haydock et al., 1972] and the our augmented space approach [Mookerjee, 1973] with the orbital peeling technique proposed by Burke (§2.7.2) to determine the small energy differences involved in the discussion of phase stability. We started our study of MnCr alloy with finding out the structure of MnCr.

4.2.1 Calculation of ordering energy

We will describe very briefly the methodology of ordering energy calculation here. Philhours and Hall [Philhours and Hall, 1967] have suggested, and Clapp and Moss [Clapp and Moss, 1966, 1968] have formally shown that a sufficient (but not necessary) condition for a stable ground state is that the wave vectors of concentration waves corresponding to an ordered phase lie in the positions of the minima of the Fourier transform of the pair energy function

$$V(\vec{k}) = \sum_{\vec{R}-\vec{R}'} \exp \left\{ i\vec{k} \cdot (\vec{R} - \vec{R}') \right\} V^{(2)}(\vec{R} - \vec{R}')$$

The above statement follows from the expression for the inverse susceptibility which measures the response of the disordered system to the concentration fluctuation perturbation described above.

$$\chi^{-1}(\vec{k}) \propto 1 + x(1-x)\beta V_{\text{eff}}(\vec{k})$$

In a zero-th approximation $V_{\text{eff}}(\vec{k}) = V(\vec{k})$. Corrections to the effective pair-function has been described in detail by Chepulskaa and Bugaev [Chepulskaa and Bugaev, 1998]. We have used here the Ring Approximation suggested by the authors as the one most suitable for our analysis :

$$V_{\text{eff}}(\vec{k}) = V(\vec{k}) - (\beta/2)(1-2x)^2 \int \frac{d^3\vec{q}}{8\pi^3} F(\vec{q})F(\vec{k}-\vec{q}) \quad (4.1)$$

where

$$F(\vec{q}) = \frac{V(\vec{q})}{1 + x(1-x)\beta V(\vec{q})}$$

Ordering and mixing energies Finally, the GPM expression also gives the ordering energy :

$$\Delta E_{ord} = \frac{1}{2} \sum_n V_{0n}^{(2)} Q_n$$

where n is a n -th nearest neighbor of an arbitrarily chosen site (which we label 0) and $Q_n = (x/2)(N_n^{BB} - xN_n)$, N_n^{BB} is the number of BB pairs and N_n the total number of pairs in the n -th nearest neighbor shell of 0.

With reference to the total energies of the pure constituents, in the approximation where we only restrict ourselves to pair energies and ignore all three body energies and higher, the so-called mixing energy is given by :

$$\Delta E_{mix} = -\frac{1}{2}x(1-x) \sum_n N_n V_{0n}^{(2)}$$

4.2.2 Analysis of Stability

We have calculated the composition dependent pair energy functions using the TB-LMTO-ASR coupled with the orbital peeling technique and the result for the equi-atomic composition is shown in Figure 4.2(b). The nearest neighbor pair energy function $f_1(\vec{R} - \vec{R}', E)$ shows the characteristic shape of a positive lobe, indicating ordering, near the position of half filling, flanked by negative lobes indicating segregation near empty and complete filling fractions.

We should note that in our approach, both the pair energy function itself and the position of the Fermi energy depend upon the composition of the alloy and its band filling. This is in contrast to some analysis (like the Connolly-Williams) which depend on similar, but composition independent, pair energy functions. The Figure 4.3(b) shows the pair energies $V^{(2)}(|\vec{R} - \vec{R}'|)$ for the equi-atomic composition. The behavior of the pair energies for MnCr indicate ordering tendencies up to the fourth nearest neighbors. The pair energies rapidly converge to zero with distance. In fact, although we had calculated the pair energies up to the seventh nearest neighbor shells, their values beyond the fourth shell were smaller than the error bars of our method and therefore these numbers were not really reliable and not used for our analysis. The same is true for the results of the ordering energies for seven different

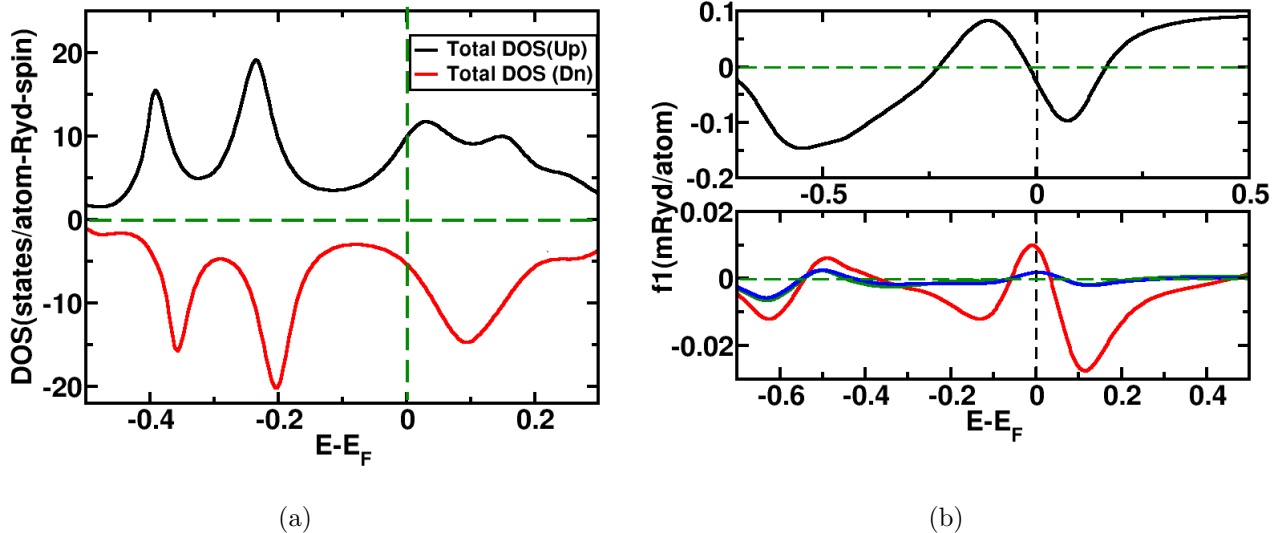


Figure 4.2: (a) Densities of states for a series of alloy compositions for 50-50 MnCr alloy.(b)Pair functions calculated for $Mn_{50}Cr_{50}$, variation shown against $E-E_F$, calculated from ScASR -OP. (top) Nearest neighbor pair function at a distance $\sqrt{3}a/2$, a being the equilibrium lattice parameter (bottom) second, third and fourth nearest neighbor pair functions at distances a , $\sqrt{2}a$ and $\sqrt{3}a$

structures and super-structures based on the body-centered cubic lattice. We have, therefore, calculated the ordering energies with contributions only up to the fourth neighboring shell. The Table 4.1 gives us the weights Q_n for the seven bcc based structures required to obtain the ordering energies in this alloy system. These superstructures are described in detail by Finel and Ducastelle [Finel and Ducastelle, 1984].

Based on the Table 4.1 we present the ordering energies for the same seven bcc based structures for MnCr in Figure 4.3(a).

The contrast between the two alloys FeCr [Tarafer et al., 2008a] and MnCr is interesting : Fe segregates with Cr while Mn orders. The stainless steel alloys, a class of which are ternary alloys FeCrMn should then see competition between segregation and ordering. We intend to study the ternary compositions subsequently.

Finally we shall examine the Fourier transform $V(\vec{k})$ of the pair energies and carry out a Clapp-Moss type of analysis. The contour diagrams for Fourier transform $V(\vec{k})$ is plotted

Structure	Neighboring shells			
	1	2	3	4
Segregated	1.00	0.75	1.50	3.00
B2	-1.00	0.75	1.50	-3.00
B32	0.00	-0.75	1.50	0.00
B11	0.00	0.25	-0.50	0.00
ST1	-0.50	0.25	0.00	0.50
ST2	0.00	-0.25	-0.50	0.00
ST3	0.50	0.25	-0.00	-0.50

Table 4.1: Weights for different neighboring shells for seven different bcc based equi-atomic superstructures.

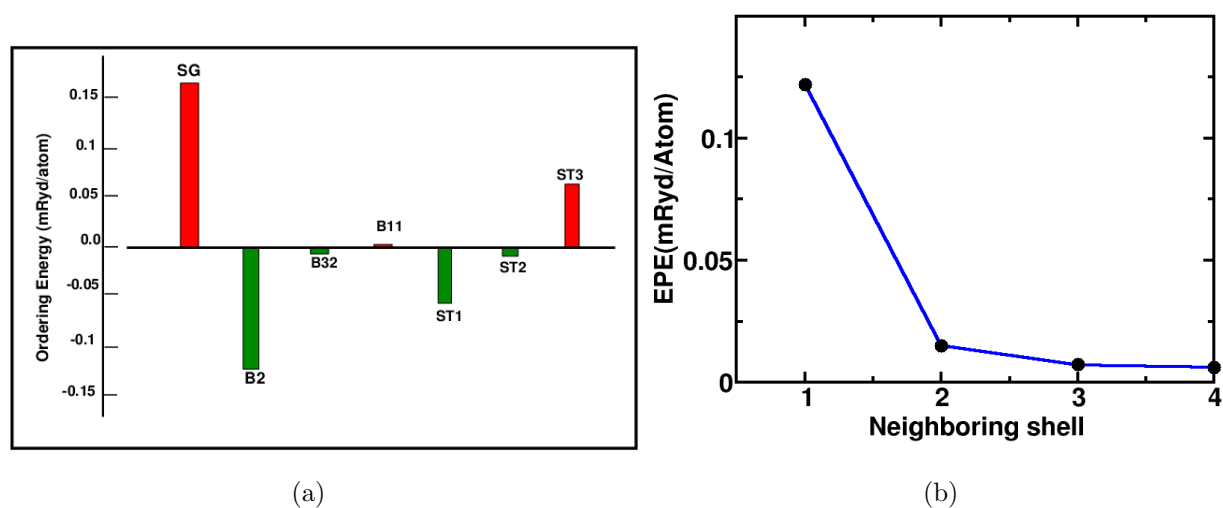


Figure 4.3: (a) Ordering energies for seven different structures based on 4.1 and (b) Pair energy for $\text{Mn}_{50}\text{Cr}_{50}$ alloy

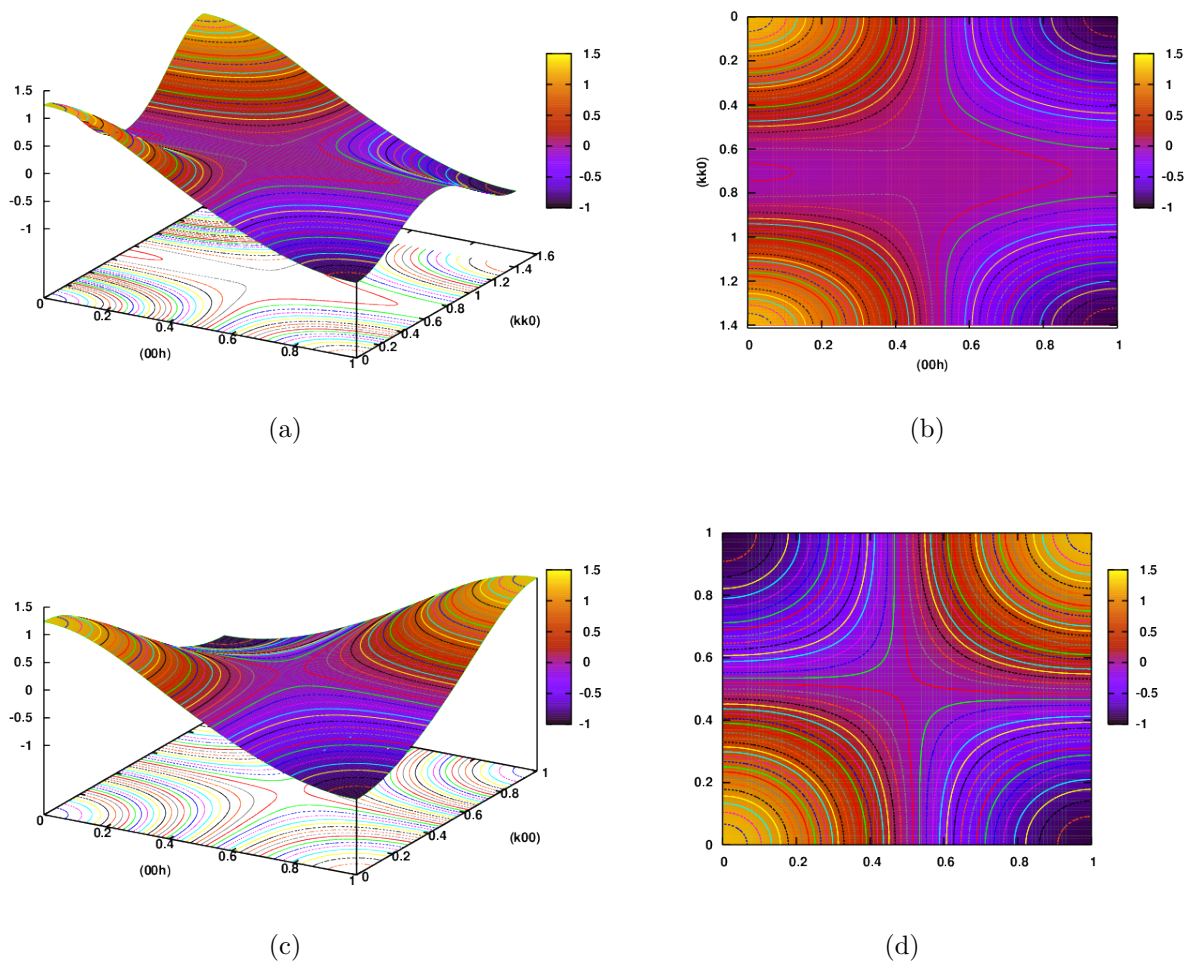


Figure 4.4: $V_{\text{eff}}(\vec{k})$ and contours on the plane bounded by (a) (001) (b) (100) (c)(001) (d)(110) of MnCr alloy

in Figure 4.4 for the (001) and ($1\bar{1}0$) planes. The minimum occurs at $\vec{k} = (001)$. This is indicative of a possible B2 type of ordering, as indicated by the ordering energy analysis.

In order to ascertain whether the ordered state associated with the minimum is stable compared to the segregated species, we have to carry out a much more detailed analysis including the contribution of the energy of mixing. The mixing energy for the B2 structure is 0.16412 mRyd/atom. This indicates that ordering is stable against segregation.

We should comment here that the above discussion is based only on the electronic contribution to the diffuse scattering intensity. At the temperatures that we are interested in there are contributions from the vibrational excitations in the system. Our aim here was to indicate the possibility of ordering tendencies in MnCr rather than accurate estimation of energetics and transition temperatures. In any detailed and accurate statistical mechanical calculations we must include the contribution of vibrational excitations to the free energy of the alloy.

4.2.3 Conclusion

K. Tarafder *et al.* [Tarafder et al., 2008b] had introduced and examined the suitability and accuracy of the Augmented Space Recursion (ASR) based Orbital Peeling (OP) method for the generation of pair energies. In this section we have extended these ideas into body-centered cubic MnCr alloy. We have looked at the phase stability of the equi-atomic alloy. Unlike FeCr, FePd and PtV alloys, for MnCr we had no earlier theoretical work to compare with. However, since the applications to FeCr, FePd and PtV gave satisfactory results, in good agreement with experimental evidence, we have confidence in our present results. With FeCr, this work will form the background of our extension of this work to ternary FeMnCr stainless steel alloys. The recursion and ASR is now available with both relativistic corrections (including spin-orbit terms) [Huda et al., 2004] and non-collinear magnetism [Bergman et al., 2008; Tarafder et al., 2008a]. Since earlier we have proposed the ASR as a analyticity preserving generalization of the single-site mean-field coherent potential approaches, this work will provide further incentive to extend the use of the ASR to problems beyond the simple density of states calculations and in problems where relativistic corrections and non-collinear magnetism will play significant roles.

4.3 Magnetic properties of AuFe alloy

4.3.1 Electronic structure of AuFe Alloy

The Figure 4.5 shows the atom and spin projected density of states for $\text{Au}_{1-x}\text{Fe}_x$ at two characteristic compositions $x = 0.04$ and $x = 0.10$. This is an example of an almost split-band alloy with the Au and Fe spectra hardly overlapping each other. It has been argued earlier that dilute split-band alloys are well described by the augmented space recursion technique used by us. We first note that the Au densities of states are negligibly exchange

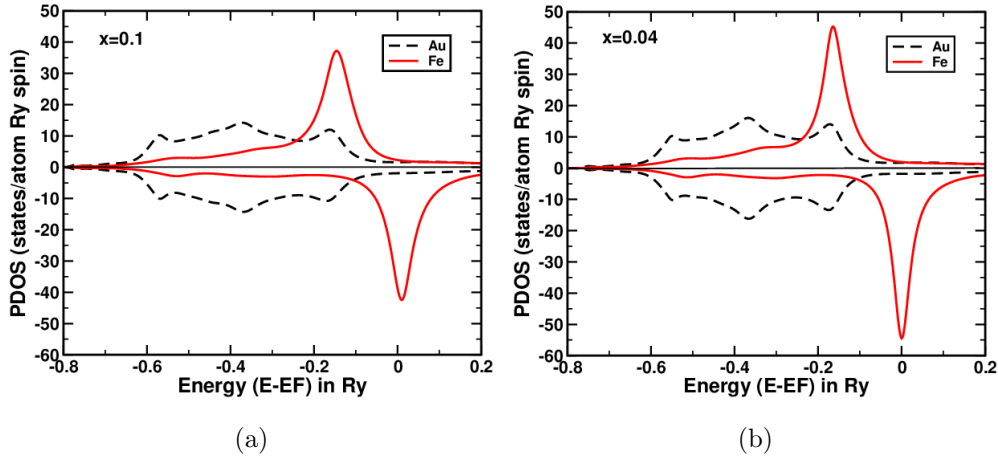


Figure 4.5: Projected densities of states for Au (black) and Fe (red) for $\text{Au}_{1-x}\text{Fe}_x$ alloys (a) $x=0.01$ (b) $x=0.40$

split. The Au atoms carry negligible magnetic moments at all compositions. The Fe density of state for the dilute Fe composition ($x = 0.04$) resembles a narrow impurity band for both the spin orientations. As the iron concentration increases the Fe PDOS becomes wider. The up-channel is almost fully occupied, while the down-channel is almost half full. This feature remains unchanged across the composition range.

4.3.2 Magnetic structure of AuFe Alloy

The Figure 4.6 shows the local magnetic moment on the Fe atom in the $\text{Au}_{1-x}\text{Fe}_x$ alloy in the same composition range. We should note two specific points:

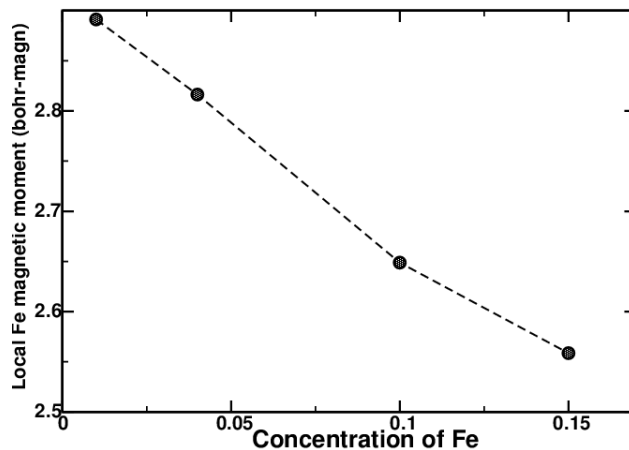


Figure 4.6: Local magnetic moment at a Fe site in $\text{Au}_{1-x}\text{Fe}_x$ as a function of Fe concentration x

- (i) even in the composition range $x \leq 0.1$ where the global magnetic moment is experimentally found to be zero, locally Fe atoms in the alloy have finite moments at low temperatures. The study of the local magnetic moment cannot distinguish the random ferromagnet from a spin glass phase.
- (ii) The local magnetic moment on Fe increases as its concentration decreases. This indicates that the magnetism on Fe is predominantly itinerant. We have noted that the projected density of states for Fe becomes narrower as its concentration decreases. The Stoner criterion says that its magnetic moment should increase. As $x \rightarrow 0$ this moment approaches that of an Fe atom.

Figure 4.7(a) shows the variation of $J(R) = E^{(2),\text{FeFe}}(R)$ with R for various compositions of the $\text{Au}_{1-x}\text{Fe}_x$ alloy. We may note two features of the pair energies :

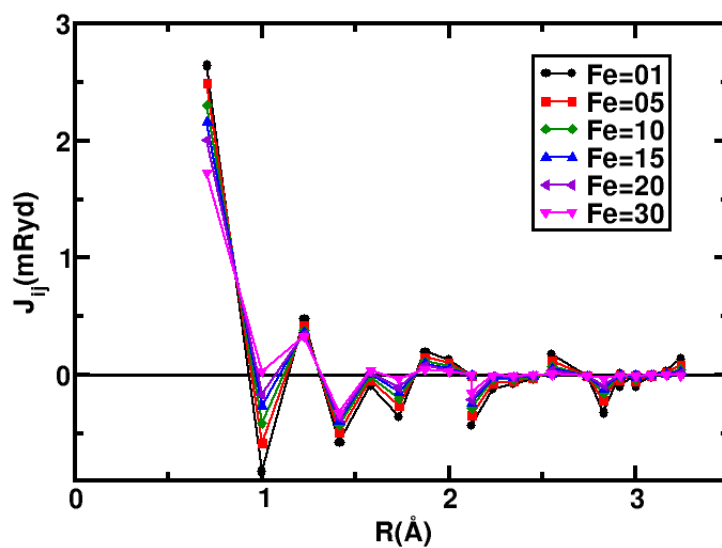
- (i) The pair energies are dependent on the composition. The simplified models without exception assumed that the pair energy depended only on the materials comprising the alloy. Figure 4.7(b) shows the composition dependence of $J_n = J(R_n)$ at various values of n-th neighbor distance R_n on the face-centered cubic lattice. Both J_1 and J_2 show strong dependence on the Fe concentration x . Several of the pair energies (markedly J_2) change their sign with increasing Fe concentration. This has to be incorporated in any realistic model of the spin glass.
- (ii) The pair energy $J(R)$ oscillates in sign with increasing R so that the possibility of frustration is present. The nearest neighbor pair energy is strongly ferromagnetic and quite a bit larger than the next nearest neighbor one. The behavior of the pair energies exhibits exponential decay characteristic of disorder damping. With increasing Fe concentration disorder scattering increases and so does the damping. A model with damped, oscillatory interaction seems suitable for these alloys.

Let us examine the behavior of $J(R)$ in greater detail. To quantify the variation of J_n with n we use the spatial moments of the scaled pair energy :

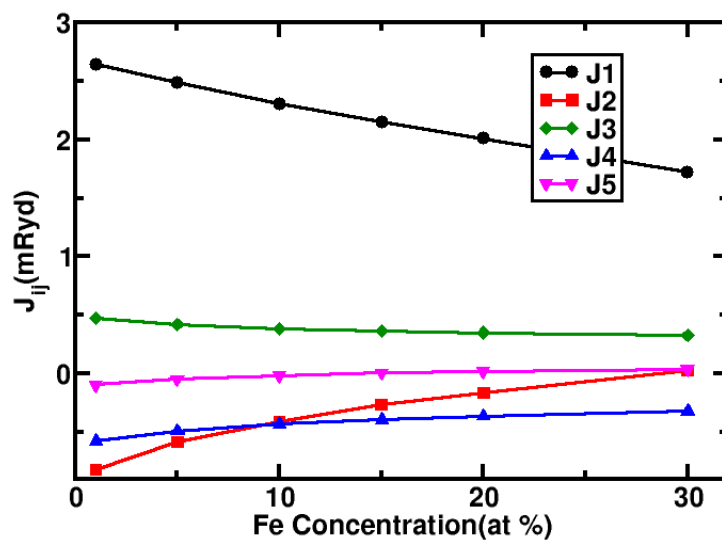
$$\begin{aligned}
 I_0 &= \sum_R W(R)J(R) \\
 I_{n-1} &= \sum_{R \geq a} W(R) \{J(R)/I_0\}^n \quad n = 2, 3 \dots
 \end{aligned}
 \tag{4.2}$$

$W(R)$ are the coordination numbers on the face-centered cubic lattice.

From Figure 4.8 we note that the third and fifth moments I_2 and I_4 are negative. This is characteristic of distribution which are asymmetric with more weightage towards negative or antiferromagnetic pair energies. This asymmetry decreases as the concentration of Fe increases and at around $x \simeq 0.16 - 0.18$ the moments become positive. The fourth moment I_3 goes to zero with increasing x indicating that the distribution becomes more Gaussian, while the second moment I_1 also decreases and the distribution about the mean becomes sharp delta function like. Can these results throw some light on the nature of frustration in the system and its behavior with x ? Khmelevskiy et.al.[Khmelevskiy et al., 2004] have used the partial moments $K(R_0) = \sum_{R > R_0} W(R)J(R)$ to illustrate frustration. We argue that



(a)



(b)

Figure 4.7: (a) The pair energy $J^{FeFe}(R)$ for AuFe alloys, across the composition range, as a function of $R = |\mathbf{R}_i - \mathbf{R}_j|$. (b) Variation of $J^{FeFe}(R)$ with composition.

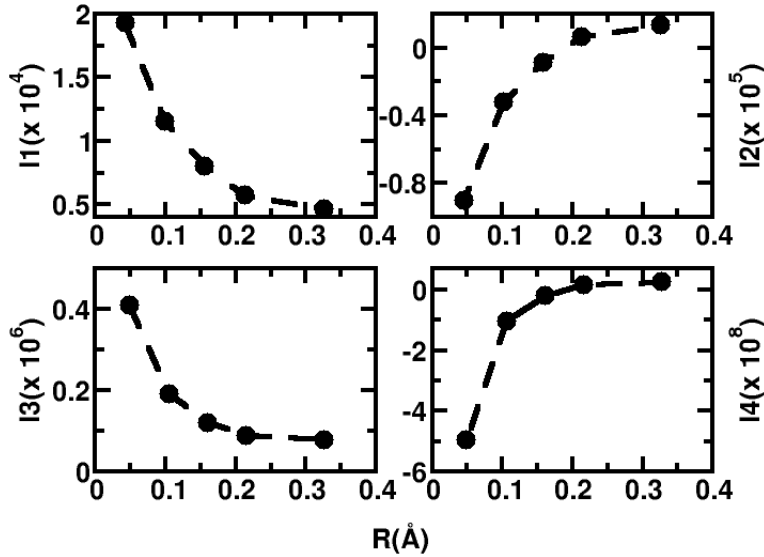


Figure 4.8: Moments of $J(R)$ for AuFe alloys (for $R \geq a$) and their variation with composition

the moments by themselves cannot give full information about frustration unless we couple them with the lattice topology. Predominance of antiferro-magnetic pair energies indicates the possibility of frustration. But antiferro-magnetic pair energies themselves may not lead to frustration until we couple it to frustrated plaquettes on the lattice. On bipartite lattices even completely antiferro-magnetic pair energies lead to no frustration at all.

Figure 4.9 shows the smallest triangular and quadrilateral plaquettes within a cubic unit cell of the face-centered cubic lattice. Only one example Figure 4.9(f) covers a triangular plaquette that spans two neighboring cells. The signs shown are that of the corresponding $J(R)$ for $x = 0.01$. All these plaquettes involve sides which are up to fifth nearest neighbors. Given the exponential decay of $J(R)$ with R , these smaller plaquettes are energetically the most important. The nearest neighbor plaquette (Figure 4.9(a)) is not frustrated, as all pair energies are ferro-magnetic. All the remaining triangular plaquettes (Figure 4.9(b)-4.9(f)) are frustrated. However, as $x \geq 0.16$ both the second and fifth nearest neighbor pair energies change sign and *all* these plaquettes lose their frustration. In the bottom row, the

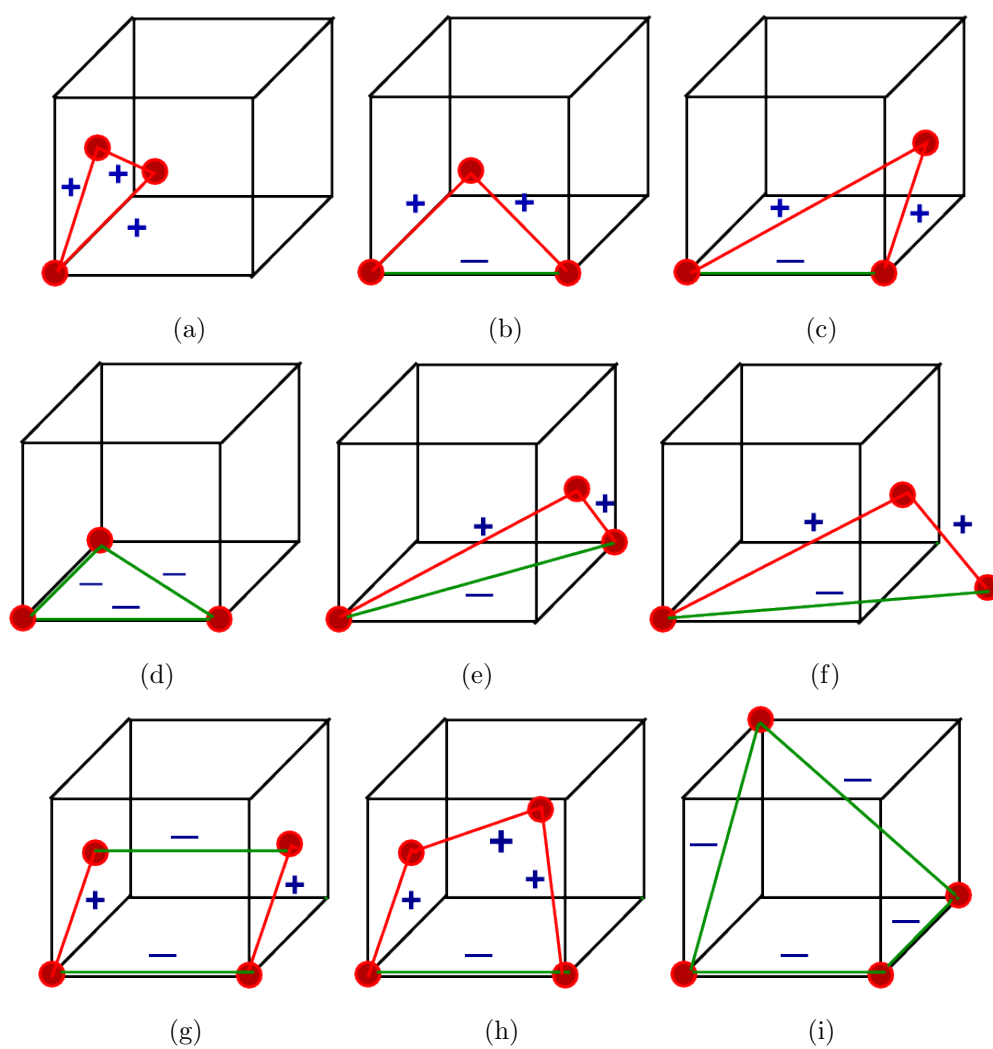


Figure 4.9: Plaquettes on the face-centered cubic lattice. Signs are those of the corresponding pair energies for $x = 0.01$

quadrilaterals (Figure 4.9(h)) and (Figure 4.9(i)) are also frustrated at $x = 0.01$ and lose their frustration as $x \geq 0.16$ and the second and the fifth nearest neighbor pair energies change sign. The table 4.2 shows the statistics of the plaquettes of various sizes and shapes within the cubic unit cell. As the concentration of Fe increases 78% of the triangular, and 90% of the polygonal plaquette which were frustrated earlier now lose their frustration.

Plaquette	(a)	(b)	(c)	(d)	(e)	(g)	(h)	(i)
Number	32	24	24	24	48	12	72	48

Table 4.2: Number of different triangular, quadrilateral and pentagonal plaquettes in a cubic unit cell

It is clear from the examination of the smaller plaquettes on a face-centered cubic lattice that the degree of frustration, as measured by the number of frustrated plaquettes, decreases considerably as x increases. Since frustration is central to the understanding of the spin-glass, the decrease of the degree of frustration with increasing x could be understood as the cause of the spin-glass to random ferro-magnet transition with composition at $T=0$. This could not have been understood without a microscopic derivation of the coupling. The physics of the interplay between chemical and magnetic ordering in AuFe has been described in some detail by Ling et.al.[Ling et al., 1995]. We have used the KKR-CPA type calculations to obtain the Ornstein-Zernicke direct correlation function from the electronic grand potential. We have not addressed the problem of chemical ordering and its effect on magnetic ordering. The Ising model which we have set up is obtained, from a generalized perturbation, by introducing magnetic fluctuations in an otherwise non-magnetic background.

4.3.3 Mean field Phase analysis of AuFe

Our model consists of N_A , A and N_B , B atoms uniformly distributed over M lattice sites and interacting via our estimated pair energies $J(|\mathbf{R}_i - \mathbf{R}_j|)$. These may vary in sign as a function of distance providing the main ingredient, frustration, in the system. The probability of an atom A occupying a specific site \mathbf{R}_k is $1/M$, as every site has equal probability of occupation. Similarly, the probability that a site is occupied by a A atom is N_A/M and a B atom is

N_B/M . In the thermodynamic limit, in the absence of any clustering or segregating effects,

$$\lim_{N_A, M \rightarrow \infty} \frac{N_A}{M} = x_A \quad \lim_{N_B, M \rightarrow \infty} \frac{N_B}{M} = x_B$$

x_A, x_B being the atomic concentrations of A and B constituents. The random ‘Hamiltonian’ is the same as shown in Eqn. (3):

$$\Delta E = \frac{1}{2} \sum_{QQ'} \sum_{\mathbf{R}_i, \mathbf{R}_j} J^{QQ'}(|\mathbf{R}_i - \mathbf{R}_j|) \delta \xi_i^Q \delta \xi_j^{Q'}$$

where,

$$J^{QQ'}(R) = E^{(2), QQ'}(R)$$

For a binary alloy, Q, Q' can be either A or B . $J^{QQ'}(|R_i - R_j|)$ is random depending upon

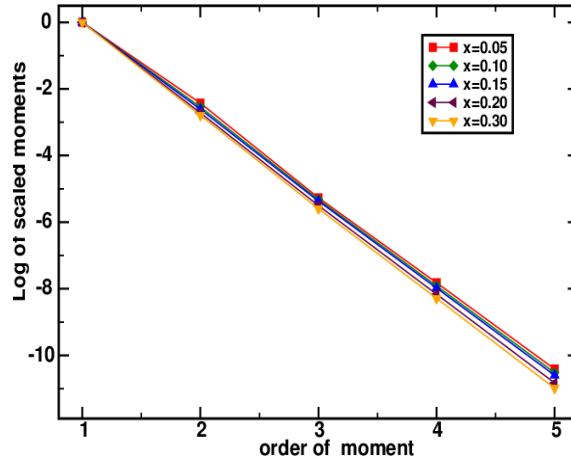


Figure 4.10: Decay of scaled moments I_n with n for AuFe

which type of atoms occupy the sites R_i and R_j . It can take on the values $J^{AA}(|R_i - R_j|)$, $J^{BB}(|R_i - R_j|)$ or $J^{AB}(|R_i - R_j|)$.

Introducing the single-site mean field approach by replacing the quadratic term $\delta \xi_i^Q \delta \xi_j^{Q'}$ by $\delta \xi_i^Q m_j^{Q'} + \delta \xi_j^{Q'} m_i^Q - m_i^Q m_j^{Q'}$ where m_i^Q is the thermal average $\langle \delta \xi_i^Q \rangle$, we can obtain

the Free energy as :

$$F = -\frac{1}{2} \sum_{QQ'} \sum_{R_j, R_j \in QQ'} J^{QQ'} (|R_i - R_j|) m_i^Q m_j^{Q'} + \frac{1}{\beta} \sum_Q \sum_{\mathbf{R}_i \in Q} \log \cosh(\beta h_i^Q) \quad (4.3)$$

where the local ‘Weiss’ fields are :

$$h_i^Q = \sum_{Q'} \sum_{R_j \in Q'} J^{QQ'} (|R_i - R_j|) m_j^{Q'} \quad (4.4)$$

In an ordered alloy we can define a homogeneous order parameter corresponding to the occupation variable of a Q type of atom as $m^Q = (1/N_Q) \sum_{i \in Q} m_i^Q$ and an average global order parameter as $m = \sum_Q x_Q m^Q$. In our disordered system inhomogeneities are in a macroscopic scale and this prevents us from introducing such an idea prior to some kind of configuration averaging. Rather we picture the system as follows : the net result of random pair energies connecting a local order parameter with its neighborhood is that it experiences a local random ‘Weiss’ field along which the average AS moment aligns. This leads to a *set of local order parameters* $\{m_i^Q\}$. In order to describe the local order parameters we need to know the distribution of the local ‘Weiss’ fields. This interpretation links our work with that of Thouless [Thouless et al., 1977] and Mookerjee [Mookerjee, 1978]. The free energy is a function of the whole set of *local* order parameters. The stable phase solution comes from the equations $\partial F / \partial m_i^Q = 0$ for all i . This leads to :

$$m_j^Q = \tanh \left[\beta h_j^Q \right] \quad Q, Q' \text{ can be } A \text{ or } B \quad (4.5)$$

For sufficiently high temperatures, the only consistent solution will be $m_i^Q = 0 \forall i$. At low concentrations of the magnetic constituent and as we lower the temperatures some of the local order parameters become non-zero and they are distributed randomly on the lattice. As many of them are + as they are -, so the net global order parameter may be zero, but the local one is still non-zero but random at Fe atoms. Moreover, there could be several different configurations of \pm order parameters which have the same free energy. This implies that rather than having a unique stable phase with non-zero global order parameter, we have a very corrugated free energy landscape with many minima differing in random distributions of

\pm moment carrying AS separated from each other by energy barriers. The resulting ‘phase’ may consist of domains with differing local AS configurations. One way of describing such an inhomogeneous picture is to find the distribution function of the scaled local ‘Weiss’ field. The scaling is carried out as follows : all $J(R)$ is replaced by $I(R) = J(R)/I_0$. In case there is only one magnetic constituent, the scaling is done with : $I_0 = \sum_R W(R)J(R)$. In case both the constituents are magnetic we have three factors I_0^{AA} , I_0^{AB} and I_0^{BB} and we scale with respect to $I_0 = \text{Max} \{I_0^{AA}, I_0^{AB}, I_0^{BB}\}$. Here $W(R)$ is the coordination number at a distance R from an origin.

The scaled ‘Weiss’ fields are given by :

$$\hat{h}_i^Q = \sum_{Q'} \sum_{R_j \in Q'} I^{QQ'}(|R_i - R_j|) m_j^{Q'}$$

The technique for the derivation of distribution function has been described earlier by Klein [Klein, 1968] and Mookerjee [Mookerjee, 1978] and the reader is referred to those papers for details. Here we shall quote the procedure and the main results. The probability is first expressed as a Radon transform of the Eqn.(4.4) and then the approximation is introduced in which we replace the delta-functional kernel of the Radon transform by its configuration average. Under the assumption that local ‘Weiss’ fields at different sites are uncorrelated : so that there is no clustering or short-ranged correlations between the local order parameters, we get

$$\mathcal{P}_Q(\hat{h}_i^Q) = \frac{1}{2\pi} \int dk e^{ik\hat{h}_i^Q} \prod_{Q'} \left[1 - \frac{F_{QQ'}(k)}{M} \right]^{N_{Q'}}$$

where,

$$F_{QQ'}(k) = \sum_R \int dz \mathcal{P}_Q(z) \left[1 - \exp \left\{ -ikI^{QQ'}(R) \tanh(\beta J^{QQ'}(R)z) \right\} \right]$$

In the thermodynamic limit :

$$\mathcal{P}_Q(\hat{h}_i^Q) = \frac{1}{2\pi} \int dk \exp \left\{ ik\hat{h}_i^Q - \sum_{Q'} x_{Q'} F_{QQ'}(k) \right\}$$

The direct calculations of the $F_{QQ'}(k)$ are tough as it stands, but let us expand the exponential and examine the terms :

$$F_{QQ'}(k) = \int dz \mathcal{P}_Q(z) \left[ikI_0^{QQ'} \tanh(\beta J_0^Q z) + \frac{k^2}{2} I_1^{QQ'} \tanh^2(\beta J_0^Q z) \dots \right. \\ \left. \dots + \frac{(-ik)^3}{6} I_2^{QQ'} \tanh^3(\beta J_0^Q z) \dots \right]$$

where

$$\sum_R W(R) I^n(R) = I_{n-1} \quad n = 1, 2 \dots$$

We define :

$$J_0^Q = \sum_{Q'} x_{Q'} m^{Q'} \sum_R J^{QQ'}(R) = \sum_{Q'} k_B T_{QQ'} m^{Q'}$$

$$J_1^Q = \sum_{Q'} x_{Q'} q^{Q'} \sum_R J^{QQ'}(R)^2 = \sum_{Q'} k_B^2 T_{QQ'}^2 q^{Q'}$$

and

$$m^Q = \int dz \mathcal{P}_Q(z) \tanh(\beta J_0^Q z)$$

$$q^Q = \int dz \mathcal{P}_Q(z) \tanh^2(\beta J_0^Q z) \quad (4.6)$$

Comparing Eqns. (4.5) and (4.6) we note that we can interpret m^Q and q^Q as the configuration averages $\ll m_i^Q \gg$ and $\ll (m_i^Q)^2 \gg$. Our frozen disordered local moment picture envisages spin-glass in AuFe as a ternary alloy $\text{Au}_{1-x}\text{Fe}_{x/2}^\uparrow\text{Fe}_{x/2}^\downarrow$, and that in NiMo as a quaternary alloy $\text{Ni}_{1-x/2}^\uparrow\text{Ni}_{1-x/2}^\downarrow\text{Mo}_{x/2}^\uparrow\text{Mo}_{x/2}^\downarrow$. For this phase $m^Q = 0$ but $q^Q \neq 0$. Thus the frozen disordered moment picture is consistent with our model for a spin-glass.

From Figure 4.10 we see that the moments I_{n-1} rapidly decrease as n increases. We shall therefore neglect all terms with I_{n-1} with $n > 3$. Then the probability densities become Gaussian. The distribution of the unscaled local 'Weiss' field $h = J_0 \hat{h}$ becomes :

$$\mathcal{P}_Q(h^Q) = \frac{1}{\sqrt{2\pi J_1^Q}} \exp \left\{ - (h^Q - J_0^Q)^2 / (2J_1^Q) \right\}$$

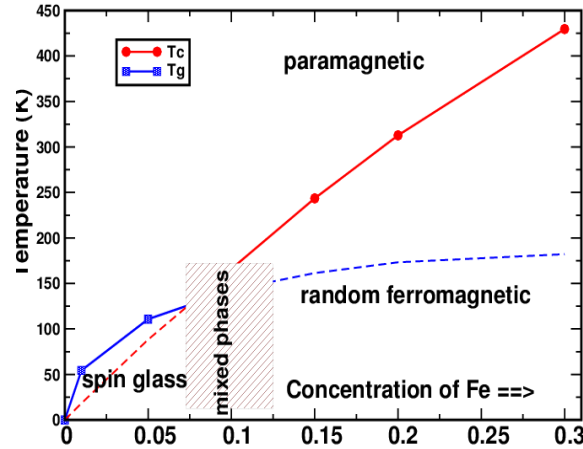


Figure 4.11: Phase diagrams for AuFe alloys

The equations (4.6) then reduce to the standard mean-field equations :

$$m^Q = \frac{1}{\sqrt{2\pi}} \int dz e^{-z^2/2} \tanh \left[\sum_{Q'} \frac{T_{QQ'}}{T} m^{Q'} + \frac{T^{g^2}_{QQ'}}{T^2} q^{Q'} z \right]$$

$$q^Q = \frac{1}{\sqrt{2\pi}} \int dz e^{-z^2/2} \tanh^2 \left[\sum_{Q'} \frac{T_{QQ'}}{T} m^{Q'} + \frac{T^{g^2}_{QQ'}}{T^2} q^{Q'} z \right]$$

The results are similar to many earlier work based on the distribution of local ‘Weiss’ fields, but it must be emphasized that our derivation has throughout made assumptions that take into account both a correct description of substitutional disorder and correct form of the pair energies. The scaling of both the mean and variance of the local ‘Weiss’ field with concentration of the magnetic component naturally arises in our results. Moreover, in this derivation we emphasize on the distribution of local ‘Weiss’ fields, so that the inhomogeneous picture of the system remains intact. m^A, m^B, q^A, q^B are being related to the moments of the local ‘Weiss’ field distribution.

One phase is characterized by $m^Q = 0, q^Q = 0$ so that the ‘Weiss’ field distribution is a delta function at $h^Q = 0$. This is obviously a paramagnetic phase with no local or global magnetization. Another phase is characterized by $m^A = 0, m^B = 0, q^A \neq 0, q^B \neq 0$. Here the distribution of the ‘Weiss’ fields are Gaussian with means at zero but with a non-zero

spread. How can such a phase be described ? Since the mean is zero the local magnetization positive at as many sites as it is negative. This is exactly the frozen disordered moment picture described earlier. The spin-glass phase boundary is given by :

$$T_g = \frac{1}{2} \left\{ (T_{AA}^g + T_{BB}^g) + \sqrt{(T_{AA}^g - T_{BB}^g)^2 + 4T_{AB}^g T_{BA}^g} \right\} \quad (4.7)$$

In case one of the constituents is non-magnetic, so that $J^{AB} = J^{BA} = J^{BB} = 0$, $J^{AA} \neq 0$ and $x_A = x$, $x_B = 1 - x$, as in the case of AuFe,

$$k_B T_g(x) = \sqrt{x J_1^A(x)} \quad (4.8)$$

Finally there is a third phase where $m^A \neq 0$, $m^B \neq 0$, $q^A \neq 0$, $q^B \neq 0$. For this phase the distribution of the local ‘Weiss’ fields are shifted Gaussians with a non-zero mean. So not only is there a distribution of different local moments, the global averaged moment is also non-zero. This is the random ferro-magnetic phase. This boundary is given by :

$$T_c = \frac{1}{2} \left\{ T_{AA} + T_{BB} + \sqrt{(T_{AA} - T_{BB})^2 + 4T_{AB}T_{BA}} \right\} \quad (4.9)$$

For the case of only one magnetic constituent, as in AuFe we get :

$$k_B T_c(x) = x J_0^A(x) \quad (4.10)$$

The derivation of the distribution of the local ‘Weiss’ fields in alloys with both components carrying moments has been done in detail earlier and we refer the reader to the work of Mookerjee and Roy [Mookerjee and Roy, 1983]. Figure 4.11 shows the phase boundaries between the paramagnetic, random-ferromagnetic and spin-glass phases for AuFe. Since we have seen that Au carries negligible local moment, we have used eqn. (4.8) and (4.10). The range in the concentration-temperature domain where we have the possibility of clustering and mixed phases has been blocked out, as our simple mean-field theory cannot hope to describe such phenomena. If we compare the phase diagram with experiment, qualitative agreement is immediately observed [Sarkissian, 1981]. Since this is a mean-field theory, we do not expect very good agreement quantitatively. However, the overall trend is well reproduced.

Chapter 5

Magnetic ordering in Ni-rich NiMn alloys around the multi-critical point

This chapter is based on

Pampa Pal, **Banerjee**, **Rudra**, Radheshyam Banerjee, Abhijit Mookerjee, Gopi Chandra Kaphle, Biplab Sanyal, Olle Eriksson, P. Mitra, A. K. Majumdar, and A. K. Nigam. Magnetic ordering in Ni-rich NiMn alloys around the multi-critical point : Experiment and Theory . *Phys. Rev. B (accepted)*, 2012.

5.1 Introduction.

Magnetism in $\text{Ni}_{100-x}\text{Mn}_x$ alloys provides a classic example of a disordered system with competing interactions. In an early work, Hahn and Kneller [Hahn and Kneller, 1958] carried out magnetic studies on Ni-Mn alloys as a function of heat treatment. They found that in spite of quenching from well above the ordering temperature, there exists small ferromagnetically ordered Ni_3Mn regions of about 20 Å in diameter in a matrix of the disordered material. This made the preparation of homophase Ni-Mn alloys a difficult task. Soon after, Kouvel and Graham [Kouvel and Graham Jr, 1959] established the coexistence of ferromag-

netism and anti-ferromagnetism coming from competing pair exchange interactions between the components at low temperatures in disordered $\text{Ni}_{100-x}\text{Mn}_x$ alloys with $x = 20, 25,$ and 30 , through hysteresis loop and torque measurements.

Kouvel et.al. [Abdul-Razzaq and Kouvel, 1987] reported the magnetic phase diagram in the composition range $23 \leq x \leq 27$. They observed, below the multi-critical point (MCP) of $x = 23.9$ and $T = 102$ K, a double transition from a paramagnetic to a ferromagnetic state at T_C followed by a spin-glass(SG)-like state at $T_{fg} < T_C$ with a re-entrant character. Above $x = 23.9$ they found a paramagnetic to a normal SG state at T_g .

Aitken et.al. [Aitken et al., 1982] found the MCP to be above $x = 26$. This difference could arise from the difference in atomic short-range order in the two works. Hauser and Bernardini [Hauser and Bernardini, 1984] studied sputtered films of $\text{Ni}_{100-x}\text{Mn}_x$ alloys and their bulk counterparts. They observed paramagnetic to spin glass transition through ac-susceptibility, $\chi(\omega)$ measured at 10 kHz and 4 Oe a.c. field. from 14.7×10^{-3} for $x = 22$ where $T_C \sim 290$ K and $T_g \sim 40$ K. They concluded that the presence of ferromagnetism below $x = 26$ is independent of preparation conditions, be they induction melted or quenched bulk alloy or sputtered films. However, the magnetic parameters like T_C , T_g , $\chi(T)$, etc. varied considerably.

Needless to say that a more detailed magnetic phase diagram of this interesting system is certainly necessary, especially away from the multi-critical composition.

Previous theoretical studies [Gabay and Toulouse, 1981; Mookerjee and Roy, 1980] had also shown that this SG-like phase below T_{fg} may have a spontaneous FM moment with the transverse spin components ordered in a spatially random manner. It has therefore been called a ‘mixed phase’. We indeed found that the SG-like phase has a spontaneous moment and the FM to SG-like transition temperature (T_{fg}) increased while the FM Curie temperature (T_C) decreased with increasing Mn concentration. They met at $x = 25$ and $T \sim 100$ K, the multi-critical point (MCP). For alloys with $x = 30$ and 35 , we observe only a single transition from paramagnetic to a spin-glass-like (or anti-ferromagnetic) phase which is different from that of the previous ‘re-entrant spin-glass’ phase. At higher concentrations like $x = 37$, a paramagnetic to an anti-ferromagnetic transition is noticed.

We shall interpret the above behavior in terms of a Weiss field constructed out of the

Ruderman-Kittel-Kasuya-Yoshida (RKKY) kind of indirect exchange interaction between the moments mediated by the conduction electrons as in an itinerant magnetic system rather than the pair interactions of a localized model. In this model the dominant exchange energies are anti-ferromagnetic Mn-Mn and ferromagnetic Ni-Ni and Ni-Mn interactions [Carr, 1952]. According to this model, for low Mn concentration (x), Mn-Mn interaction is negligible and hence all the spins become parallel resulting in an increase in M falling on the right segment of the Slater-Pauling (SP) curve (moment/atom vs. electron/atom) with a slope of -1. For disordered alloys with somewhat higher x , the Mn-Mn AF interaction wins over the Ni-Mn FM interaction and Mn spins tend to cancel each other. As a result M decreases with x and start following the left segment of the SP curve. At still higher x , Ni 3d minority band gets gradually filled reducing the magnetization and due to the Z-difference of 3 between Ni and Mn ferromagnetism is lost for $x \sim 30$, which is what is found in most experiments. The magnetic behavior of Ni-Mn alloys is typical of a competing interacting system with ferromagnetic and anti-ferromagnetic regions enclosing a concentration regime in which only magnetic short-range order (MSRO) exists

5.2 Samples

We have investigated in detail the magnetic properties of six samples of disordered $\text{Ni}_{100-x}\text{Mn}_x$ alloys enclosing the critical concentration ($x = 25$) in the composition range $x = 15 - 37$ at.% Mn which was the transition region from ferromagnetism to antiferromagnetism as shown in Table. 5.1.

For alloys with $x = 15$ and 20, on decreasing the temperature, we observed a paramagnetic (PM) to a ferromagnetic (FM) transition at T_C and then below T_{fg} the occurrence of a spin-glass (SG)-like phase.

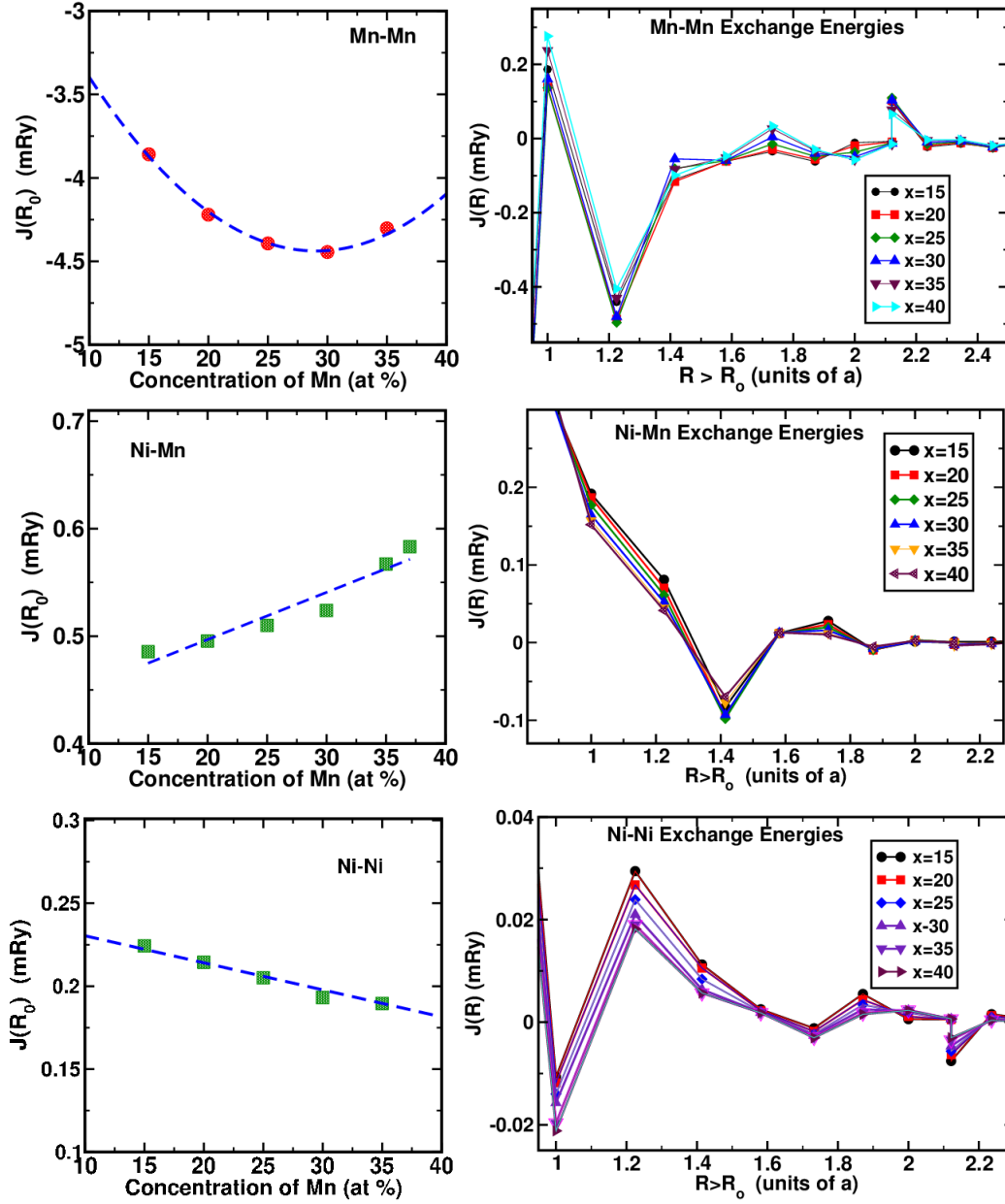


Figure 5.1: EPE for $\text{Ni}_x\text{Mn}_{1-x}$ alloy. Left column: EPE for the nearest neighbor distances. It is seen that the Mn-Mn EPE is anti-ferromagnetic and most dominant; whereas, those for Mn-Ni and Ni-Ni are ferromagnetic but relatively weak. Right Column : EPE for second nearest neighbor and further distances. The oscillatory behavior shows the possibility of frustration.

#	Ni	Mn	Å
1	85	15	3.572
2	80	20	3.583
3	75	25	3.595
4	70	30	3.615
5	65	35	3.654
6	63	37	3.670

Table 5.1: Atomic concentration of NiMn alloy and lattice parameters.

5.3 Ordering of magnetic moment carrying atomic spheres

In order to understand the onset of magnetic ordering in random alloys, we proceeded in two steps. The formation of a magnetic moment within an atomic sphere was analyzed using the TB-LMTO-ASR as described above. This is an itinerant electron picture where the moment is produced by an exchange splitting of the majority and minority spin projected densities of states. However, the ordering of these moment carrying atomic spheres is studied via derivation of the lowest configurational energy for a specified spin configuration. Models have been set up describing configurational energies in terms of effective multi-site interactions, in particular “effective pair energies” (EPE). Within this approach, the analysis of alloy ordering tendencies and phase stability reduces to accurate and reliable determinations of these EPE. We have calculated EPE on $40 \times 40 \times 40$ lattice. The oscillatory behavior of Mn-Mn, Mn-Ni and Ni-Ni EPE with distance and also the fact that nearest neighbor Mn-Mn EPE is anti-ferromagnetic where Mn-Ni EPE and Ni-Ni EPE are ferromagnetic. This is a clear indication of strong frustration in the system. The $J^{NiNi}(0)$ increases with increase of Ni concentration, consistent with the fact that Ni has very fragile magnetic moment and depends heavily on its surroundings. When Ni concentration is high, its more likely to be surrounded with more Ni atoms and the dominant $J^{NiNi}(0)$ increases. On the other hand the dominant EPE for both Mn-Mn and Mn-Ni decreases with increase of Ni concentration.

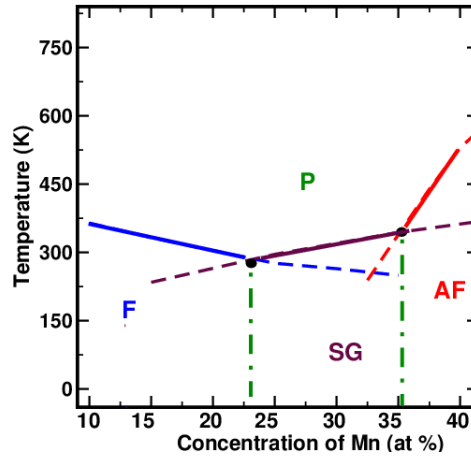


Figure 5.2: Phase diagram of NiMn based on a mean field calculation.

5.4 Mean field analysis of the random Ising model

Mookerjee and Roy [Mookerjee and Roy, 1983] have studied the $T = 0$ phases and have shown that there exists a critical concentration x_C which separates the spin-glass from the ordered phases. We have also carried out a mean field calculation and obtained the magnetic phase diagram in Figure 5.2.

5.5 Magnetic relaxation

The spin-glass state has a very complex phase space and a lack of ergodicity [Mookerjee and Roy, 1983]. This leads to interesting dynamical behavior where relaxation of magnetization is characterized by a wide spectrum of relaxation times [Chowdhury and Mookerjee, 1983]. Hellsvik et.al. [Hellsvik et al., 2008] has suggested that an aging experiment is an elegant way to exhibit the multi-scale nature of dynamics in a spin-glass. In an aging experiment, the alloy is quenched from a high temperature in zero field, down to temperatures below the critical temperature (T_C or T_g). The aging now proceeds for a ‘waiting time’ t_w during which a small external field h is applied and the subsequent relaxation of magnetization $m(t)$ is measured. After quenching the magnetization first relaxes towards a local equilibrium

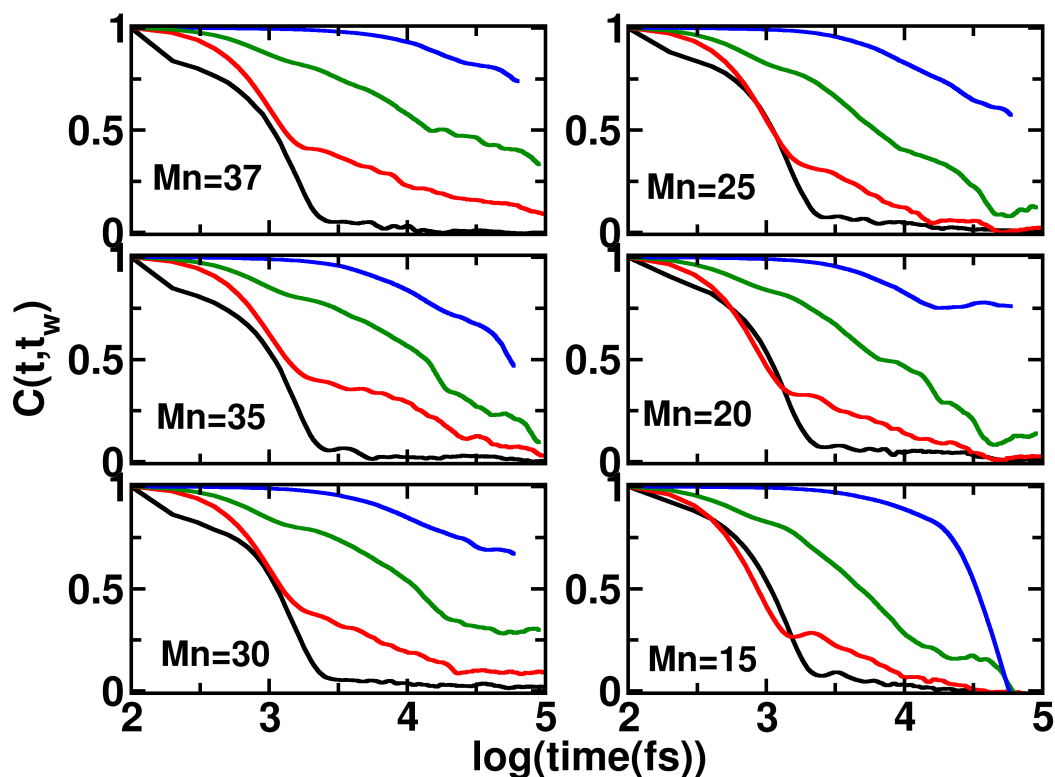


Figure 5.3: Auto correlation functions for $\text{Ni}_{1-x}\text{Mn}_x$ alloy. The figure shows anomalous slowing down of auto-correlation for $x = 30$. The aging behavior within the range $20 \leq x \leq 35$ agrees with the experimental suggestion of spin-glassy behavior for these compositions. Breakdown of aging at $x = 15$ and $x = 37$ also agree with the experimental suggestion of transitions to random ferromagnetic and random anti-ferromagnetic states respectively, at these compositions [Pal et al., 2012].

state. Subsequently, if there is a glassy state present the magnetization proceeds with aging dynamics. In the absence of a glassy state, the system relaxes towards the global equilibrium state rather fast. In glassy states this latter type of relaxation is not achievable as the time scale required is greater than the ergodic time $\tau_{\text{erg}} \sim \exp N$. In the absence of glassy state, time translation in variance is satisfied and magnetic relaxation does not depend

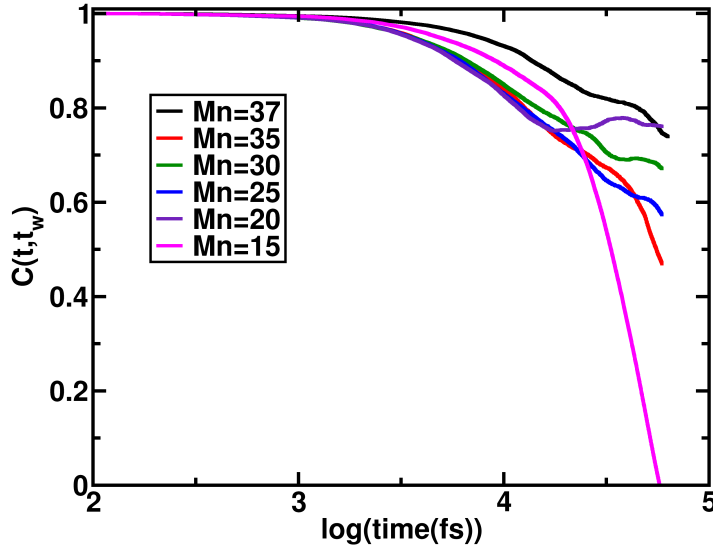


Figure 5.4: Comparison of NiMn alloy with different composition for highest waiting time used (blue curves in Figure 5.3).

strongly on waiting times : $C_{\text{eq}}(t) = C(t_w + t, t_w)$. However, in a glassy state the fluctuation-dissipation theorem is violated and aging is observed. The aging behavior of diluted magnetic semiconductors [Hellsvik et al., 2008] has been studied recently by the same approach.

The magnetic pair energies $J^{QQ'}(R)$ are used to calculate the spin-spin auto-correlation functions via a Landau-Lifshitz-Gilbert (LLG) equation of motion.

The spin-spin autocorrelation function

$$C(t, t_w) = \frac{1}{N} \sum_{\mathbf{R}} \left\langle \left\{ \vec{m}_{\mathbf{R}}^Q(t) \cdot \vec{m}_{\mathbf{R}}^Q(t + t_w) \right\} \right\rangle \quad (5.1)$$

carries the signature of this critical slowing down of magnetic relaxation. It is an important tool to study the existence of the spin glass phase. We have used an atomistic approach as proposed by Skubic et.al.[Skubic et al., 2008]. Skubic's approach, based on density functional theory starts with LLG equation. It allows us to carry out finite temperature calculations by including a stochastic magnetic field ($\vec{b}_{\mathbf{R}}(t)$).

These alloys often exhibit macroscopic magnetic anisotropy in experiments [Monod and

Berthier, 1980]. We shall, for the time being, ignore such anisotropy effects, and shall assume that some mechanism exists to provide magnetic damping. This will be parameterized by α . For the present we shall not attempt to obtain this parameter until we have identified the mechanism for damping. We shall set $\alpha=0.1$.

We have performed atomistic spin dynamics simulations using UppASD code [Ericksson, 2009]. The calculations have been carried out on a $30 \times 30 \times 30$ lattice. In Figure 5.3, we have shown $\log(C(t, t_w))$ vs t at three compositions across the composition range for different logarithmically separated waiting times. The long waiting time regimes show no aging behavior for $x = 15$. At $x=30$ (in fact, at all concentrations between $x = 20$ and $x = 35$, not shown in the figure for compactness) aging behavior is prominent. Then at $x=37$ and higher, aging behavior begins to break down.

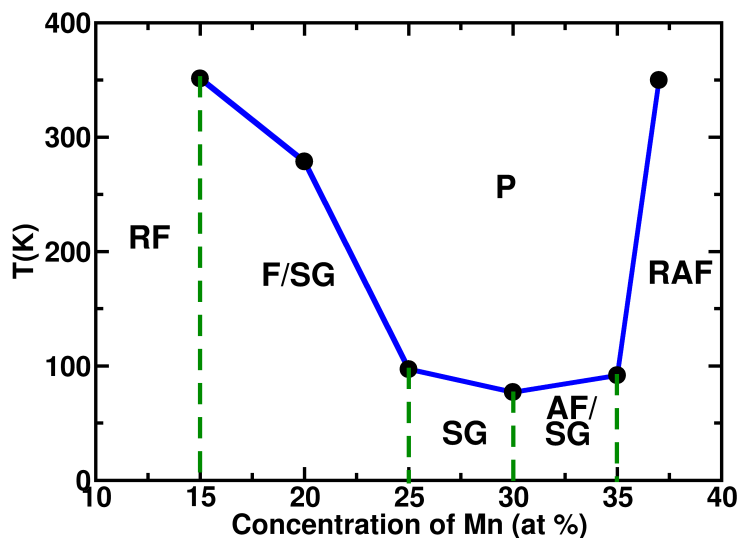


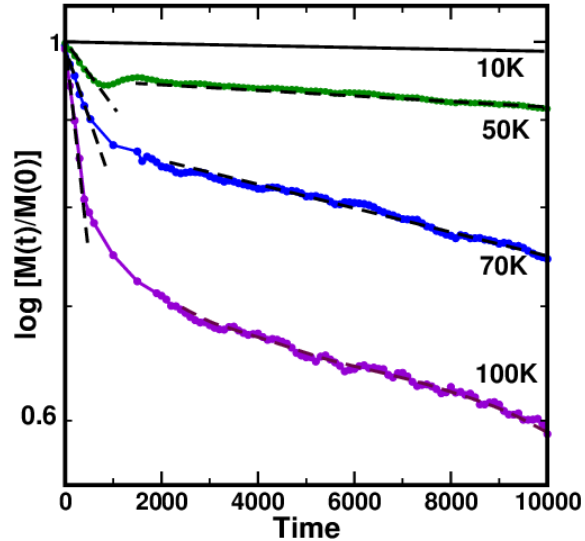
Figure 5.5: Proposed phase diagram from Monte Carlo simulations followed by the aging analysis

Preliminary Monte Carlo simulations showed that critical slowing down occurs close to the temperatures shown in Figure 5.5. The LLG analyses were carried out at temperatures well below these critical temperatures. Our analysis was in two steps. A DFT based calculation of

the formation of moments in atomic spheres and a statistical analysis of the free-energetically the most favorable arrangement of these moment carrying spheres. Since the DFT part was done for uniaxial spins, we were unable to describe the ferro-spin-glass or the anti-ferro-spin-glass mixed phases. Since the moments are randomly canted in these phases [Mookerjee and Roy, 1983] it would have required a generalization of the DFT part to allow description of non-collinear magnetic moments before carrying out the statistical analysis of their favorable arrangements. Recently such a generalization has been carried out for the TB-LMTO-ASR [Ganguly et al., 2011] and our immediate future plan would be to implement the Lichtenstein formula within this formalism and describe the mixed phases.

Temp(K)	τ_1	τ_2
100	813	140
70	449	120
50	200	41

(a)



(b)

Figure 5.6: (a) Theoretical study of decay of magnetization with time. The decay rates for the initial fast decay and the subsequent decay to a global minimum ($m(t)/m(o) = \exp(-\tau t)$) are shown for both the experimental data [Pal et al., 2012] and LLG simulation results. The alloy shows freezing behavior at low temperatures. (b) LLG results for the time decay of magnetization for the $\text{Ni}_{75}\text{Mn}_{25}$ alloy at different temperatures. Here too the alloy magnetization shows anomalously slow relaxation as we approach and cross the glass-transition temperature below 100K.

5.6 Conclusions

We conclude from a detailed experimental magnetic study of several disordered $\text{Ni}_{1-x}\text{Mn}_x$ alloys that the spin-glass-like state in these alloys below T_{fg} has a spontaneous (FM) moment. This moment decreases slowly with rising temperature and merges smoothly with the spontaneous moment of the FM state at the multi-critical point (MCP) around 25 at.% Mn. The existence of the reentrant SG phase, a canonical SG phase, and the onset of an antiferromagnetic phase around 37 at.% Mn is also confirmed. In brief, we found ferromagnetic LRO with re-entrant spin-glass (RSG)/ferro-spin-glass (FSG) phase for $x \leq 25$, an anti-ferromagnetic LRO around $x \sim 37$, and a gradual change from a canonical spin-glass state (which is nothing but a short-range anti-ferromagnet) to a long-range AF phase in the intermediate composition region.

Chapter 6

Magnetic properties of FeNiMo alloy

This chapter is based on

Mitali Banerjee, **Rudra Banerjee**, A.K. Majumdar, Abhijit Mookerjee, Biplab Sanyal, and A.K. Nigam. Magnetism in NiFeMo disordered alloys: Experiment and theory. *Physica B: Condensed Matter*, 405(20):4287–4293, 2010. ISSN 09214526.

R. Banerjee, M. Banerjee, AK Majumdar, A. Mookerjee, B. Sanyal, J. Hellsvik, O. Eriksson, and AK Nigam. Fe_{3.3}Ni_{83.2}Mo_{13.5}: a likely candidate to show spin-glass behaviour at low temperatures. *J. Phys.: Condens. Matter*, 23:106002, 2011.

High permeability and low magnetostrictive properties of Ni-Fe permalloys are widely used in making magnetic cores for light electrical equipment applications. They are also useful as magnetic shielding materials. Applications being one of the primary concerns in science and technology of materials, permalloys are still attractive systems to study. High permeability is expected to result from domain rotation against weak crystalline anisotropy or from boundary displacements where the opposing force is small [Bozorth, 1953]. Considerable work has been done earlier substituting Fe by other 3d transition elements like Cr and V in Ni-Fe permalloys [Chakraborty and Majumdar, 1998b,a] but very few of them considered 4d or 5d elements for substitution like Mo, or W, partly due to their high melting temperatures.

In the present and next chapter we will study some Ni-rich Mo and W substituted permalloys.

Mo enhances the permeability of the material, even if a small amount is added. A high permeability can also be obtained if the amount of Ni is reduced. Mo at the same time increases the electrical resistivity of permalloys and hence reduces eddy current losses. Magnetic heads consisting of NiFeMo alloys assures excellent high frequency characteristics. It is relatively easy to form magnetic domain structures without any special heat treatment (U.S. Patent 6376108 B1, 2002). We will present our first principle density functional theory based calculation to try to understand the physics behind the problem.

6.1 Sample

The samples we used are shown in Table 6.1. This is based on our experimental sample and lattice parameters are also determined from experiment. Experimental result shows the lattice is FCC.

#	Ni	Fe	Mo	a(Å)
1	81.0	16.7	2.3	3.3558
2	80.4	12.9	6.7	3.566
3	83.4	10.7	5.9	3.568
4	83.5	7.6	8.9	3.561
5	83.1	6.0	10.9	3.565
6	83.2	3.3	13.5	3.571

Table 6.1: Atomic % of Ni, Fe and Mo in the six alloy samples and lattice constant.

6.2 Experimental Motivation¹

The electronic configurations of Mo is $[\text{Kr}] 4d^5 5s^1$, while those of Fe and Ni are $[\text{Ar}] 3d^6 4s^2$ and $[\text{Ar}] 3d^8 4s^2$. The melting point of Mo is as high as 2890 K. Hence it is difficult to make homogeneous alloys with Mo as additive.

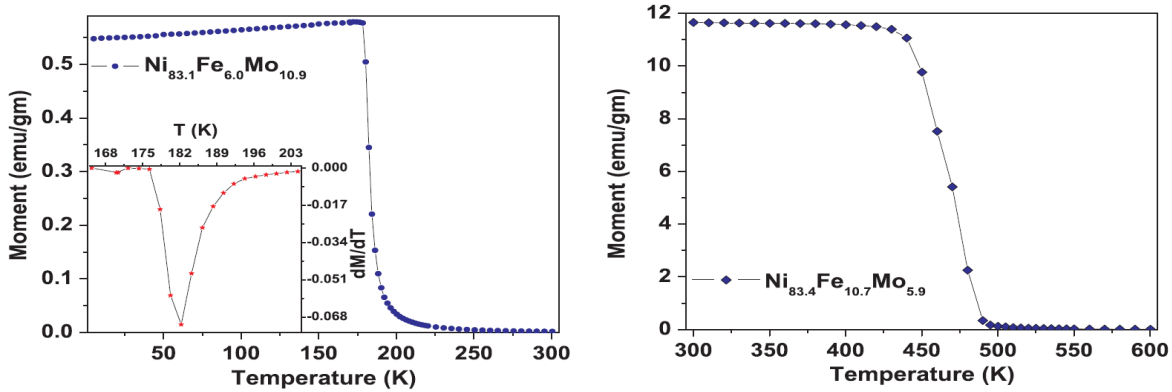


Figure 6.1: Magnetization vs Temperature for two compositions (left) sample 5 with 10.9 at.% Mo, 6.0 at.% Fe and lower T_c and (right) sample 3 with 5.9 at.% Mo, 10.7 at.% Fe and higher T_c .

In experiment, concentration of Ni roughly around 80-83 at.% and varied that of Fe and Mo. The samples (3)-(6) belong to one group, where the Ni concentration is fixed at ~ 83 at.% and increasing Mo and decreasing Fe content. Samples (1) and (2) belong to a slightly different group with a lower Ni concentration of ~ 80 at.% and relatively higher Fe content than those in the other group.

Figure 6.1 shows the magnetization vs temperature curves for two representative samples : one with a higher Mo concentration of 10.9 at.% and lower Fe concentration of 6 at.% (sample 5, taken at 20 Oe) and the other with a lower Mo concentration of 5.9 at.% and a higher Fe concentration of 10.7 at.% (sample 3, taken at 50 Oe). As shown in the inset, the critical temperature T_c is obtained from the dip in dM/dT which corresponds to the point

¹This section is based on [R. Banerjee et al., 2011; Banerjee et al., 2010b] and partly included in the thesis of Dr. Mitali Banerjee

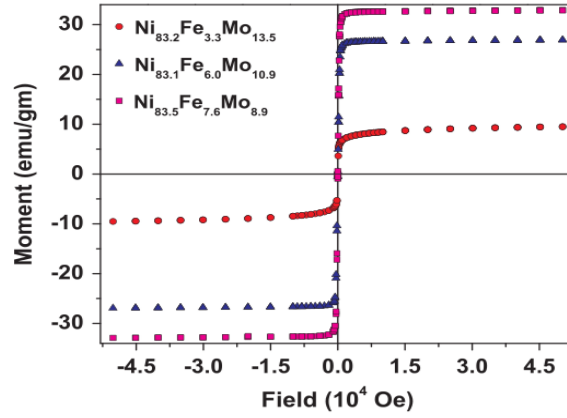


Figure 6.2: $M(H)$ vs H taken at 5 K for samples (4), (5) and (6).

of inflection in the M vs T curves. The higher the Fe concentration the higher is the T_c , while the reverse trend is seen with increasing Mo concentration.

Figure 6.2 shows the M vs H curves for three representative samples (1),(3) and (4) (numbers refer to that given in Table 1). All experiments were carried out at 5K. The saturation fields are very small in all three cases and the magnetization very quickly saturates. None of the samples show appreciable hysteresis. All three cases are clean random ferromagnets. The saturation magnetization decreases with increasing Mo and decreasing Fe concentrations.

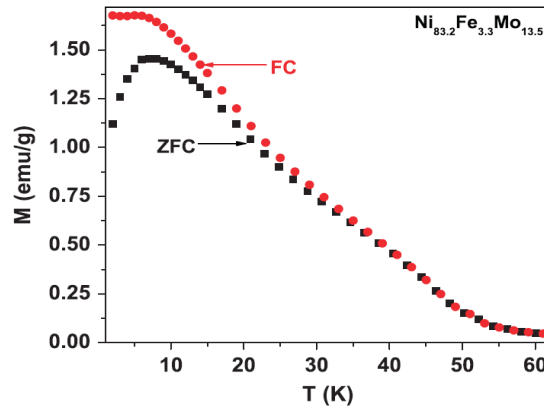


Figure 6.3: M vs T results for sample (6) with both field-cooled and zero-field-cooled situations.

The sample (6) shows a different behavior. Figure 6.3 shows the M vs T results for this sample both for field-cooled and zero field-cooled cases. They now bifurcate at low temperatures around 30 K. This is a signature of memory effects characteristic of a spin-glass transition. We shall show later from our theoretical analysis that there is the possibility of a spin-glass transition at around this composition. More careful experiments are suggested in the neighborhood of this compositions to confirm (or otherwise) our prediction.

The Table 2 summarizes our results. Note that we have converted the magnetization results from emu/g to μ^B units in order to compare with theoretical estimates.

Sample	a (A)	Ms		T_c (K)
		(emu/g)	μ^B	
1	3.558	80.5	0.85	720
2	3.565	53.6	0.56	495
3	3.568	51.3	0.54	470
4	3.561	32.5	0.34	320
5	3.565	26.5	0.28	182
6	3.571	7.9	0.08	10 (T_g)

Table 6.2: Summary of experimental results on the six alloy samples.

6.3 Electronic structure and magnetic moments

The usual statistical mechanical models used to study magnetism and magnetic phase diagrams of alloys involve the Ising and Heisenberg models, both of which involve localized moments. Straightforward application of such models in our problem is inadmissible. It is generally believed that Ni-rich alloy systems usually are itinerant magnets. Consequently, these localized spin models are inappropriate for these systems. In order to describe our alloys we have to begin with an itinerant picture. This we shall do within a local spin density functional (LSDA) approach. We shall begin with the Kohn-Sham equation for the of valence electrons in the alloy. Our choice of electronic structure methods will be guided by the fact that subsequently we shall have to model substitutional disorder. We shall choose

the tight-binding, linear muffin-tin orbitals method (TB-LMTO)[§2.4.3]. Since the system is disordered, our description of self-averaging properties will require configuration averaging. In this work we have primarily used the ternary alloy version of the augmented space recursion (ASR)[§2.6]. Once we have calculated the configuration averaged Green function $\ll G_{\mathbf{R}_i L \mathbf{R}_i L}^\sigma(E) \gg$ we obtain immediately the local density of states, the charge and magnetization densities and the local magnetic moment per atom. Within the TB-LMTO procedure the solid is partitioned into atom-centric atomic spheres (AS) labeled by \mathbf{R}_i . $\Phi(\mathbf{r} - \mathbf{R}_i)$ is the wave function in an AS and $\rho(\mathbf{r} - \mathbf{R}_i)$ is the charge density within it. $m(\mathbf{r} - \mathbf{R}_i)$ is the magnetic moment density in that AS. From this description it is clear that the magnetic moment is smeared across the AS. $m(\mathbf{R}_i)$ integrated over an AS is the average magnetic moment associated with it. These magnetic moments are thus built up out of itinerant electron charge densities associated with different spins.

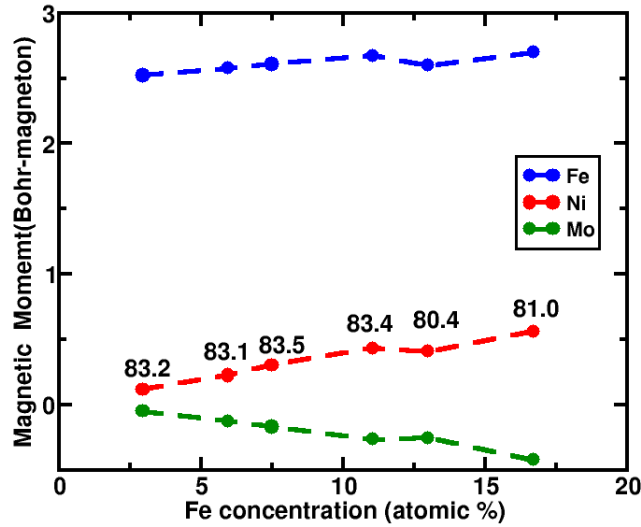


Figure 6.4: Local magnetic moments per atom on Fe, Ni and Mo sites as a function of composition. The labels indicate (the concentration of Ni which is kept around 80-83 at.%.)

Figure 6.4 shows the local magnetic moments on the Fe, Ni and Mo atoms in the alloy.

These local moments were not accessible by the experiments we carried out. However, it will be instructive to analyze the theoretical results. The Ni concentrations are almost invariant across the six samples, fixed around 83 at.% for the first four and around 80 at.% for the last two. The Fe moment changes very slowly across the composition range. That for Ni increases linearly as Fe concentration increases and correspondingly Mo concentration decreases. For the last two samples the Mo concentration is higher, and the Ni local moment is correspondingly decreased. The moment on Mo is small and opposite to that of Fe and Ni. Its behavior is a mirror image of that for Ni.

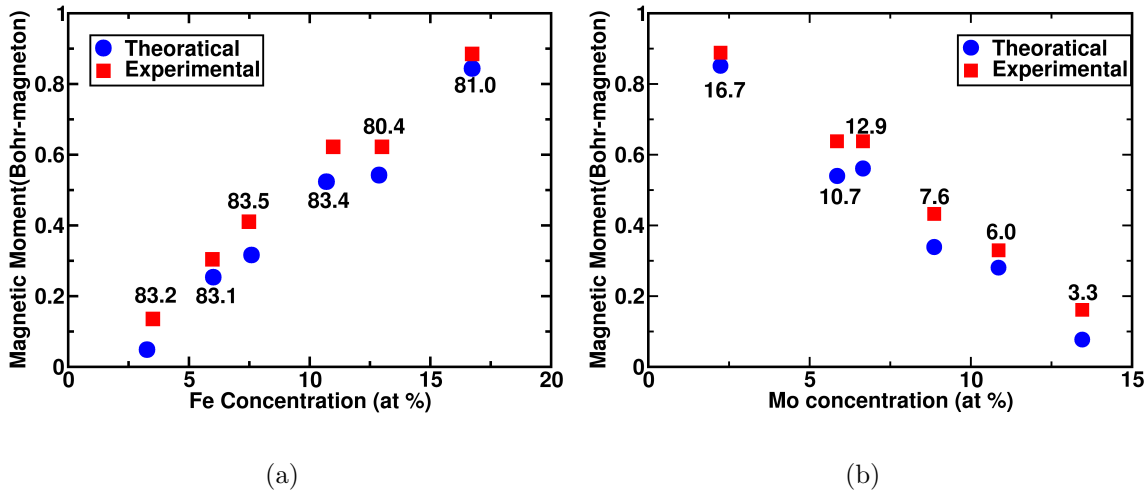


Figure 6.5: Local magnetic moments on Fe, Ni and Mo sites as a function of composition. The labels indicate (a) the concentration of Ni which is kept around 80-83 at.%. (b) the concentration of Fe in at.%.

Figure 6.5 shows the experimental saturation magnetic moments at 5K for the alloys at the six compositions, described earlier, as compared with the theoretical magnetic moment estimates. Given the approximations involved in the theoretical estimates, the two agree reasonably well across the composition range. The magnetic moment is boosted when Fe concentration increases and the increase is almost linear. The opposite occurs when the Mo concentration increases against that of Fe. In the fifth (from the left) composition shown in the Figure 6.5(a), Mo concentration increases against Ni. Although the Fe concentration

increases as we go from the fourth to the fifth composition (from the left), increase in the Mo concentration causes the the moment not to increase as expected. The same is clear from the Figure 6.5(b) : although the Mo concentration increases as we go from the second to the third sample (from the left), increase in the Fe concentration against Ni causes the magnetic moment to increase. The general picture is that Fe boosts magnetism and Mo depletes it. In the ternary alloy, there is a competition between these two.

6.4 Magnetic ordering

The panels in Figure 6.6 show the pair energies for all possible pairs. Among them Fe-Fe, Fe-Ni, Fe-Mo and Ni-Ni are dominant; other pairs are negligibly small and may be neglected. The following comments may be made at this stage :

- (i) The strongest pair energies are Fe-Fe, Fe-Ni and Fe-Mo, followed by Ni-Ni. The Ni-Mo and Mo-Mo terms are negligible.
- (ii) The Fe-Fe pair energy is almost independent of composition. Fe compositions vary from 3 to 17 at.%. All other pair energies are strongly composition dependent. The Fe-Ni coupling is ferromagnetic up to the third nearest neighbors and increases with Fe concentration. It is known from earlier work on NiFe [Sanyal and Mookerjee, 1998] that Fe atoms in the neighborhood of Ni enhances its moment. This is a reflection of that. The Ni-Ni pair energies increase when Fe concentration increases and diminishes as Mo concentration increases. These pair energies show the effect of enhancement by neighboring Fe, when Fe concentration increases and its fragility as it becomes negligible as Mo concentration is increased. Similarly, higher Fe concentrations leads to a small Mo-Fe coupling, which becomes negligible at lower Fe concentrations. The behavior of the pair energies indicate : a strong magnetism in Fe, which can induce magnetism in Ni and Mo; a weak, fragile magnetism in Ni and a very weak, induced magnetism in Mo.
- (iii) Figure 6.6 shows the oscillatory behavior of Ni-Ni pair energies with the variation of $R = |\mathbf{R}_i - \mathbf{R}_j|$ for $R \geq a$. For low concentrations of Mo the second, fifth and

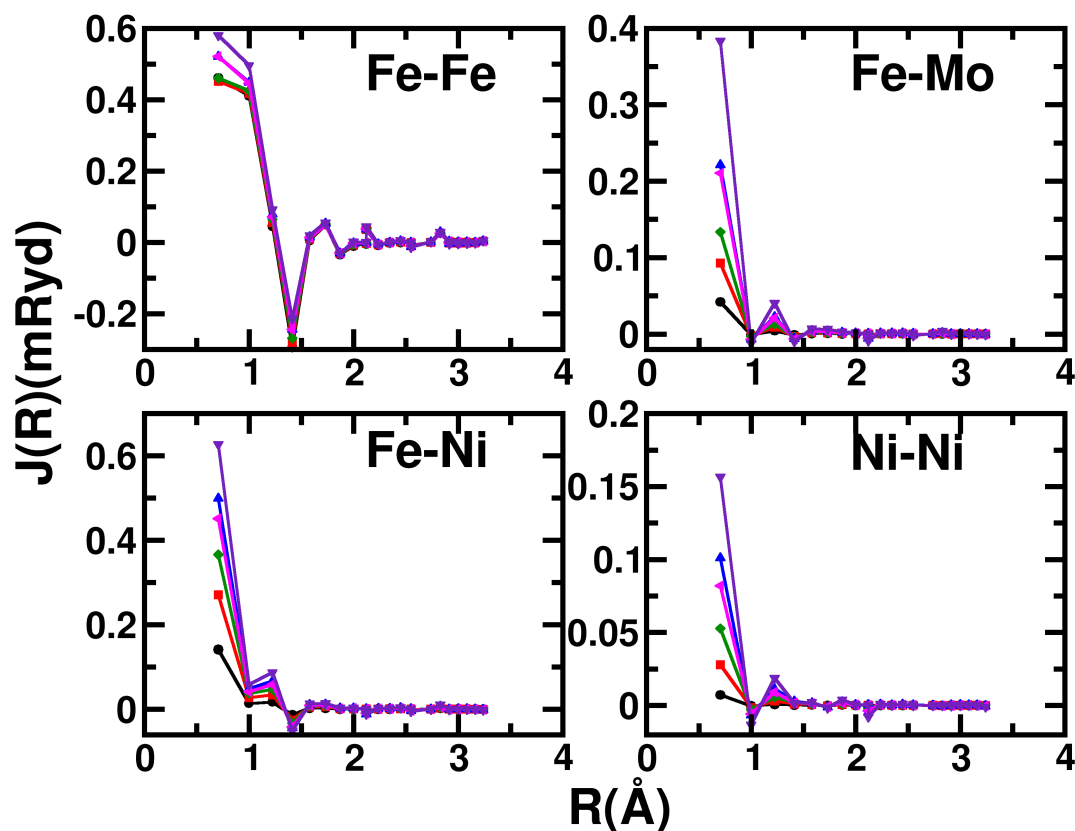


Figure 6.6: The dominant pair energies between Fe-Fe, Fe-Mo, Fe-Ni, and Ni-Ni for compositions with Fe content varying from 3 to 17 at %. (Magenta)=#1, (Violet)=# 2, (Blue)=# 3, (Green)=# 4, (Red)=# 5 and (Black)=# 6 of Table 6.1

tenth neighbor are anti-ferromagnetic. This would lead to frustration on triangular and quadrilateral plaquettes in a cubic unit cell of the face-centered cubic lattice. As the Mo concentration increases, these interactions become less negative and eventually ferromagnetic. As a consequence, frustration on those triangular and quadrilateral plaquettes decreases. We generally expect that the spin-glass phase occurs at larger Mo concentrations. Not only does frustration decrease at these compositions, the magnetic moment of Ni itself becomes small exactly at these same compositions. Consequently

we may find paramagnetism rather than spin-glass behavior at these compositions. Therefore, like NiMo, in NiFeMo too we may expect spin-glass in a very small range in the temperature-composition phase diagram.

- (iv) Figure 6.6 also shows that the pair energies decay with distance R . The behavior is a signature of an exponentially decaying oscillatory interaction. The exponential decay is due to disorder scattering which dampens the usual algebraically decaying oscillatory interaction. As the Mo concentration increases, the range of interaction rapidly decreases, until for the composition 83.2:13.8:3 it is almost nearest neighbor as all other pair energies for $R > a$ become negligibly small.

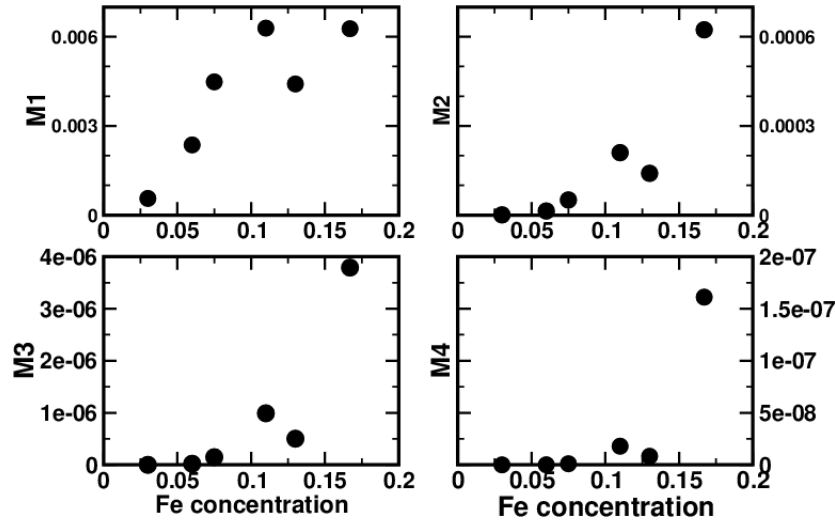


Figure 6.7: The first four moments of the probability distribution of the Ni-Ni pair-energies shown as functions of Fe concentration.

- (v) Figure 6.7 shows the moments

$$M_n = \sum_{R>a} W(R) \{E^{(2),NiNi}(R)\}^n$$

where $W(R)$ is the coordination number. Since the sites are randomly occupied by Ni atoms, this randomness is reflected in the randomness in R and hence $E^{(2),NiNi}(R)$. The above moments therefore characterize the distribution in the pair-energies.

-
- (a) The first moment is positive throughout the composition range showing that on the average the pair-energies favor ferromagnetism rather than frustration. Since the nearest neighbor pair-energy ($R = a/\sqrt{2}$) is left out in the calculation of the moments and the first moment goes to zero around Fe concentration of 2-3 at.% and Mo concentration of around 14-15 at.%, at these compositions the pair-energy is almost nearest-neighbor.
 - (b) The second moment also goes down to zero at Mo concentrations of 14-15 %. This indicates that the distribution becomes delta-function like around the average or mean value.
 - (c) The third and fourth moments measure the asymmetry and kurtosis of the distribution. Both becoming small indicates that the distribution becomes close to Gaussian when Mo concentration is around 14-15 at.%.

The behavior of the moments indicate that at those compositions where we expect the spin-glass phase to be stable, the distribution of $E^{(2),NiNi}(R)$ is a delta function centered at zero. This is an indication that the moment on Ni may itself vanish at these compositions.

6.5 Mean-field analysis of transition temperatures

Figure 6.8 shows the mean-field phase diagram for NiFeMo. Ni being a fragile magnet, rapidly loses magnetic moment as Mo increases and exactly where we expect the spin glass phase to exist ($T_g > T_c$) the system becomes paramagnetic. Existence of the spin-glass phase in NiMo has not been reported. However, in the ternary NiFeMo, addition of Fe enforces magnetism in Ni and around Mo concentration of 14-15% the T_c and T_g curves intersect and there is a possibility of the spin-glass phase. The mean-field estimates of the transition temperatures are never very accurate, therefore the best we can say is that exact critical composition where we expect a spin-glass phase is around 14-15% of Mo and around 80-83% of Ni.

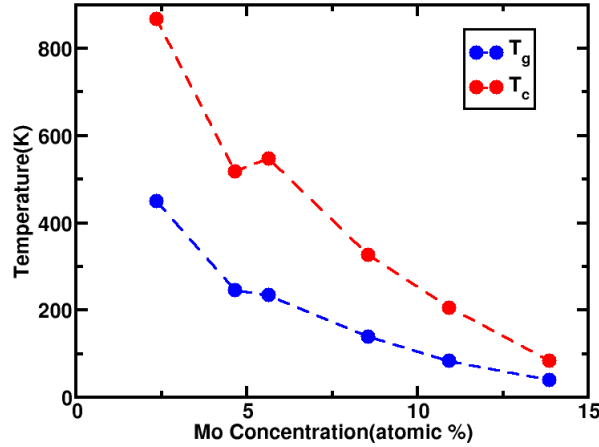


Figure 6.8: Mean-field phase diagram (top) for NiFeMo.

6.6 Magnetic relaxation : a theoretical analysis.

For our analysis we shall turn to the atomistic approach based on the quantum description of solids, as proposed by Skubic et.al.[Skubic and O.Eriksson, 2008] as detailed in §2.8.2. This is an approach which provides a study of magnetization relaxation from first-principles, appropriate for systems with complex chemical compositions. The approach is based on the density functional theory, which quite accurately reproduces both magnetic moments and EPIs. We shall follow Skubic et.al.[Skubic and O.Eriksson, 2008] and begin with the Landau-Lifshitz-Gilbert (LLG) equation and model finite temperatures by adding a stochastic field to the effective field. This leads to a stochastic differential equation :

$$\frac{\partial \vec{m}_R^Q}{\partial t} = -\gamma \vec{m}_R^Q \times \left\{ \vec{B}_R^Q + \vec{b}_R(t) \right\} - \frac{\gamma \alpha}{m} \left[\vec{m}_R^Q \times (\vec{m}_R^Q \times \left\{ \vec{B}_R^Q + \vec{b}_R(t) \right\}) \right] \quad (6.1)$$

where,

$$\vec{B}_R^Q = -\frac{\partial \mathcal{H}}{\partial \vec{m}_R^Q} \quad \mathcal{H} = -\frac{1}{2} \sum_{QQ'} \sum_{R \in Q} \sum_{R' \in Q'} J_{RR'}^{QQ'} \vec{m}_R^Q \cdot \vec{m}_{R'}^{Q'}$$

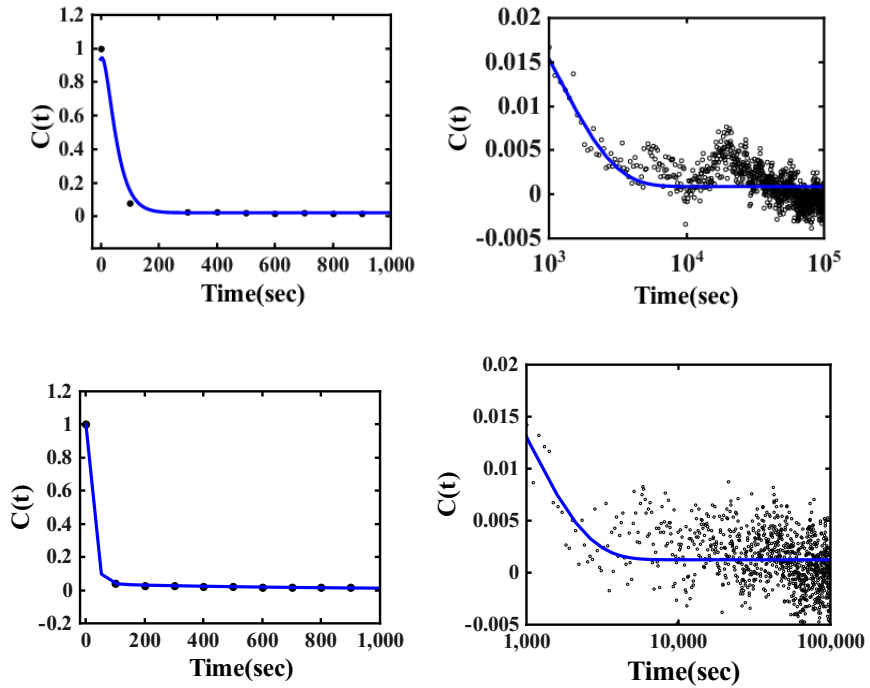


Figure 6.9: Relaxation of auto-correlation function at $T=5\text{K}$ for (Top) $\alpha = 0.1$ (bottom) $\alpha = 0.4$. The left panels show the fast initial decay while the right panels zooms onto the later slower decay.

$$\langle b_R^\mu(t) \rangle = 0 \quad \langle b_R^\mu(t) b_{R'}^\nu(t') \rangle = 2D \delta_{\mu\nu} \delta_{RR'} \delta(t - t').$$

Q, Q' refer to Fe, Ni and Mo components, γ is the electron gyromagnetic ratio. The stochastic field $\vec{b}_R(t)$ has a Gaussian distribution. The amplitude D of the stochastic field has been derived by Skubic [Skubic and O.Eriksson, 2008] and brings in the temperature

$$D = \frac{\alpha}{1 + \alpha^2} \frac{k_B T}{\gamma m}.$$

α is a phenomenological damping parameter, associated with D and the temperature as above and m is the magnitude of the magnetic moment.

For our numerical simulations we have found it convenient to work with the auto-correlation function defined as:

$$C(t) = \frac{1}{N} \sum_R \left\langle \left\{ \vec{m}_R^Q(0) \cdot \vec{m}_R^Q(t) \right\} \right\rangle_{\text{av}}. \quad (6.2)$$

The configuration average is taken over different configurations of the components Q .

The EPIs are calculated from our first-principles KKR-CPA method. Since the EPIs are very small energy differences (of the order of mRy) of large energies (of the order of 10^3 Ry), a separate calculation of each component energy will produce errors larger than the small differences themselves. Then the inter-atomic ‘pair-exchange’ parameters will be calculated following the theory of Lichtenstein *et al.* Figure 6.6 shows the dominant EPIs of the problem as functions of distance. At these compositions $J^{\text{NiNi}}(|R - R'|)$ is weak, consistent with Ni beginning to lose its intrinsic moments at these dilutions. $J^{\text{NiFe}}(|R - R'|)$ and $J^{\text{MoFe}}(|R - R'|)$ are reasonably strong, while $J^{\text{FeFe}}(|R - R'|)$ remains unchanged with composition. This is consistent with magnetism on Fe being robust and weakly dependent on its environment.

The relaxations were carried out on a cluster of size $32 \times 32 \times 32$ and at two different damping coefficients and at 5 K.

Figure 6.9 shows the relaxation of the auto-correlation function $C(t)$ for two different values of the damping parameter α . The left panels focus onto the fast initial relaxation, while the right panels zoom onto the later slower relaxation. Both the curves can be fitted to the double exponential form :

$$C(t) = C_{\text{eq}} + A \exp(-t/\tau_1) + B \exp(-t/\tau_2).$$

The dynamics of the relaxation process, as measured by the auto-correlation function with zero waiting times can be divided into two distinct regimes : an initial fast relaxation, followed by relaxation towards the global minimum. Let us first analyze the influence of

α	τ_1 (s)	τ_2 (s)
0.1	32.04 ± 4.8	1273.8 ± 87.8
0.4	28.48 ± 2.3	925.8 ± 66.3

Table 6.3: Fitted time parameters ($\tau_1 < \tau_2$) for the double exponential decay of magnetization at 5K for different damping parameters

damping on spin relaxation. The left panels in Figure 6.9 show the initial dynamics immediately after quench. Table 6.3 shows the relaxation times τ_1 and τ_2 of the double exponential fit. The short time behavior, characterized by τ_1 is weakly dependent on the damping α . In our case we have begun with a completely random spin distribution. The immediate relaxation of the auto-correlation function is dominated by strong precessional motion of the spins in the rapidly varying effective exchange fields. The system relaxes via a damping torque on each atomic spin. The subsequent relaxation is associated with equilibration of spins in their local fields. The relaxation rate τ_2 is now dependent on α . The larger the damping the smaller is τ_2 , that is, the relaxation is faster. This is clear from Table 6.3 that the variation of τ_2 with α is somewhat larger than the errors in its determination. From the right panels of Fig. 6.9 we see that after 1000 sec the autocorrelation decays to 0.015 from the initial value of 1 for $\alpha = 0.1$, while it decays to 0.0125 for $\alpha = 0.4$, in agreement with the above statements.

The behavior and arguments are similar to that given by Skubic et.al.[Skubic and O.Eriksson, 2008] for CuMn. Our analysis concludes that the relaxation may be fitted to a double exponential : an initial fast decay followed by a slower but still *exponential* relaxation. In the quasi-equilibrium state the magnetization and auto-correlation relaxations are similar. Our theoretical relaxation results agree qualitatively with experiment.

The main point to note that, both in experiment and theory, there does not seem to be any signature of an anomalously slow power-law, logarithmic or stretched exponential relaxation characteristic of the pure spin-glass phase. Given the experimental results on frequency dependent a.c. susceptibility peaks and bifurcation between FC and ZFC magnetization in low fields, absence of anomalously slow relaxation comes as a surprise.

6.7 Conclusions

In this paper we have reported results of experiments based on magnetization variation with temperatures at low magnetic fields and with magnetic field at 5K on NiFeMo ternary alloys at six different compositions. For five of the compositions there is a clear indication of transition from a paramagnetic to a random ferromagnetic phases. Fe boosts and Mo depletes

the fragile moment on Ni. The sixth sample with large Mo concentration showed the possibility of a glassy phase. First-principles density functional based theoretical analyses agreed well with the experimental data. A mean-field phase study also indicated paramagnetic-ferromagnetic transitions in a large part of the phase diagram. NiMo alloys threw up the possibility of Ni losing its fragile moment due to alloying with Mo just as the spin-glass phase becomes possible [P.Singh et al., 2011]. In NiFeMo, further alloying with Fe can bolster Ni moment and make the spin-glass phase stable.

Chapter 7

Magnetic properties of FeNiW alloy

This chapter is based on

Mitali Banerjee, Abhijit Mookerjee, A.K. Majumdar, **Rudra Banerjee**, Biplab Sanyal, and A.K. Nigam. Magnetism in FeNiW disordered alloys: Experiment and theory. *J. Magn. Magn. Mater.*, 322 (21):3558–3564, November 2010. ISSN 03048853.

7.1 Introduction

Magnetic cores require materials which have high permeability and low magnetostriction. Ni-Fe permalloys are one of the widely used materials in this area. High permeability is expected to result from domain rotation against weak crystalline anisotropy or from boundary displacements where the opposing force is small [Bozorth, 1953]. In last chapter (§6) we had substituted the $4d$ element Mo for Fe and studied its magnetic properties. In this work we shall substitute Fe with the $5d$ element W. Small amounts of added W, like Mo, enhances the permeability of the material and, simultaneously, it increases the electrical resistivity of permalloys reducing eddy current loss.

7.2 Samples

The sample chosen here is based on the experimental results that we have. The atomic percentage of samples used is shown in Table 7.1 The electronic configurations of Fe, Ni and

#	Ni	Fe	W
1	78.9	18.1	3.0
2	79.4	14.1	6.5
3	81.0	11.8	7.2
4	83.5	7.6	8.9
5	82.6	6.9	10.5
6	86.6	3.1	10.3

Table 7.1: Composition of the six samples in atomic %.

W are $[\text{Ar}] 3d^6 4s^2$, $[\text{Ar}] 3d^8 4s^2$ and $[\text{Xe}] 4f^{14}5d^46s^2$ respectively. It has a very high melting point of 3683 K.

7.3 Experimental Motivation ¹

In all the samples Ni concentration remains roughly around 79 - 86 at % while those of Fe decreases from 18 to 3 at % and those of W increases from 3 - 10 at % as we go from sample # 1 to # 6 in 7.1.

Figure 7.1 shows the magnetization variation with temperature for three different compositions. The left panel shows the magnetization variation for a sample with low Fe content of 3.1 at % (sample 6 of Table. 7.1.) measured at 20 Oe external field. The critical temperature T_c is obtained, as shown in the inset of left panel of Figure 7.1, by a sharp dip in dM/dt at the point of inflection in the M vs T curve. The right panel shows M vs T for two compositions with Fe content at 11.8 at.% and 14.1 at. % (# 3 and # 2 in 7.1), both

¹The experimental study discussed here is based on [Banerjee et al., 2010a] which is included in the thesis of Dr. Mitali Banerjee

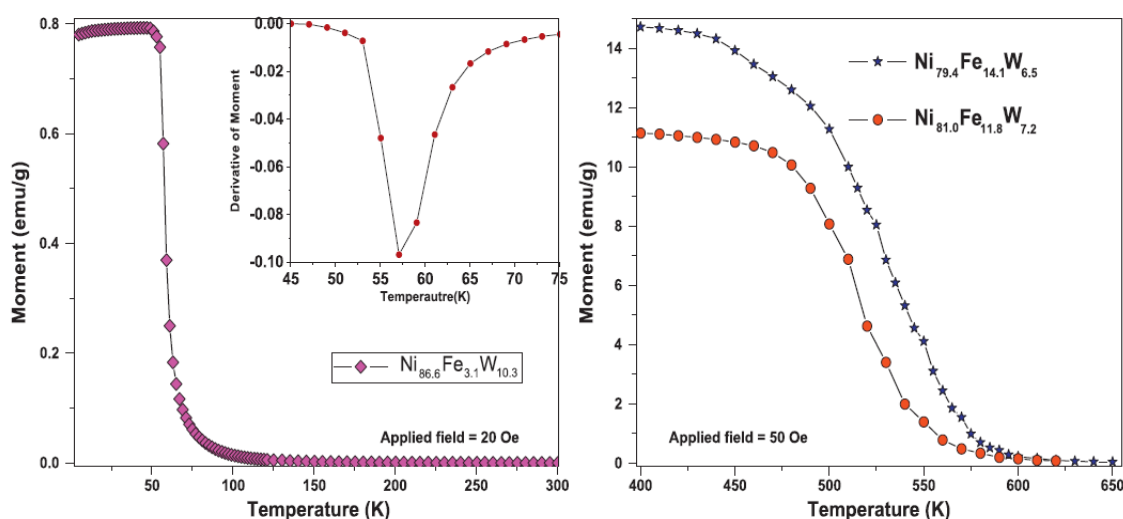


Figure 7.1: Magnetization vs Temperature for three compositions. (left) low Fe content of 3.1 at.% showing the behavior of dM/dT in the inset. (right) higher Fe content of 11.8 at.% and 14.1 at.%.

measured at an external field of 50 Oe. We note that T_c increases with Fe content for all the samples. Unlike the case of FeNiMo alloy (see §6), at no composition is there a sign of glassy behavior with different field-cooled and zero-field-cooled responses, at least not even at W concentration of 10.5 at.%.

Figure 7.2 shows the $M(H)$ vs H curves for the three samples 4,5 and 6 (Table 7.1). All experiments were carried out at 5 K. The saturation fields are very small, even smaller than those found in FeNiMo earlier. None of the samples show any reasonable hysteresis. Saturation magnetization increases with increasing Fe content. All samples studied are clean random ferromagnets. The hysteresis does not indicate any glassy behavior.

Table 7.2 summarizes the experimental data on the structure and magnetism of the six different samples described above.

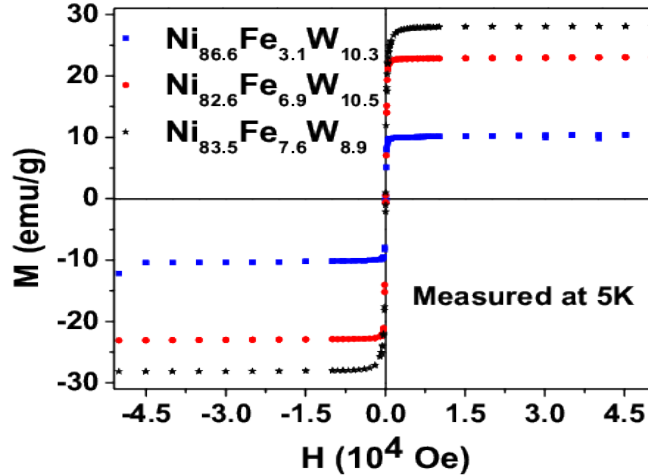


Figure 7.2: $M(H)$ vs H taken for samples 4,5 and 6 taken at 5 K.

7.4 Electronic Structure

Figure 7.3 shows the local magnetic moments on the Fe, Ni and W atoms in the alloy. The Ni concentrations increase from 78.9 at % to 86.6 at % across the six samples, while the Fe concentration goes down from 18.1 at % to 3.1 at %. The Fe moment hardly changes across the composition range. That for Ni increases almost linearly as Fe concentration increases and correspondingly W concentration decreases. The moment on W is small and opposite to that of Fe and Ni. Its behavior is a mirror image of that for Ni. We conclude that the moment on Ni is fragile. It is enhanced by Fe and diminished by W sitting in the neighborhood of Ni. The moment on W is induced by Fe and vanishes as Fe concentration decreases.

Figure 7.4 shows the experimental saturation magnetic moments at 5 K for the alloys at the six compositions described earlier. The comparison is with the theoretical magnetic moment estimates. Given the approximations involved in the theoretical estimates, the two agree reasonably well across the composition range. The magnetic moment is boosted when Fe concentration increases and increases almost linearly. This analysis complements our earlier conclusion that Fe boosts magnetism in Ni while W depletes it. In the ternary alloy,

Sample	a (Å)	M_s		T_c (K)
		(emu/gm)	μ_B	
1	3.560	80.4	0.85	775
2	3.562	54.2	0.57	530
3	3.567	50.0	0.53	515
4	3.573	28.6	0.30	300
5	3.576	23.0	0.24	191
6	3.586	10.4	0.11	55

Table 7.2: Summary of experimental results on the six samples.

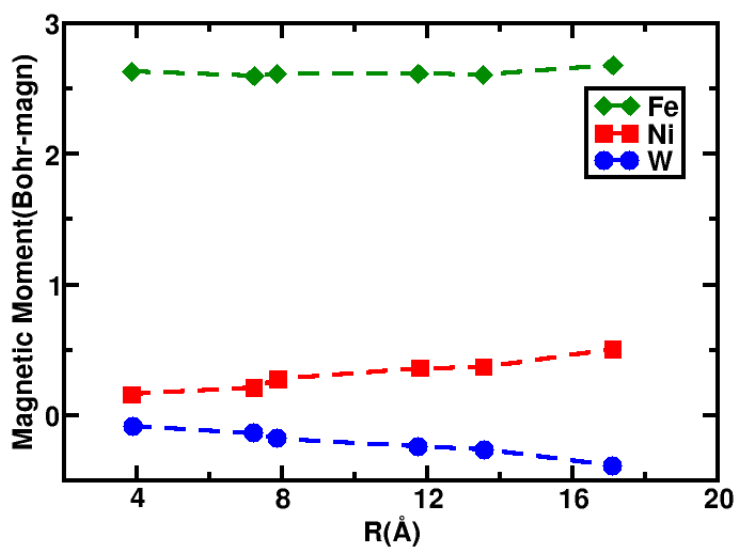


Figure 7.3: Local magnetic moments on Fe, Ni and W sites as a function of composition. The labels indicate the concentration of Ni which is kept around 80-83 at %.

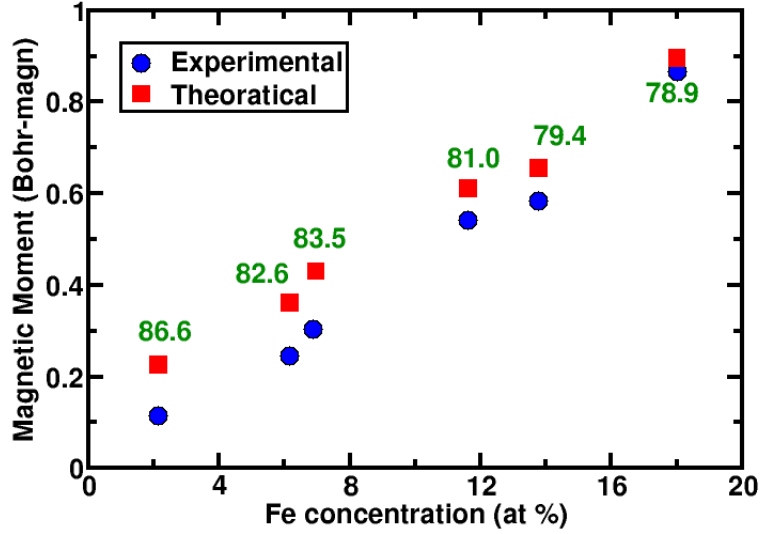


Figure 7.4: Total magnetic moments as a function of Fe concentration. The labels indicate the concentration of Ni in the sample.

there is a competition between these two. Because the alloys have mostly Ni, the behavior of the local moment on Ni mirrors that of the total moment.

7.5 Application to phase analysis of FeNiW ternary alloys

We shall continue our electronic structure analysis for FeNiW ternary alloys. The panels in Figure 7.5 show the pairing energies for the six distinct pairs from the three components Ni, W, and Fe. The Figure 7.6 illustrates the composition dependence of the pairing energies. The following comments may be made at this stage :

- (i) The strongest couplings are Fe-Fe, Ni-Fe and W-Fe, followed by Ni-Ni. The Ni-W coupling is relatively weak and W-W coupling is almost negligible.

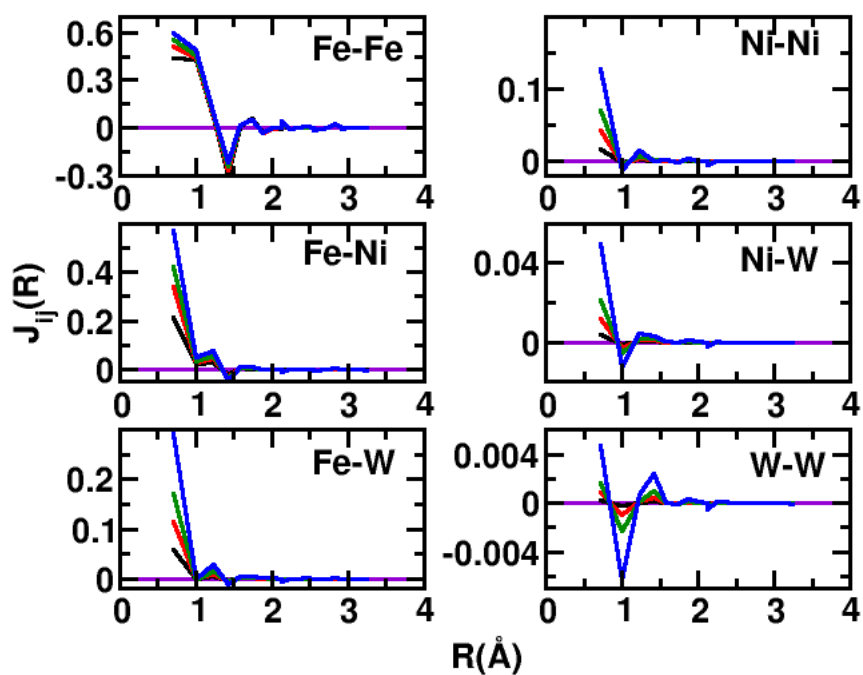


Figure 7.5: The pair interactions for different pairs of FeNiW alloy. Black for # 1; Red for # 2; Green for # 5; Blue for # 6 in alloy composition shown in Table 7.1.

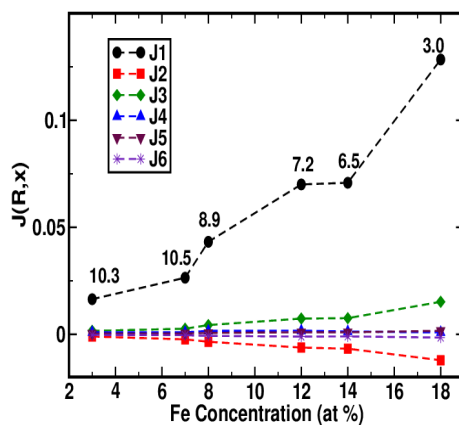


Figure 7.6: Behavior of the n -th nearest neighbor pair energies J_n as functions of composition. The W concentration is labeled on the graphs.

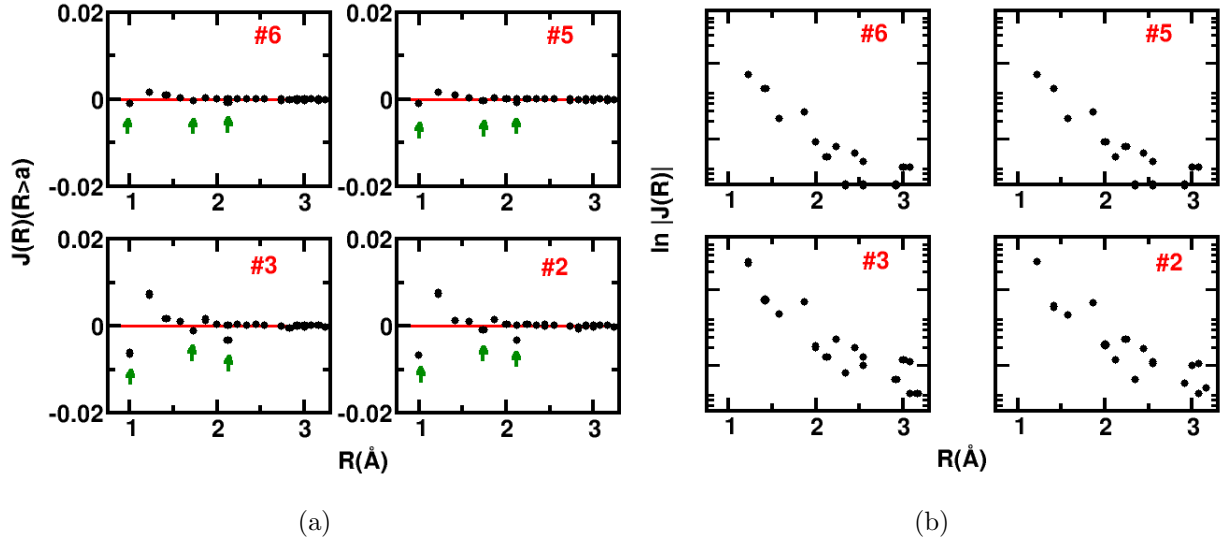


Figure 7.7: (a) Spread in $J^{NiNi}(R)$ as a function of R ($R > a$) (b) Behavior of $\log(|J^{NiNi}(R)|)$ vs R for the same compositions # 6, #5, #3, #2 as in Table 7.1.

- (ii) The Fe-Fe coupling is almost independent of composition. Fe compositions vary from 3 to 12 at %. All other couplings are strongly composition dependent. The Ni-Fe coupling is ferromagnetic up to the third nearest neighbors and increases with Fe concentration. It is known from earlier works on NiFe that Fe atoms in the neighborhood of Ni enhances its moment. This is a reflection of that. As for Ni-W, the coupling is induced by Fe and rapidly becomes negligible as the Fe concentration decreases and W increases. The Ni-Ni coupling shows both the effect of its enhancement by neighboring Fe as Fe concentration increases and its fragility when it becomes negligible as W concentration is increased. At higher Fe concentrations, the W-W attains a very small antiferromagnetic coupling. However, at lower Fe concentrations it is negligible. Similarly, higher Fe concentrations lead to a small W-Fe coupling which becomes negligible at lower Fe concentrations. The behavior of the pair couplings indicates : a strong magnetism in Fe which can induce magnetism in Ni and W; a weak, fragile magnetism in Ni and a very weak, induced magnetism in W.

- (iii) In Figure 7.7(a) we show the oscillatory behavior of $J^{NiNi}(R)$ vs R for $R > a$. For low concentrations of W the second, fifth and tenth neighbor $J(R)$ are antiferromagnetic (shown in red arrows). As the W concentration increases, these interactions become less negative and eventually ferromagnetic. As a consequence, frustration on triangular and quadrilateral plaquettes in a cubic unit cell of the face-centered cubic lattice drastically decreases. Frustration decreases exactly at those compositions where we expect a spin-glass phase. Therefore, like NiW in FeNiW too we should expect a spin-glass, if at all, in a very narrow range in the temperature-composition phase diagram.
- (iv) In Figure 7.7(b) we plot $\log(|J^{NiNi}(R)|)$ vs R . The behavior is a signature of an exponentially decaying oscillatory interaction. The exponential decay is due to disorder scattering which dampens the usual algebraically decaying oscillatory RKKY type interaction. As the W concentration increases, the range of interaction rapidly decreases, until for the composition 83.2:13.8:3 it is almost nearest neighbor as all other $J(R)$ for $R > a$ become negligibly small.

Figure 7.8 compares the experimental and mean-field estimates of the Curie temperatures for the six samples. The mean-field over-estimates T_c for all compositions. However, the qualitative trend of T_c elevation with increasing FE content and depression with increasing W content at a fixed Ni concentration, is reproduced by our mean-field prediction and confirmed by experiment.

Figure 7.9 shows the composition dependence of the critical temperatures T_c and T_g obtained from the mean field equations (9) and (10). For most of the composition range shown here, the T_g sits lower than T_c , therefore the transition is observed between the paramagnetic to the random ferro-magnetic phases. Only in the composition range at the lowest Fe concentration (3 at %) with the largest W concentration (10.3 at %) there is a possibility of T_g crossing over T_c and a transition to a spin-glass phase. Our extrapolation to W concentrations > 10.3 at.% indicates that a spin-glass phase may not exist in this alloy at all. Unlike FeNiMo, this seems to be the experimental evidence as well.

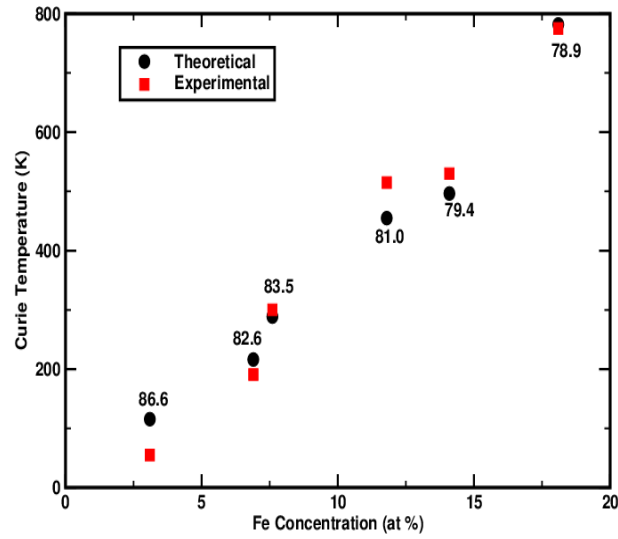


Figure 7.8: Experimental and theoretical estimates of the Curie temperature T_c for the six samples.

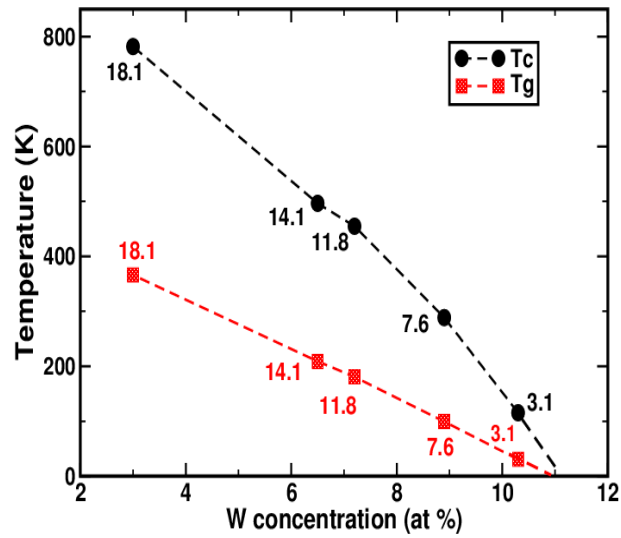


Figure 7.9: The mean-field phase diagram showing the critical temperatures T_c and T_g as a function of composition.

7.6 Conclusion

Using first-principles LSDA based TB-LMTO-ASR method we have obtained the magnetic moment across the composition range. Our values agree reasonably well both qualitatively and quantitatively with the experimental saturation magnetization as shown in [Banerjee et al., 2010a]. We have gone ahead and, based on the generalized perturbation expansion, mapped the energetics of the problem onto an equivalent random Ising model. The pair energies of the Ising model were derived from the TB-LMTO-ASR using Lichtenstein's formula. Our mean-field analysis of the model shows that at low Fe concentrations not only frustration decreases, but Ni also loses its moment. The resulting phase diagram confirms the possibility that spin-glass transition may not take place in this system even at low Fe concentrations, as found experimentally.

Chapter 8

Magnetic properties of AuCrFe alloy

This chapter is based on

Banerjee, Rudra, Abhijit Mookerjee, and Biplab Sanyal. Magnetic ordering in ternary AuFeCr alloys. *in manuscript*.

8.1 Introduction

In 3d transition metal doped noble metal binary alloys [Nakai et al., 1989], a spin glass phase is observed in low 3d-metal concentration. For a $A_{1-x}B_x$ where A is a Nobel metal and B is a transition metal, $5 < x < 10$ is generally the region where we expect a spin glass behavior due to the long ranged RKKY type interaction. In this paper we have shown that in ternary alloy, we can increase the percolation limit by doping two suitably chosen 3d metal (FM-AFM) to a noble metal matrix.

8.2 Low Au regime

We have chosen the concentration where Au concentration is very low and fixed Cr concentration to 20 atomic %. Figure 8.1 shows the magnetic EPE for the first few neighbors. The dominant magnetic interactions are Fe-Fe(FM), Fe-Cr and Cr-Cr (both AFM). It is noted

#	Au	Cr	Fe
1	10	20	70
2	20	20	60
3	25	20	55
4	30	20	50
5	35	20	45
6	40	20	40

Table 8.1: Samples in low-Au regime in atomic %

that dominant interactions, specially that for Fe-Fe and Fe-Cr vary very little with concentration if compared to weaker interactions involved with Au. Figure 8.2 shows spin-spin auto-correlations for those samples. It is seen that in this low-Au regime, magnetic ordering is unstable. It is seen that when $x_{Fe} \gg x_{Cr}$, the correlation tends to some stability in higher t_w (as in $x_{Au}=10,20$) but where $x_{Fe} \approx x_{Cr}$, due to FM-AFM strong interaction, it remains virulent (as in $x_{Au}=30,40$).

8.3 High Au Concentration: Around percolation limit

We have studied behavior of AuCrFe alloy with x_{Cr} is over [§8.3.1], just over [§8.3.2], equal [§8.3.3] and less [§8.3.4] than the percolation limit.

8.3.1 Cr above the percolation limit

We have fixed the Cr concentration at 25 atomic % and varied Au and Fe concentration as shown in Table 8.2. The basic features of J_{ij} , as in Figure 8.3 remains same in this regime as well with Fe-Cr and Fe-Fe remains almost same through concentration.

There are the following features in Figure 8.3:

- i. Fe-Fe interaction is the strongest followed by Cr-Cr and Fe-Cr; with Au-Au being the weakest.

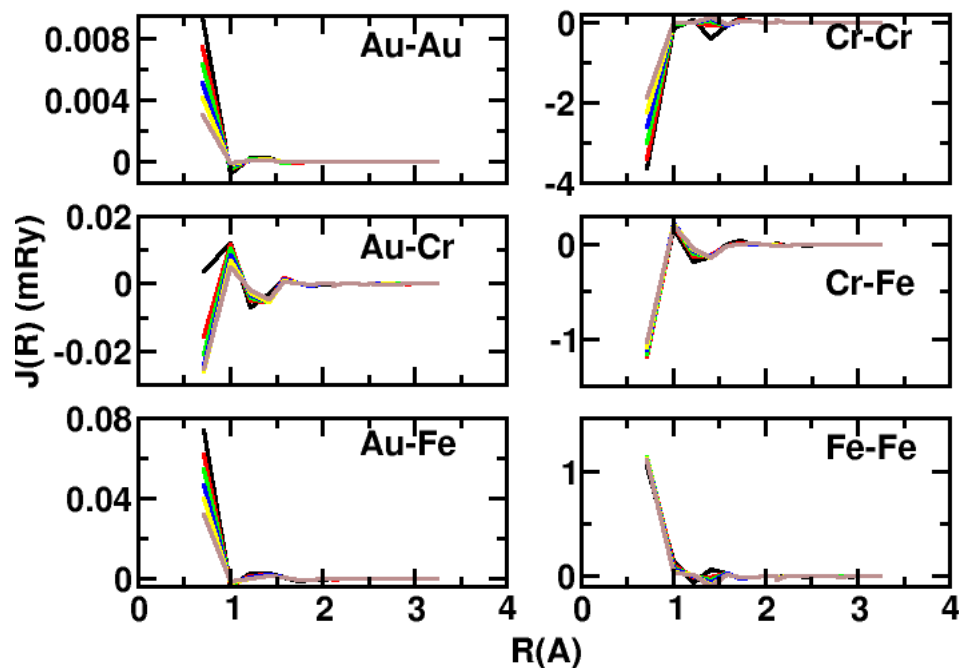


Figure 8.1: Magnetic pair interaction for $\text{Au}_x\text{Cr}_{20}\text{Fe}_{100-20-x}$ alloy with low Au concentration. (Black) $x=10$; (Red) $x=20$; (Green) $x=25$; (Blue) $x=30$; (Indigo) $x=35$; (Grey) $x=40$

- ii. The stronger the interaction, the least it depends on concentration. Fe-Fe interaction does not depend on composition at all in this range; while for Au-Au to Cr-Cr, it depends a lot on composition.

In this regime, as in Figure 8.4, there is a obvious and strong slowing down in spin dynamics as is evident from even lower waiting time.

If we look into it we can see the following features:

- i. For all the concentrations, there is a strong signal of frozen phase.
- ii. Composition $\# 2$ is absolutely frozen as the auto-correlation for higher waiting time is completely frozen. This is because of the fact that while Fe concentration is \cong to the percolation limit, along with frustration due to presence of Cr makes it frozen.

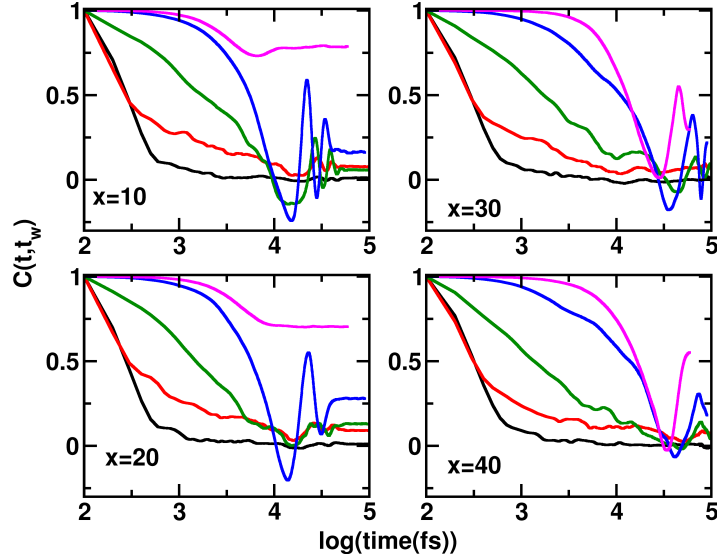


Figure 8.2: Spin relaxation of $\text{Au}_x\text{Cr}_{20}\text{Fe}_{100-20-x}$ alloy for different waiting time

#	Au	Cr	Fe
1	60	25	15
2	65	25	10
3	70	25	05

Table 8.2: Samples in $\text{Cr} > \text{percolation limit}$

8.3.2 Cr near the percolation limit

In this section we will discuss alloy composition with Cr concentration fixed at 18 atomic % which is slightly over the percolation range. The composition studied is shown in Table 8.3.

In brief, as shown in Figure 8.6, we can see a strong (but weaker than that in §8.3.2) aging in spin dynamics. There is a slowing down as normal in pure AuFe alloy. Aging is evident throughout the concentration range, but only in the highest waiting time.

The following features are evident from the Figure 8.5.

- i. The basic natures of magnetic interactions are same as in §8.3.1. The Fe-Fe is strongest

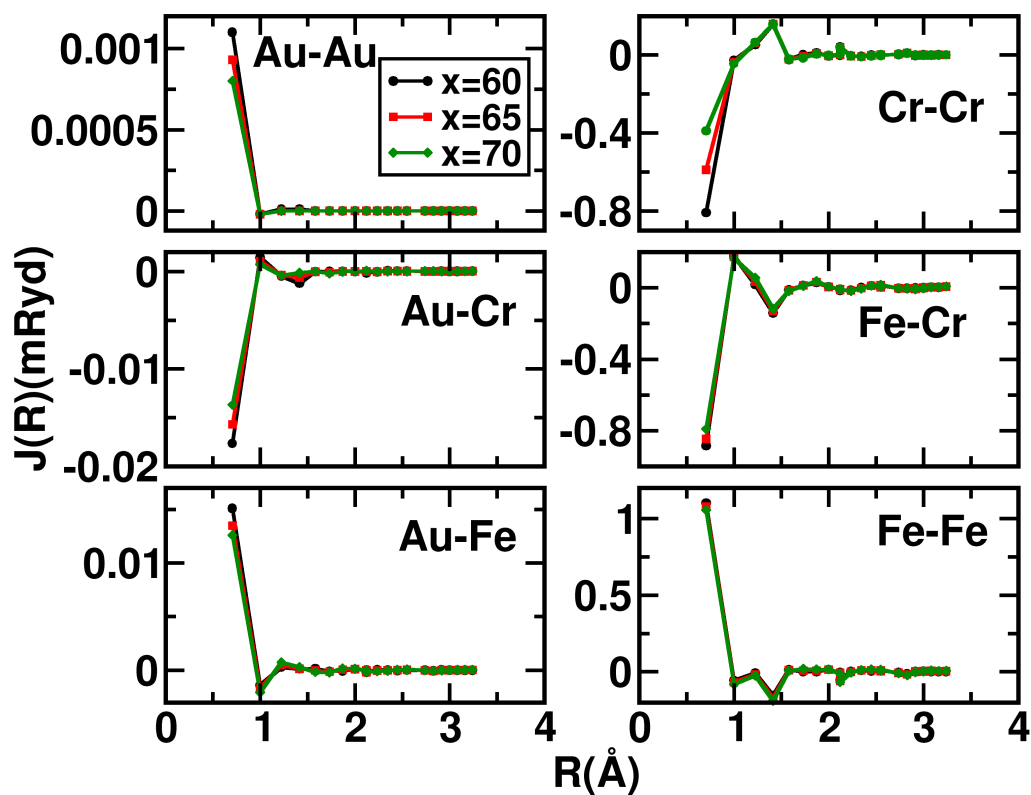


Figure 8.3: Magnetic pair interaction for $\text{Au}_x\text{Cr}_{25}\text{Fe}_{100-25-x}$ alloy with low Au concentration. (Black) $x=60$; (Red) $x=65$; (Green) $x=70$.

#	Au	Cr	Fe
1	60	18	22
2	65	18	17
3	70	18	12
4	80	18	02

Table 8.3: Samples in Cr \approx percolation limit

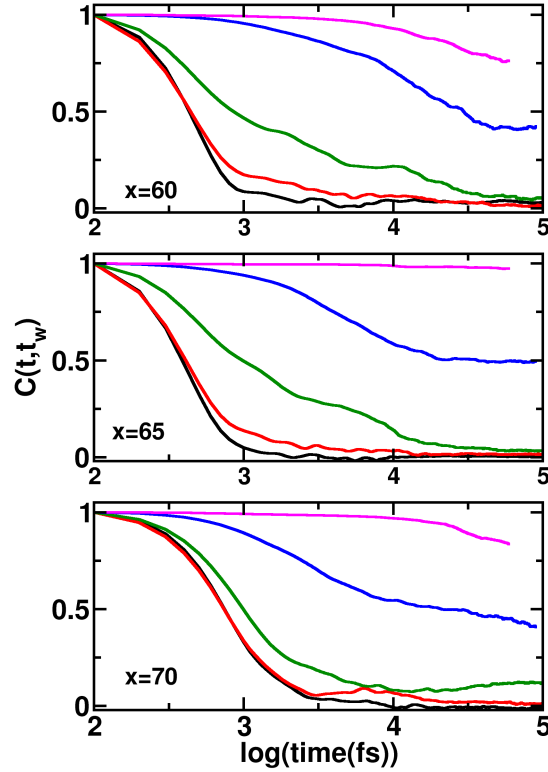


Figure 8.4: Autocorrelation function for $\text{Au}_x\text{Cr}_{25}\text{Fe}_{100-25-x}$ alloy for compositions # 1, # 2 and # 3 in Figure 8.2.

and almost independent of composition, where when the interaction is weak, it becomes more dependent on composition.

- ii. Unlike in §8.3.1, Cr-Fe interaction shows a hint of composition dependence. This tendency will grow larger as we can see in later sections.
- iii. It can also be seen from comparing Figure 8.5 and Figure 8.3 that the Fe-Fe interaction is also decreasing while others are remaining same. This point we will discuss later in §8.3.5

There is a magnetic slowing down that is evident from the Figure 8.6. We can see the

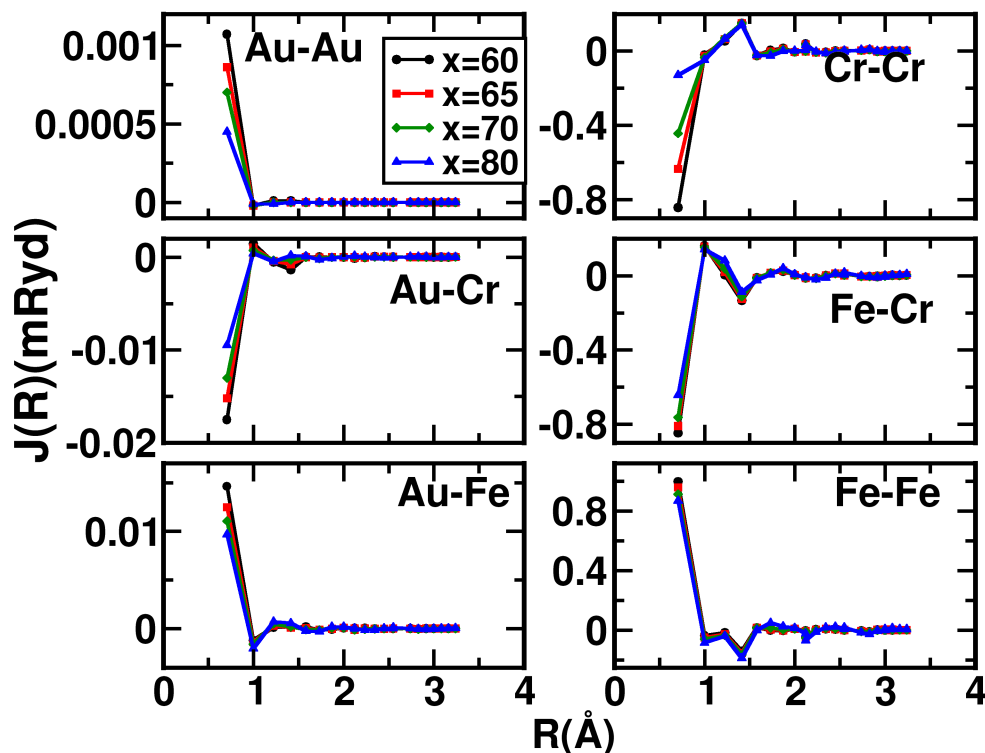


Figure 8.5: Magnetic pair interaction for $\text{Au}_x\text{Cr}_{18}\text{Fe}_{100-18-x}$ alloy with low Au concentration. (Black) $x=60$; (Red) $x=65$; (Green) $x=70$; (Blue) $x=80$.

following features of the spin dynamics from the figure:

- i. There is no evident frozen phase in this range.
- ii. But we cannot rule out all possibilities as there is a spin-frozen-phase like tail at the higher waiting time. But, notwithstanding the possibility, we can safely say there is very little possibility that spin glass phase will occur in this concentration range of Cr.

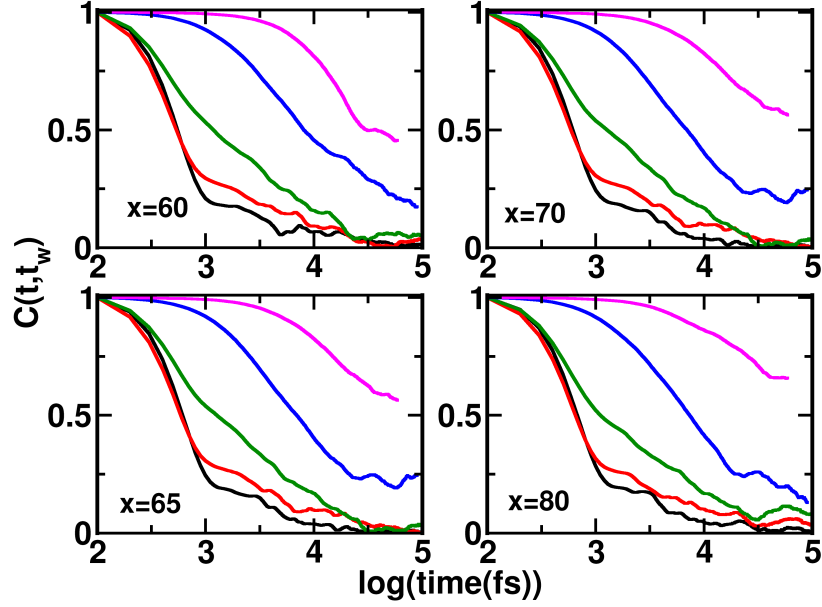


Figure 8.6: Autocorrelation function for $\text{Au}_x\text{Cr}_{18}\text{Fe}_{100-18-x}$

8.3.3 Cr inside percolation limit

In this section we have studied the AuCrFe alloy where the Cr concentration is fixed at 10 atomic % which is the percolation limit of AuCr binary alloy.

#	Au	Cr	Fe
1	60	10	30
2	70	10	20
3	80	10	10
4	85	10	05

Table 8.4: Samples in Cr inside percolation limit

Figure 8.7 shows the magnetic interaction between its components for different concentration shown in Table 8.4. Following features are evident from the J_{ij} plots Figure 8.7:

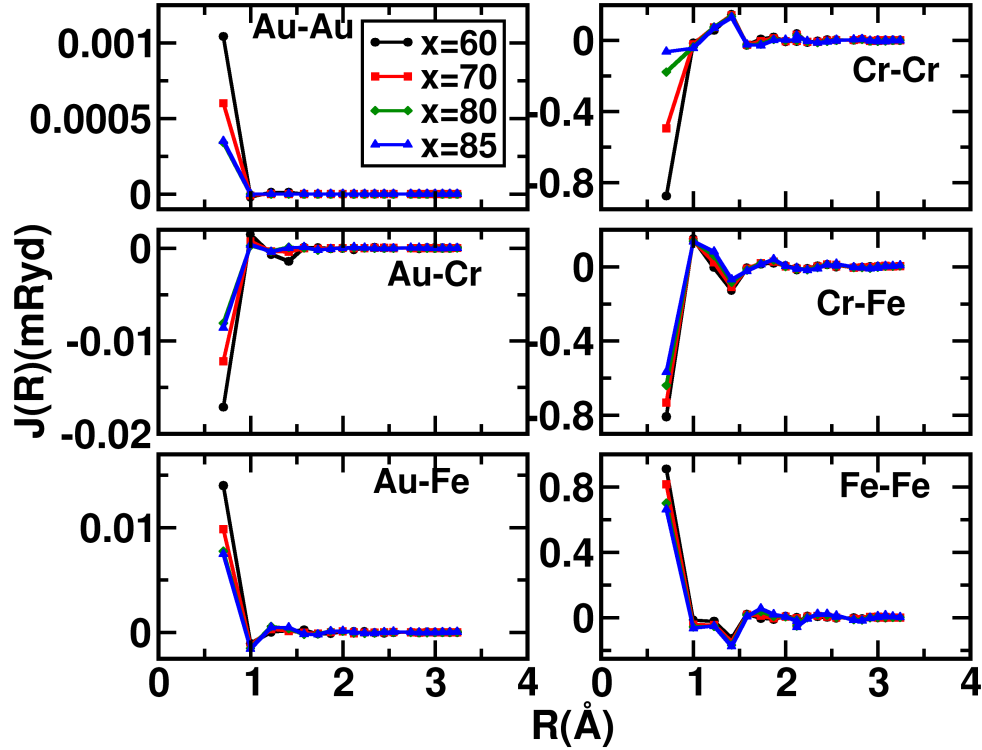


Figure 8.7: Magnetic pair interaction for $\text{Au}_x\text{Cr}_{10}\text{Fe}_{100-10-x}$ alloy with low Au concentration. (Black) $x=60$; (Red) $x=70$; (Green) $x=80$; (Blue) $x=85$.

- i. Basic qualitative nature remains same as in §8.3.1 and §8.3.2.
- ii. The absolute value of magnetic interaction is decreasing specially for first nearest neighbor interaction for Fe based interaction as Au-Fe, Fe-Cr and Fe-Fe.
- iii. As the absolute value of J_{ij} decreases, even the strongest Fe-Fe interaction becomes composition dependent; but we can also see this dependency decreases with higher concentration of Au. The variation of J_{ij} is very small for # 3rd and # 4th composition shown in Table 8.4.

Figure 8.8 shows the spin relaxation of this alloy for different waiting time. It is evident

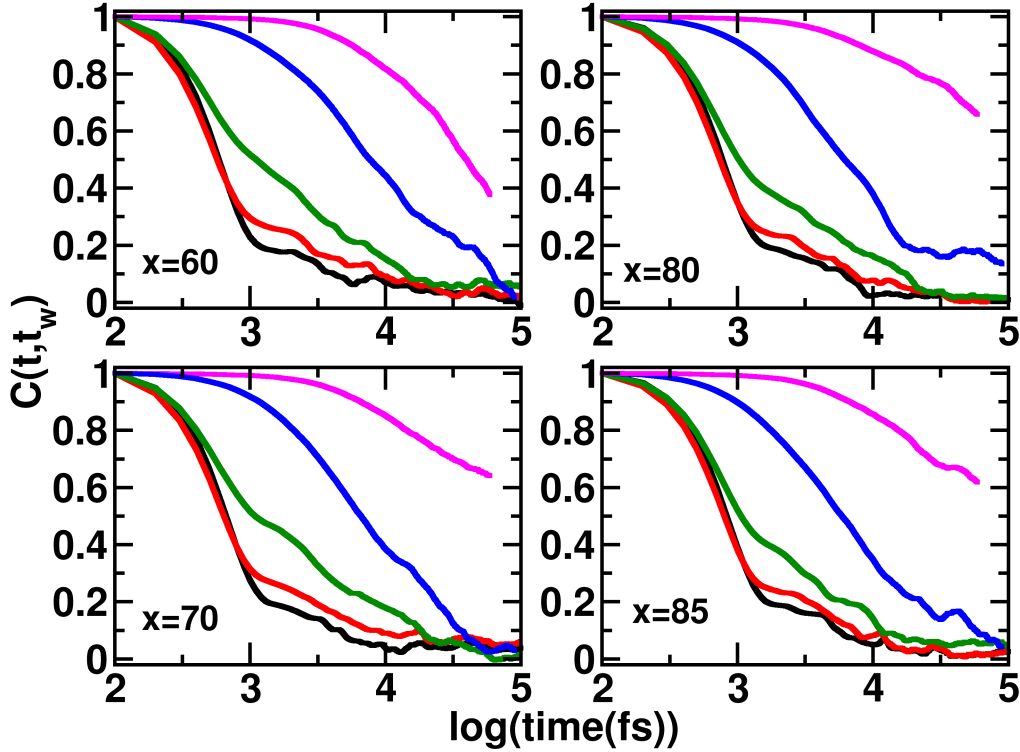


Figure 8.8: Autocorrelation function for $\text{Au}_x\text{Cr}_{10}\text{Fe}_{100-10-x}$

from the figure that the strong spin glass phase is broken and the tendency of relaxation indicates a paramagnetic ground state. The following features can also be seen in this figure:

- i. No spin glass phase is present in this composition range. The phase present in binary alloy is completely broken.
- ii. A signature of AuCr binary spin glass phase can be seen if we look at Figure 8.8 with higher Au concentration. Though no frozen phase exists, the tendency of slowing down is clear as we increase Au concentration, which means, decreasing the Fe concentration. For Au_{80} and Au_{85} , i.e. Fe is in impurity limit, tendency of slowing down for higher waiting time is clearly visible.

8.3.4 Cr lower than the percolation limit

In this last section, we will see the magnetic interaction and spin relaxation characteristics when Cr concentration is 06 atomic %, which is less than its binary percolation limit. The composition studied is given in Table 8.5. Figure 8.9 shows the magnetic interactions

#	Au	Cr	Fe
1	70	06	24
2	80	06	14
3	85	06	09
4	90	06	04

Table 8.5: Samples in Cr < percolation limit

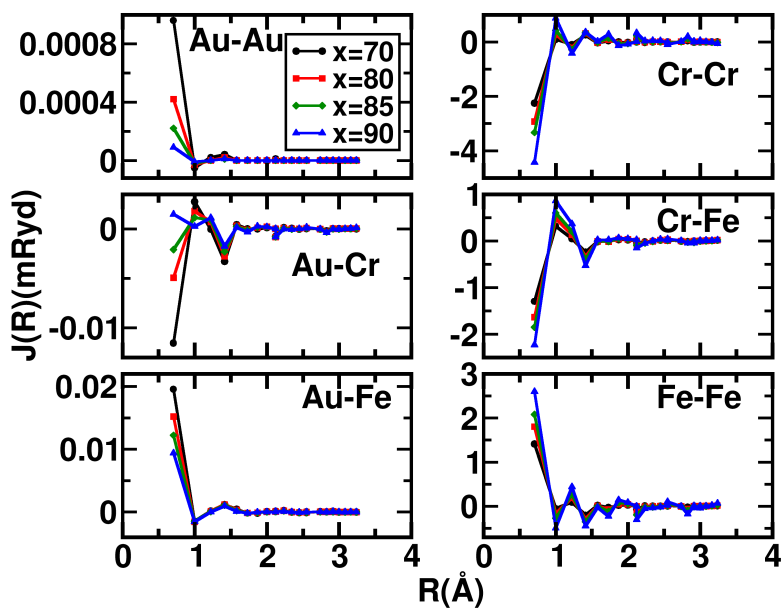


Figure 8.9: Magnetic pair interaction for $\text{Au}_x\text{Cr}_6\text{Fe}_{100-6-x}$ alloy with low Au concentration. (Black) $x=70$; (Red) $x=80$; (Green) $x=85$; (Blue) $x=90$.

between the different pairs of components. The following properties can be seen in it:

- i. The qualitative nature remains almost same. But we can see the Au-Cr interaction for Au_{90} for first nearest neighbor is *ferromagnetic* ; a different behavior from the other compositions we have studied.
- ii. First nearest neighbor interaction for all the interaction is very high.
- iii. The Au_{90} , i.e. # 4th composition of Table 8.5 shows a distinct oscillatory feature for Fe-Fe and Cr-Cr interaction. Though this oscillatory behavior is present in other composition also, they are not as distinct. This is a clear indication of existence of frustration. We will explore this more with spin relaxation seen in Figure 8.10.

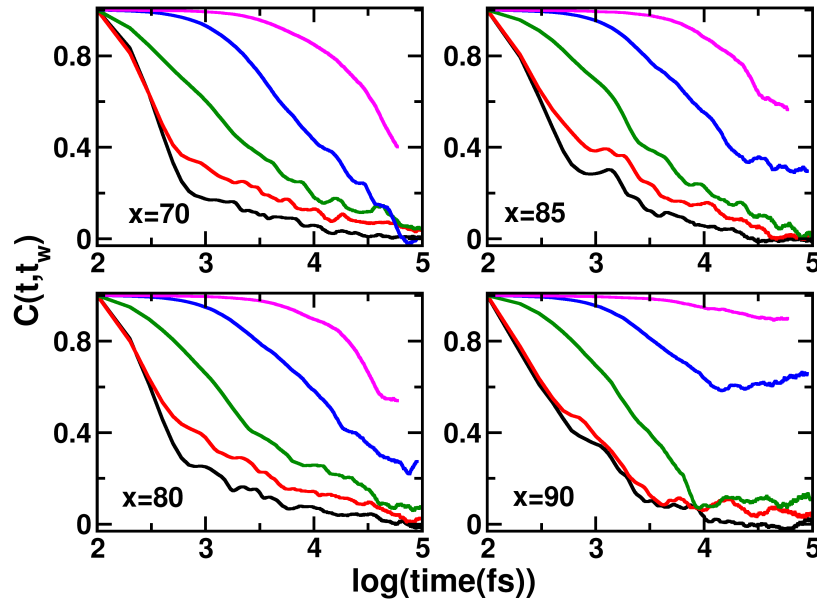


Figure 8.10: Autocorrelation function for $\text{Au}_x\text{Cr}_6\text{Fe}_{100-6-x}$

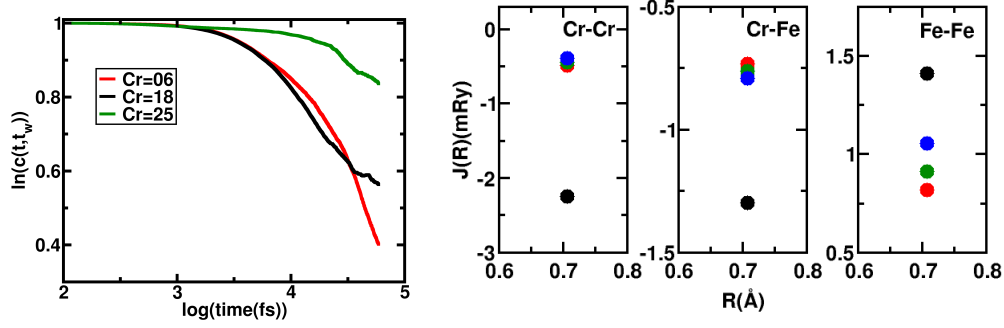
In Figure 8.10 we can see aging in spin dynamics but weaker than both in §8.3.1 and §8.3.2. There is a slowing down as normal in pure AuFe alloy. Aging is evident only for $x_{\text{Au}} = 80$ and in the highest waiting time. If we look into further details, we can see

-
- i. No evident frozen phase is seen except Au₉₀, i.e. # 4th composition of 8.5.
 - ii. The spin relaxation is slow, but except for Au₉₀, all tend towards a paramagnetic ground state.
 - iii. Au₉₀, i.e. # 4th composition of 8.5 shows a distinct spin frozen phase not only for very high waiting time but even before that. This is expected from the result of Figure 8.9, which shows very frustrated interaction for this composition.

8.3.5 Comparison

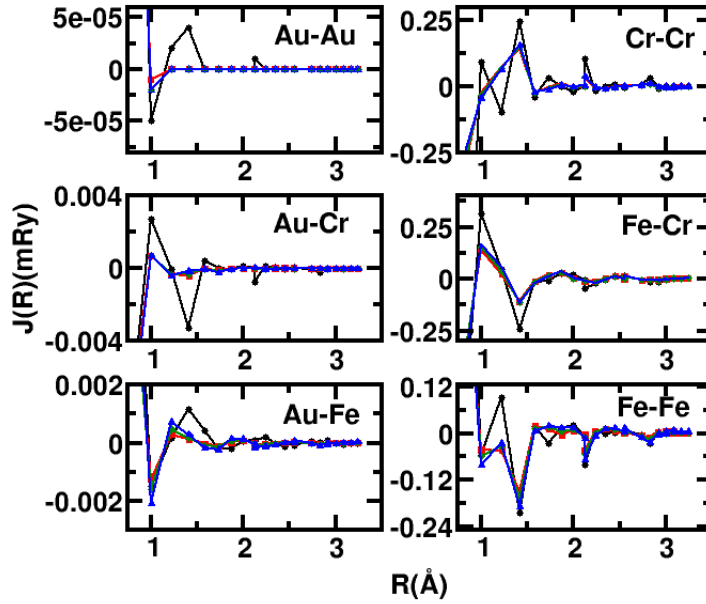
In the Figure 8.11, we have compared the magnetic EPE (J_{ij})'s for Au₇₀Cr_{*x*}Fe_{30-*x*}

In all the cases, we see the magnitude of interaction increases as the concentration of Cr decreases. This means the FM-AFM competition increases with the decrease of Cr concentration. As a result, as evident from Fig. 8.11(a), there is a strong spin glass phase in high Cr concentration. This is very reasonable as when x_{Cr} is in impurity range, it increases the mobility to spins and thus breaks the spin glass phase as opposite to in higher x_{Cr} where FM-AFM interaction becomes more evident and contributes to the spin-spin frustration.



(a)

(b)



(c)

Figure 8.11: (a) comparative plot with $\text{Au}_{70}\text{Cr}_x\text{Fe}_{30-x}$ for $t_w = 40960ps$. (b) and (c) Comparative plot effective interaction for dominating pair interactions: (b) for nearest neighbor and (c) for 2^{nd} nearest neighbor and beyond. (Black) Cr=06; (Red)Cr=10; (Green)Cr=18 and (Blue)Cr=25 for $\text{Au}_{70}\text{Cr}_x\text{Fe}_{30-x}$ alloy

Chapter 9

Conclusion

Art is never finished, only abandoned.

Leonardo da Vinci

In this thesis I have shown my work on development of configuration average based code ScASR and its application on binary and ternary disordered alloys. I have shown the methodology is at par and even for some specific cases, better than CPA, the most used methodology for studying disordered systems.

Taking specific cases like in FeNiMo, FeNiW and NiMn, I have shown our result matches well with experimental results; which is the best proof of usability of any numerical method.

If we look back to each chapter, the major achievements of the chapter is as follows:

In chapter 3 I have discussed the algorithm of my code and compared with other most prominent methodologies exist in this field.

In chapter 4 I have discussed several binary alloys to show the range of applications the code has.

In chapter 5 I have shown its application in NiMn alloy.

In chapter 6 and 7 I have discussed FeNi alloy doped with Mo and W respectively.

In this three chapter I have studied their electronic and magnetic structure and effective pair interactions and compared the results wit experimental findings.

In chapter 8 I have studied the magnetic properties and ageing of ternary AuCrFe alloy in the region around Cr concentration where spin glass phase exists in binary AuCr alloy. This helps us ti understand how exactly introduction of antiferromagnetic Cr affects the AuFe alloy.

But, as per the quotation from Leonardo da Vinci that starts this chapter, the work can not be considered finished or complete. There is a lot of scope for improvement in the code. I am planning to incorporate short-range ordering and non-collinear magnetism in ScASR. Incorporation of inhomogeneity and $\mathbf{L}-\mathbf{S}$ coupling in the code and applying the methodology to confined systems are the next thing I would like to work on.

References

- W. Abdul-Razzaq and JS Kouvel. Magnetic phase diagram of disordered Ni-Mn near the multicritical point. *Phys. Rev. B*, 35(4):1764, 1987.
- RG Aitken, TD Cheung, JS Kouvel, and H. Hurdequint. Transitions between spin-glass and ferromagnetic (or related) states in disordered Ni-Mn alloys. *J. Magn. Magn. Mater.*, 30(1):L1–L4, 1982.
- O. K. Andersen. Linear methods in band theory. *Phys. Rev. B*, 12:3060, 75.
- O. K. Andersen and O. Jepsen. Explicit, first-principles tight-binding theory. *Phys. Rev. Lett.*, 53(27):2571–2574, 1984.
- O. K. Andersen and R. V. Kasowski. Electronic states as linear combinations of muffin-tin orbitals. *Phys. Rev. B*, 4(4):1064, 1971.
- O. K. Andersen, O. Jepsen, and M. Snob. Linearized Band Structure Method. In M. Yussouff, editor, *Electronic Band Structure and its applications*. Springer, Berlin, 1987.
- V. Antropov. Time-dependent density-functional spin dynamics and its application for Fe and Ni. *J. Appl. Phys.*, 97:10A704, 2005.
- V. P. Antropov, M.I. Katsnelson, M.van Schilfgaadre, and B. N. Harmon. Ab initio spin dynamics in magnets. *Phys. Rev. Lett.*, 75:729, 1995.
- VP Antropov, MI Katsnelson, BN Harmon, M. Van Schilfgaarde, and D. Kusnezov. Spin dynamics in magnets: Equation of motion and finite temperature effects. *Phys. Rev. B*, 54(2):1019, 1996.

-
- Alden C. Armgnac. New Steel Alloy Is Rust Proof. *Popular Science*, page 31, December 1930.
- NW Ashcroft and ND Mermin. *Solid State Physics*. Brooks Cole, 1976.
- Mitali Banerjee, Abhijit Mookerjee, A.K. Majumdar, **Rudra Banerjee**, Biplab Sanyal, and A.K. Nigam. Magnetism in FeNiW disordered alloys: Experiment and theory. *J. Magn. Magn. Mater.*, 322(21):3558–3564, November 2010a. ISSN 03048853.
- Mitali Banerjee, **Rudra Banerjee**, A.K. Majumdar, Abhijit Mookerjee, Biplab Sanyal, and A.K. Nigam. Magnetism in NiFeMo disordered alloys: Experiment and theory. *Physica B: Condensed Matter*, 405(20):4287–4293, 2010b. ISSN 09214526.
- JL Beeby. Electronic structure of alloys. *Phys. Rev.*, 135(1A):A130, 1964a.
- J.L. Beeby. The electronic structure of disordered systems. *Proceedings of the Royal Society of London. Series A. Mathematical and Physical Sciences*, 279(1376):82, 1964b.
- A. Bergman, L. Nordström, O Eriksson, Klautau, and S Frota-Pessôa. private communication, 2008.
- K. Binder and A.P. Young. Spin glasses: Experimental facts, theoretical concepts, and open questions. *Rev. Mod. Phys.*, 58(4):801, 1986.
- M. Born and J. R. Oppenheimer. Zur Quententheorie der Molken. *Ann. Physik*, 84:457, 1927.
- A. Bovier and P. Picco, editors. *Mathematical aspectss of spin glasses and neuronal networks*, volume 41 of *Progress in Probability*, 1998. Birkhäuser Boston.
- RM Bozorth. The Permalloy Problem. *Rev. Mod. Phys.*, 25(1):42, 1953.
- W. F. Brown. Thermal fluctuations of a single-domain particle. *Phys. Rev.*, 130(5):1677, 1963.
- N. R. Burke. A tight-binding theory of the interactions between transition metal adatoms adsorbed on a transition metal substrate. *Surf. Sci.*, 58:349, 1976.

-
- WH Butler. Self-consistent cluster theory of disordered alloys. *Phys. Lett. A*, 39(3):203–204, 1972.
- W.H. Butler. Self-consistent cluster theory of disordered alloys. *Phys. Rev. B*, 8(10):4499, 1973.
- V. Cannella and JA Mydosh. Magnetic ordering in gold-iron alloys. *Phys. Rev. B*, 6(11):4220, 1972.
- R. Car and M. Parrinello. Unified Approach for Molecular Dynamics and Density-Functional Theory. *Phys. Rev. Lett.*, 55:2471–2474, Nov 1985.
- W. J. Carr. Intrinsic Magnetization in Alloys. *Phys. Rev.*, 85:590–594, 1952.
- D. M. Ceperley and B. J. Alder. Ground State of the Electron Gas by a Stochastic Method. *Phys. Rev. Lett.*, 45(7):566–569, 1980.
- A. Chakrabarti and A. Mookerjee. A self-consistent TB-LMTO-augmented space recursion method for disordered binary alloys. *The European Physical Journal B-Condensed Matter and Complex Systems*, 44(1):21–32, 2005.
- S. Chakraborty and A. K. Majumdar. Galvanomagnetic studies in γ -Ni_{100-x-y}Fe_xCr_y permalloys ($5 < x < 23$; $2 < y < 21$). *Phys. Rev. B*, 58:6434–6441, 1998a.
- S. Chakraborty and AK Majumdar. Electron transport studies in Ni-rich [gamma]-NiFeCr alloys. *J. Magn. Magn. Mater.*, 186(3):357–372, 1998b.
- RV Chepulskaa and VN Bugaev. Analytical methods for calculation of the short-range order in alloys: II. Numerical accuracy study. *J. Phys.: Condens. Matter*, 10:7327, 1998.
- D. Chowdhury. *The Spin Glass Transition*. PhD thesis, Department of Physics, IIT, Kanpur, 1983.
- D. Chowdhury and A. Mookerjee. Relation between Wohlfarth’s model and the percolation model of spin glasses. *J. Phys. F: Met. Phys*, 13:L19, 1983.

-
- P.C. Clapp and S.C. Moss. Correlation functions of disordered binary alloys. I. *Phys. Rev.*, 142(2):418, 1966.
- P.C. Clapp and S.C. Moss. Correlation functions of disordered binary alloys. II. *Phys. Rev.*, 171(3):754, 1968.
- E.U. Condon and G. Shortley. *The theory of atomic spectra*. Cambridge Univ Pr, 1935.
- A. R. Williams J. W. D. Connolly. Density-functional theory applied to phase transformations in transition-metal alloys . *Phys. Rev. B*, 27:5169, 1983.
- F. Cyrot-Lackmann. On the electronic structure of liquid transitional metals. *Advances in Physics*, 16(63):393–400, 1967.
- T. G. Dargam, R. B. Capaz, and Belita Koiller. Critical analysis of virtual crystal approximation. *Brazilian Journal of Physics*, 27/A(4):299, 1997.
- F. den Hollander and F. Toninelli. *Spin glasses: A mystery about to be solved*. EURANDOM, 2004.
- B. Derrida. A generalization of the random energy model which includes correlations between energies. *Journal de Physique Lettres*, 46(9):401–407, 1985.
- F. Gautier F. Ducastelle. Generalized perturbation theory in disordered transitional alloys: Applications to the calculation of ordering energies . *J. Phys. F: Met. Phys*, 6:2039, 1976.
- S.F. Edwards and P.W. Anderson. Theory of spin glasses. *J. Phys. F: Met. Phys*, 5:965, 1975.
- T. L. Einstein and J. R. Schrieffer. Indirect Interaction between Adatoms on a Tight-Binding Solid. *Phys. Rev. B*, 7:3629–3648, Apr 1973.
- Olle Ericksson. UppASD. <http://www.physics.uu.se/en/page/UppASD>, 2009.
- Jay Fenlason and Richard Stallman. The GNU Profiler . *GNU*, December 2011.

-
- E. Fermi. Un metodo statistico per la determinazione di alcune priorieta dell'atome. *Rend. Accad. Naz. Lincei*, 6:602, 1927.
- A. Finel and F. Ducastelle. Phase Transformations in Solids. In *Materials Research Society Symposia Proceedings*, volume 21, 1984.
- J. Friedel. Advances in Physics. *Phil. Mag. Suppl*, 3:446, 1954.
- Marc Gabay and Gérard Toulouse. Coexistence of Spin-Glass and Ferromagnetic Orderings. *Phys. Rev. Lett.*, 47:201–204, 1981.
- S. Ganguly, M. Costa, A.B. Klautau, A. Bergman, B. Sanyal, A. Mookerjee, and O. Eriksson. Augmented space recursion formulation of the study of disordered alloys with noncollinear magnetism and spin-orbit coupling: Application to MnPt and Mn₃Rh. *Phys. Rev. B*, 83(9):94407, 2011.
- Subhradip Ghosh, P. L. Leath, and Morrel H. Cohen. Phonons in random alloys: The itinerant coherent-potential approximation. *Phys. Rev. B*, 66:214206, Dec 2002.
- T. L. Gilbert. A phenomenological theory of damping in ferromagnetic materials. *Magnetics, IEEE transactions on*, 40(6):3443, 2004.
- TJ Godin and R. Haydock. New method for calculation of quantum-mechanical transmittance applied to disordered wires. *Phys. Rev. B*, 38(8):5237, 1988.
- TJ Godin and R. Haydock. The Block recursion library: accurate calculation of resolvent submatrices using the block recursion method. *Comput. Phys. Commun.*, 64(1):123–130, 1991.
- A. Gonis. *Green functions for ordered and disordered systems*. North-Holland Amsterdam, 1992.
- A. Gonis, X.G. Zhang, AJ Freeman, P. Turchi, GM Stocks, and DM Nicholson. Configurational energies and effective cluster interactions in substitutionally disordered binary alloys. *Phys. Rev. B*, 36(9):4630, 1987.

-
- Göran Grimvall. On rigid bands and mass enhancements in noble metal alloys. *Zeitschrift für Physik B Condensed Matter*, 14:101–104, 1972.
- F. Guerra. Broken replica symmetry bounds in the mean field spin glass model. *Communications in mathematical physics*, 233(1):1–12, 2003.
- F. Guerra and F. L. Toninelli. The Thermodynamic Limit in Mean Field Spin Glass Models. *Communications in Mathematical Physics*, 230:71–79, 2002.
- B. L. Gyorffy, A. J. Pindor, J. Staunton, G. M. Stocks, and H. Winter. A first-principles theory of ferromagnetic phase transitions in metals. *J. Phys F: Met. Phys*, 15(6):1337–1386, 1985.
- R. Hahn and E. Kneller. *Z. Metallk*, 49:426, 1958.
- J. J. Hauser and J. E. Bernardini. Structure-sensitive magnetic properties of Ni-Mn alloys. *Phys. Rev. B*, 30:3803–3807, Oct 1984.
- R. Haydock and MJ Kelly. Surface densities of states in the tight-binding approximation. *Surf. Sci.*, 38(1):139–148, 1973.
- R. Haydock and CMM Nex. Comparison of quadrature and termination for estimating the density of states within the recursion method. *Journal of Physics C: Solid State Physics*, 17:4783, 1984.
- R. Haydock, V. Heine, and MJ Kelly. Electronic structure based on the local atomic environment for tight-binding bands. *Journal of Physics C: Solid State Physics*, 5:2845, 1972.
- R. Haydock, V. Heine, and MJ Kelly. Electronic structure based on the local atomic environment for tight-binding bands. II. *Journal of Physics C: Solid State Physics*, 8:2591, 1975.
- J. Hellsvik. *Atomistic Spin Dynamics, Theory and Applications*. PhD thesis, Uppsala University, Materials Theory, 2010.

-
- J. Hellsvik, B. Skubic, L. Nordström, B. Sanyal, O. Eriksson, P. Nordblad, and P. Svedlindh. Dynamics of diluted magnetic semiconductors from atomistic spin-dynamics simulations: Mn-doped GaAs. *Phys. Rev. B*, 78(14):144419, 2008.
- B. Hillebrands and K. Ounadjela. *Spin dynamics in confined magnetic structures*, volume I, II, III. Springer Verlag, 2002, 2003, 2006.
- P. Hohenberg and W. Kohn. Inhomogeneous electron gas. *Phys. Rev.*, 136:B864, 1964.
- A. Huda, D. Paudyal, A. Mookerjee, and M. Ahmed. Spin-orbit coupling: a recursion method approach. *Physica B: Condensed Matter*, 351(1-2):63–70, 2004.
- M. Jarrell and H. R. Krishnamurthy. Systematic and causal corrections to the coherent potential approximation. *Phys. Rev. B*, 63:125102, Mar 2001.
- DD Johnson, DM Nicholson, FJ Pinski, BL Gyorffy, and GM Stocks. Density-functional theory for random alloys: Total energy within the coherent-potential approximation. *Phys. Rev. Lett.*, 56(19):2088–2091, 1986.
- T. Kaplan and LJ Gray. Off-diagonal disorder in random substitutional alloys. *Journal of Physics C: Solid State Physics*, 9:L303, 1976.
- Efthimios Kaxiras. *Atomic and Electronic Structure of Solids*. Cambridge University Press, 2003.
- S. Khmelevskiy, J. Kudrnovský, BL Gyorffy, P. Mohn, V. Drchal, and P. Weinberger. Frustration and long-range behavior of the exchange interactions in AuFe spin-glass alloys. *Phys. Rev. B*, 70(22):224432, 2004.
- Charles Kittel. *Introduction to Solid state physics*. John Wiley & Sons, 8th edition, 2005.
- M.W. Klein. Temperature-dependent internal field distribution and magnetic susceptibility of a dilute ising spin system. *Phys. Rev.*, 173(2):552, 1968.
- W. Kohn and N. Rostoker. Solution of the Schrödinger Equation in Periodic Lattices with an Application to Metallic Lithium. *Phys. Rev.*, 94:1111–1120, Jun 1954.

-
- W. Kohn and L. J. Sham. Self-consistent equations including exchange and correlation effects. *Phys. Rev.*, 140(4A):1133–1138, 1965.
- J. Koringa. On the calculation of the energy of a Bloch wave in a metal. *Physica*, 13(6-7):392–400, 1947.
- JS Kouvel and CD Graham Jr. Exchange anisotropy in disordered nickel-manganese alloys. *J. Phys. Chem. Solids*, 11(3-4):220–225, 1959.
- R. Kubo. The fluctuation-dissipation theorem and Brownian motion. In *Many-body theory*, volume 1, page 1, 1966.
- R. Kubo and N. Hashitsume. Brownian motion of spins. *Progress of Theoretical Physics Supplement*, 46:210–220, 1970.
- J. Kudrnovský and V. Drchal. Electronic structure of random alloys by the linear band-structure methods. *Phys. Rev. B*, 41(11):7515, 1990.
- J. Kudrnovský, V. Drchal, M. Sob, and O. Jepsen. First-principals calculations of electronic structure in random hep alloys: a Ru-Re example. *Phys. Rev. B*, 41(15):10459–10462, 1990.
- C. Lanczos. *An iteration method for the solution of the eigenvalue problem of linear differential and integral operators*. United States Governm. Pr. Office, 1950.
- L. Landau and E. Lifshitz. On the theory of the dispersion of magnetic permeability in ferromagnetic bodies. *Phys. Z. Sowjetunion*, 8(153):101–114, 1935.
- M. Lax. Multiple scattering of waves. *Rev. Mod. Phys.*, 23(4):287–310, 1951.
- M. Lax. Multiple scattering of waves. II. The effective field in dense systems. *Phys. Rev.*, 85(4):621, 1952.
- PL Leath. Equivalence of Expanding in Localized or Bloch States in Disordered Alloys. *Phys. Rev. B*, 2(8):3078, 1970.

-
- PL Leath. Pair Effects in Disordered Alloys. *Phys. Rev. B*, 5:1643–1646, 1972.
- M Levy. “Universal variational functionals of electron densities, first-order density matrices, and natural spin orbitals and solution of the v -representability problem. *Proc. Natl. Acad. Sci. USA*, 76:6062, 1979.
- E. H. Lieb. Density functionals for Coulomb systems. *Int. J. Quantum Chem*, 24:243, 1982.
- M. F. Ling, J. B. Staunton, D. D. Johnson, and F. J. Pinski. Origin of the $\langle 11/20 \rangle$ atomic short-range order in Au-rich Au-Fe alloys. *Phys. Rev. B*, 52:R3816–R3819, Aug 1995.
- Raquel Lizárraga, Sabina Ronneteg, Rolf Berger, Anders Bergman, Peter Mohn, Olle Eriksson, and Lars Nordström. Theoretical and experimental study of the magnetic structure of TiCo_2Se_2 . *Phys. Rev. B*, 70:024407, Jul 2004.
- MU Luchini and CMM Nex. A new procedure for appending terminators in the recursion method. *Journal of Physics C: Solid State Physics*, 20:3125, 1987.
- M. Mézard, G. Parisi, and M.A. Virasoro. Spin glass theory and beyond, volume 9 of World Scientific Lecture Notes in Physics. *World Scientific, Singapore*, 1987.
- P. Monod and Y. Berthier. Zero field electron spin resonance of Mn in the spin glass state. *J. Magn. Magn. Mater.*, 15:149–150, 1980.
- A. Mookerjee. Averaged density of states in disordered systems. *Journal of Physical Chemistry*, 6:1340, 1973.
- A. Mookerjee. A mean-field, effective medium theory of random magnetic alloys I: The random ising model. *Pramana*, 11(2):223–232, 1978.
- A. Mookerjee. Electronic structure of alloys, surfaces and clusters. In D. D. Sarma and A. Mookerjee, editors, *Electronic structure of alloys, surfaces and clusters*. Taylor-Francis, UK, 2003.
- A. Mookerjee and R. Prasad. Generalized augmented-space theorem for correlated disorder and the cluster-coherent-potential approximation. *Phys. Rev. B*, 48(24):17724, 1993.

-
- A. Mookerjee and S. B. Roy. A mean-field, effective medium theory of random magnetic alloys : II the random Heisenberg model . *Pramana*, 14:11, 1980.
- A. Mookerjee and S. B. Roy. A mean-field, effective medium theory of random binary alloys III. The ising model with competing interactions. *Pramana*, 21(3):171–182, 1983.
- Y. Nakai, M. Takagishi, and N. Kunitomi. Magnetic Phase Diagram of Ternary Alloy System, $\text{Au}^{i-} \text{Cr}^{\text{Fe}-j}$,). *J. Phys. Soc. Jpn.*, 58(1):291–294, 1989.
- L. Néel. Theory of magnetic viscosity of fine grained ferromagnetics with application to baked clays. *Ann. Geophys*, 5:99–136, 1949.
- C.M. Newman. *Topics in disordered systems*. Birkhäuser, 1997.
- CM Newman and DL Stein. Nonrealistic behavior of mean-field spin glasses. *Phys. Rev. Lett.*, 91(19):197205, 2003a.
- CM Newman and DL Stein. Ordering and broken symmetry in short-ranged spin glasses. *J. Phys.: Condens. Matter*, 15:R1319, 2003b.
- CMM Nex. Estimation of integrals with respect to a density of states. *Journal of Physics A: Mathematical and General*, 11:653, 1978.
- Pampa Pal, **Banerjee, Rudra**, Radheshyam Banerjee, Abhijit Mookerjee, Gopi Chandra Kaphle, Biplab Sanyal, Olle Eriksson, P. Mitra, A. K. Majumdar, and A. K. Nigam. Magnetic ordering in Ni-rich NiMn alloys around the multi-critical point : Experiment and Theory . *Phys. Rev. B (accepted)*, 2012.
- G. Parisi. The order parameter for spin glasses: A function on the interval 0-1. *Journal of Physics A: Mathematical and General*, 13:1101, 1980.
- R. E. Peierls. *The Quantum Theory of Solids*. Oxford University Press, 1955.
- J. Philhours and G.L. Hall. Ordering Conditions. I. For Alloys Represented by Generalized Ising Models. *Phys. Rev.*, 163(2):460, 1967.

-
- P.Singh, **R. Banerjee**, M. Rahaman, A.V. Ruban, B. Sanyal, and A. Mookerjee. Magnetic behaviour of AuFe and NiMo alloys. *Pramana*, 76:639, 2011.
- M. Rahaman and A. Mookerjee. Augmented-space cluster coherent potential approximation for binary random and short-range ordered alloys. *Phys. Rev. B*, 79(5):054201, 2009.
- M. Rahaman, S. Ganguly, P. Samal, T. Saha-Dasgupta, A. Mookerjee, and M.K. Harbola. A local-density approximation for the exchange energy functional for excited states: The band-gap problem . *Physica B: Condensed Matter*, 404:1137, 2009.
- Lord Rayleigh. *Phil. Mag. St*, 5(34):481, 1892.
- R. Banerjee**, M. Banerjee, AK Majumdar, A. Mookerjee, B. Sanyal, J. Hellsvik, O. Eriksson, and AK Nigam. $\text{Fe}_{3.3}\text{Ni}_{83.2}\text{Mo}_{13.5}$: a likely candidate to show spin-glass behaviour at low temperatures. *J. Phys.: Condens. Matter*, 23:106002, 2011.
- Derwyn A. Rowlands, Julie B. Staunton, Balazs L. Györffy, Ezio Bruno, and Beniamino Ginatempo. Effects of short-range order on the electronic structure of disordered metallic systems. *Phys. Rev. B*, 72:045101, Jul 2005.
- A. V. Ruban and H. L. Skriver. Screened Coulomb interactions in metallic alloys. I. Universal screening in the atomic-sphere approximation. *Phys. Rev. B*, 66:024201, Jun 2002.
- T. Saha and A. Mookerjee. The effects of local lattice distortion in non-isochoric alloys: CuPd and CuBe. *J. Phys.: Condens. Matter*, 8:2915, 1996.
- T. Saha, I. Dasgupta, and A. Mookerjee. Augmented-space recursive method for the study of short-ranged ordering effects in binary alloys. *Phys. Rev. B*, 50(18):13267, 1994.
- T. Saha, I. Dasgupta, and A. Mookerjee. Electronic structure of random binary alloys. *Journal of Physics: Condensed Matter*, 8:1979, 1996.
- B. Sanyal and A. Mookerjee. Magnetism and magnetic asphericity in NiFe alloys. *Phys. Lett. A*, 246(1-2):151–156, 1998.

-
- B. V. B. Sarkissian. The appearance of critical behaviour at the onset of ferromagnetism in AuFe alloys. *J. Phys. F: Met. Phys*, 11:2191, 1981.
- D. Sherrington and S. Kirkpatrick. Solvable model of a spin-glass. *Phys. Rev. Lett.*, 35(26):1792, 1975.
- H.L. Skriver. *The LMTO Method*. Springer Verlag, Berlin, 1984.
- B. Skubic, J. Hellsvik, L. Nordström, and O. Eriksson. A method for atomistic spin dynamics simulations: implementation and examples. *J. Phys.: Condens. Matter*, 20:315203, 2008.
- J. Hellsvik L. Nordström B. Skubic and O.Eriksson. A method for atomistic spin dynamics simulations: implementation and examples. *J. Phys.: Condens. Matter* , 20:315203, 2008.
- J. C. Slater. Wave Functions in a Periodic Potential. *Phys. Rev.*, 51:846–851, May 1937.
- P. Soven. Coherent-potential model of substitutional disordered alloys. *Phys. Rev.*, 156(3):809, 1967.
- D. Stein. Spin glasses: still complex after all these years? In *Decoherence and Entropy in Complex Systems*, pages 147–153. Springer, 2004.
- DL Stein and CM Newman. Spin Glasses: Old and New Complexity. In *American Institute of Physics Conference Series*, volume 1389, pages 965–968, 2011.
- Edward A. Stern. Rigid-Band Model of Alloys. *Phys. Rev.*, 157:544–551, 1967.
- GM Stocks and H. Winter. Self-consistent-field-Korringa-Kohn-Rostoker-coherent-potential approximation for random alloys. *Zeitschrift für Physik B Condensed Matter*, 46(2):95–98, 1982.
- GM Stocks, B. Ujfalussy, X. Wang, DMC Nicholson, WA Shelton, Y. Wang, A. Canning, and BL Györffy. Towards a constrained local moment model for first principles spin dynamics. *Philos. Mag. B*, 78(5-6):665–673, 1998.

-
- K. Tarafder, S. Ghosh, B. Sanyal, O. Eriksson, A. Mookerjee, and A. Chakrabarti. Electronic and magnetic properties of disordered Fe–Cr alloys using different electronic structure methods. *J. Phys.: Condens. Matter*, 20:445201, 2008a.
- K. Tarafder, M. Rahaman, D. Paudyal, B. Sanyal, O. Eriksson, and A. Mookerjee. Study of phase stability in a class of binary alloys using augmented space recursion based orbital peeling technique. *Physica B: Condensed Matter*, 403(21-22):4111–4119, 2008b.
- L. H. Thomas. The calculation of atomic field. *Proc. Cambridge Phil. Roy. Soc.*, 23:542, 1927.
- D. J. Thouless, P. W. Anderson, and R. G. Palmer. Solution of 'solvable model of a spin glass'. *Philos. Mag.*, 35(3):593–601, 1977.
- J Toulouse. *Commun. Phys*, 2:115, 1977.
- M. Tsukada. Contribution to the Many Site Theory of the Disordered System. *J. Phys. Soc. Jpn.*, 32(6):1475–1485, 1972.
- P. E. A. Turchi, L. Reinhard, and G. M. Stocks. First-principles study of stability and local order in bcc-based Fe-Cr and Fe-V alloys. *Phys. Rev. B*, 50:15542–15558, Dec 1994.
- B. Ujfalussy, B. Lazarovits, L. Szunyogh, GM Stocks, and P. Weinberger. Ab initio spin dynamics applied to nanoparticles: canted magnetism of a finite Co chain along a Pt (111) surface step edge. *Phys. Rev. B*, 70(10):100404, 2004.
- N. G. van Kampen. *Stochastic Processes in Physics and Chemistry*. North-Holland, 3 edition, 2007.
- M. Von Laue. The variability of ray beams. *Ann. Phys*, 44:1197, 1914.
- web of knowledge. <http://apps.webofknowledge.com>. Thomson Reuters, 2012.
- E. Wigner and F. Seitz. On the Constitution of Metallic Sodium. *Phys. Rev.*, 43:804–810, May 1933.

- E. Wigner and F. Seitz. On the Constitution of Metallic Sodium. II. *Phys. Rev.*, 46:509–524, Sep 1934.
- EP Wohlfarth. Spin glasses exhibit rock magnetism. *Physica B+C*, 86:852–853, 1977.
- F. Yonezawa and K. Morigaki. Coherent potential approximation. *T. Matsubara (Herausgeber): The Structure and Properties of Matter*, 28:383–432, 1973.
- Alex Zunger, S.-H. Wei, L. G. Ferreira, and James E. Bernard. Special quasirandom structures. *Phys. Rev. Lett.*, 65(3):353–356, 1990.